

AFRL-RW-EG-TR-2010-047

## Multifunctional Composite Structures

---

Ashok V. Kumar

University of Florida  
Office of Engineering Research  
339 Weil Hall  
Gainesville, FL 32611-0000



March 2010

FINAL REPORT FOR PERIOD MARCH 2006 – FEBRUARY 2010

DISTRIBUTION A: Approved for public release; distribution unlimited. 96<sup>th</sup> ABW/PA Approval and Clearance # 96ABW-2010-0304, dated 12 May 2010

**AIR FORCE RESEARCH LABORATORY, MUNITIONS DIRECTORATE**

■ Air Force Materiel Command    ■ United States Air Force    ■ Eglin Air Force Base

## NOTICE AND SIGNATURE PAGE

Using Government drawings, specifications, or other data included in this document for any purpose other than Government procurement does not in any way obligate the U.S. Government. The fact that the Government formulated or supplied the drawings, specifications, or other data does not license the holder or any other person or corporation; or convey any rights or permission to manufacture, use, or sell any patented invention that may relate to them.

This report was cleared for public release by the 96 Air Base Wing, Public Affairs Office, and is available to the general public, including foreign nationals. Copies may be obtained from the Defense Technical Information Center (DTIC) <<http://www.dtic.mil/dtic/index.html>>.

AFRL-RW-EG-TER-2010-047 HAS BEEN REVIEWED AND IS APPROVED FOR PUBLICATION IN ACCORDANCE WITH ASSIGNED DISTRIBUTION STATEMENT.

FOR THE DIRECTOR:

//SIGNED//

---

MIKEL M. MILLER, PhD, DR-IV  
Technical Director  
Advanced Guidance Division

//SIGNED//

---

GREGG L. ABATE, PhD, DR-III  
Chief, Airframe Dynamics & Robust Control Section  
Weapon Dynamics & Controls Sciences Branch

This report is published in the interest of scientific and technical information exchange, and its publication does not constitute the Government's approval or disapproval of its ideas or findings.

REPORT DOCUMENTATION PAGE				Form Approved OMB No. 0704-0188	
Public reporting burden for this collection of information is estimated to average 1 hour per response, including the time for reviewing instructions, searching existing data sources, gathering and maintaining the data needed, and completing and reviewing this collection of information. Send comments regarding this burden estimate or any other aspect of this collection of information, including suggestions for reducing this burden to Department of Defense, Washington Headquarters Services, Directorate for Information Operations and Reports (0704-0188), 1215 Jefferson Davis Highway, Suite 1204, Arlington, VA 22202-4302. Respondents should be aware that notwithstanding any other provision of law, no person shall be subject to any penalty for failing to comply with a collection of information if it does not display a currently valid OMB control number. <b>PLEASE DO NOT RETURN YOUR FORM TO THE ABOVE ADDRESS.</b>					
1. REPORT DATE (DD-MM-YYYY) 31-03-2010		2. REPORT TYPE FINAL		3. DATES COVERED (From - To) MAR 2006 - FEB 2010	
4. TITLE AND SUBTITLE Multifunctional Composite Structures				5a. CONTRACT NUMBER N/A	
				5b. GRANT NUMBER FA8651-06-1-0001	
				5c. PROGRAM ELEMENT NUMBER 62602F	
6. AUTHOR(S) Ashok V. Kumar				5d. PROJECT NUMBER 2502	
				5e. TASK NUMBER 99	
				5f. WORK UNIT NUMBER 21	
7. PERFORMING ORGANIZATION NAME(S) AND ADDRESS(ES)  University of Florida Department of Mechanical and Aerospace Engineering Gainesville, FL 32611				8. PERFORMING ORGANIZATION REPORT NUMBER	
9. SPONSORING / MONITORING AGENCY NAME(S) AND ADDRESS(ES) Air Force Research Laboratory Munitions Directorate 101 W Eglin Blvd Eglin AFB, FL 32542				10. SPONSOR/MONITOR'S ACRONYM(S) AFRL-RW-EG	
				11. SPONSOR/MONITOR'S REPORT NUMBER(S) AFRL-RW-EG-TR-2010-047	
12. DISTRIBUTION / AVAILABILITY STATEMENT DISTRIBUTION A: Approved for public release; distribution unlimited. 96 <sup>th</sup> ABW/PA Approval and Clearance # 96ABW-2010-0304, dated 12 May 2010					
13. SUPPLEMENTARY NOTES					
14. ABSTRACT  In this project, computational tools were developed that help in designing and analyzing multi-functional composite structures that have sensing and actuation capabilities. Magnetic actuation of composite structures using built-in or embedded electromagnetic devices was studied. The main application of interest is micro air vehicle wings that are designed to flap to generate thrust and lift. Computational tools were developed to design and analyze such structures actuated by magnetic forces. Coupled magnetostatic-elastostatic analysis capability was implemented into a pre-existing software (named IBFEM) developed at the University of Florida that can perform finite element analysis without the need for generating mesh. After a systematic comparison of several actuator designs, it was concluded that a coil actuator built into composite structures is an ideal means for actuation of composite structures. A conceptual design of a flapping wing vehicle was developed. A method for sensing load application and damage in composite structures by determining change in resistivity/conductivity was also studied. An algorithm for solving inverse problem to determine average resistivity values in composite structures was demonstrated.					
15. SUBJECT TERMS					
16. SECURITY CLASSIFICATION OF:			17. LIMITATION OF ABSTRACT  UL	18. NUMBER OF PAGES  125	19a. NAME OF RESPONSIBLE PERSON Gregg Abate
a. REPORT  UNCLASSIFIED	b. ABSTRACT  UNCLASSIFIED	c. THIS PAGE  UNCLASSIFIED			19b. TELEPHONE NUMBER (include area code) 850 883 2596

This page intentionally left blank

# TABLE OF CONTENTS

	<u>page</u>
LIST OF TABLES .....	v
LIST OF FIGURES .....	vii
Abstract .....	1
I. INTRODUCTION .....	3
1. Sensors .....	4
2. Actuators .....	4
3. Coupled Magneto-elastostatics using IBFEM .....	5
4. Analysis of shell-like structures using IBFEM .....	5
5. Design of structural actuators .....	5
II. COMPOSITE STRUCTURAL SENSORS .....	7
1. Overview .....	7
2. Sensing capabilities of carbon fiber composite structure .....	7
3. Experimental Procedures and Analysis .....	9
4. Inverse problem .....	11
5. Numerical validation .....	13
6. Experimental Results .....	15
Resistivity measurement for undamaged unidirectional composite specimen..	16
Woven composite specimen with and without damage .....	17
7. Discussion .....	18
III. COMPOSITE ACTUATING STRUCTURES .....	21
1. Overview .....	21
2. Motivation for structural actuators .....	22
3. Designing the shape and topology of structural actuator .....	24
4. Examples of Topology Design .....	29
Gripper Mechanism Design .....	29
Displacement Inverter Mechanism Design .....	32
Flapping Wing Mechanism .....	34
IV. MAGNETOSTATIC ANALYSIS USING Implicit boundary finite element method ...	37
1. Overview .....	37
2. Governing equation and Weak form for 2D Magnetostatics .....	38
3. Governing equation and Weak form for 3D magnetostatics .....	42
4. Solution structure for multi-material models .....	47

5. Magnetic force computation.....	48
6. Results and discussion .....	51
Coaxial cable.....	52
Switched Reluctance Motor.....	56
Iron block in a homogeneous magnetic field .....	57
Plunger solenoid actuator.....	61
7. Discussion .....	68
V. Modeling shells using IBFEM.....	69
1. Overview.....	69
2. Implicit Boundary Method .....	70
3. B-Spline approximations.....	73
4. Numerical Implementation .....	75
5. Results and Discussion .....	77
Centrally Loaded Square Clamped Plate in Bending .....	77
Micro Air Vehicle Wing design.....	78
Design of vibrating / oscillating wings for MAV .....	79
6. Discussion .....	81
VI. DESIGN of ACTUATORS FOR FLAPPING WING .....	83
1. Design criteria.....	83
2. Solenoid actuators with clapper armature.....	84
3. Solenoid actuators with plunger armature .....	88
4. Solenoid actuators with a combined plunger & clapper armature.....	91
5. Coil actuators.....	93
6. The best actuator among the designed actuators.....	94
7. Coupled magneto-elastostatic analysis of flapping wing actuation .....	97
VII. Conclusions and future ReSEARCH DIRECTION .....	103
1. Summary .....	103
Composite sensors:.....	103
Magnetically actuated composite structures.....	104
Computational tools for designing magnetically actuated structures .....	104
2. Future work.....	104
VIII. LIST OF REFERENCES.....	107

## LIST OF TABLES

<u>Table</u>	<u>page</u>
Table I: Measurement configurations .....	16
Table II: Computed values of resistivity .....	17
Table III: Resistivity values for woven fiber composite specimen .....	18
Table IV. Square plate: results for vertical displacement at the middle of the square plate, based on various meshes and element types.....	78
Table V. Comparison for three clapper solenoid actuators ( $N=30$ ).....	87
Table VI. Comparison for three plunger solenoid actuators ( $N=30$ ) .....	90
Table VII. Comparison for three combined plunger & clapper solenoid actuators ( $N=30$ ) .....	92
Table VIII. Comparison for coil actuators ( $N=30$ ) .....	94

This page intentionally left blank



# LIST OF FIGURES

<u>Figure</u>	<u>page</u>
Fig. 1 Two conventional methods to measure a resistivity: (a) Two-probe method (b) Four-probe method. ....	8
Fig. 2 A schematic diagram of the experimental setup.....	10
Fig. 3 FEA model of specimen with eight electrodes.....	10
Fig. 4 The voltage distribution as the solution of a forward problem.....	11
Fig. 5 Error in computed resistivity due to noise in voltage data.....	14
Fig. 6 Size and shape of the damaged region modeled in the forward problem.....	15
Fig. 7 Computed average conductivity versus damage size.....	15
Fig. 8 Woven fiber composite prepregs with embedded Teflon patches .....	17
Fig. 9 Flapping wing conceptual design.....	23
Fig. 10 Alternate design of actuator .....	23
Fig. 11 Deforming structural mechanism.....	24
Fig. 12 Shape representation using shape density function.....	25
Fig. 13 Feasible domain for gripper mechanism design with a 30 x 30 mesh .....	30
Fig. 14 Topology results for a mechanical gripper design with a 30 x 30 mesh using (a) Quad 4N elements (b) B-spline 9N elements (c) B-spline 16N elements.....	30
Fig. 15 Topology results for a mechanical gripper design with a 50 x 50 mesh using (a) Quad 4N elements (b) B-spline 9N elements (c) B-spline 16N elements.....	31
Fig. 16 Results from ABAQUS for the gripper mechanism (a) FE Model of the grripper mechanism with loads and boundary conditions (b) Deformed shape of the gripper mechanism .....	32
Fig. 17 Feasible domain for displacement inverter design with a 30 x 30 mesh .....	32

Fig. 18	Topology results for a displacement inverter design with a 30 x 30 mesh using (a) Quad 4N elements (b) B-spline 9N elements (c) B-spline 16N elements .....	33
Fig. 19	Topology results for a displacement inverter design with a 50 x 50 mesh using (a) Quad 4N elements (b) B-spline 9N elements (c) B-spline 16N elements .....	33
Fig. 20	Results from ABAQUS for the inverter mechanism (a) FE Model of the inverter mechanism with loads and boundary conditions (b) Deformed shape of the inverter mechanism .....	34
Fig. 21	Feasible domain for a flapping wing mechanism with 70 x 35 elements .....	35
Fig. 22	Topology results for the flapping mechanism for a 70 x 35 size mesh and a volume fraction of 0.5 (a) Quad 4N elements (b) B-spline 9N elements (c) B-spline 16 N elements .....	35
Fig. 23	Results from a finite element analysis on the optimum structure for the flapping mechanism.....	36
Fig. 24	2D FEM mesh .....	37
Fig. 25	Structure mesh for multi-material systems .....	38
Fig. 26	Analysis domain and boundaries .....	43
Fig. 27	Structured mesh.....	52
Fig. 28	Magnitude of the magnetic field .....	53
Fig. 29	3D coaxial cable model with the structured grid .....	53
Fig. 30	Current density in z-direction for 3D coaxial cable .....	54
Fig. 31	Magnetic field for 3D coaxial cable.....	54
Fig. 32	Magnetic field versus radius.....	55
Fig. 33	Convergence of H1 norm6.3. Plunger solenoid actuator.....	56
Fig. 34	Switched reluctance motor .....	56
Fig. 35	Field lines .....	57
Fig. 36	Iron cube in homogeneous magnetic field.....	58
Fig. 37	Iron objects with the same grid density .....	59

Fig. 38	Cross-sections with the line $y=z=10\text{mm}$ .....	59
Fig. 39	Components of B along the line $y=z=10\text{mm}$ . (a) $B_x$ (b) $B_y$ (c) $B_z$ .....	60
Fig. 40	Plunger solenoid actuator .....	61
Fig. 41	Top view of plunger actuators .....	62
Fig. 42	3D solid models of the solenoid actuators.....	62
Fig. 43	Magnitude of current density .....	63
Fig. 44	Magnetic flux density in y direction.....	63
Fig. 45	Magnetic field in y direction .....	64
Fig. 46	Magnetic force versus gap .....	64
Fig. 47	Planar clapper solenoid actuator with a cantilever beam. A) $d=10\text{mm}$ B) $d=20\text{mm}$ and C) $d=28\text{mm}$ .....	65
Fig. 48	Displacement on the tip versus. NI according to the location of the beam ....	66
Fig. 49	Top views of structures attached on the plunger armature. A) Solid plate, B) plate with one hole, and C) plate with two holes .....	66
Fig. 50	3D plunger solenoid actuators with attached structures. A) Solid plate, B) plate with one hole, and C) plate with two holes.....	67
Fig. 51	Deformed structures: A) Solid plate, B) plate with one hole, and C) plate with two holes .....	67
Fig. 52	Maximum displacement versus NI .....	68
Fig. 53	FEM mesh versus structured mesh for shells .....	70
Fig. 54	Shape function of one dimensional quadratic B-spline element .....	73
Fig. 55	Shape function of one dimensional cubic B-spline element .....	74
Fig. 56	Centrally loaded square plate.....	77
Fig. 57	IBFEM results (using cubic B-spline 64 node elements (5 x 5 Mesh) .....	77
Fig. 58	Abaqus result using S4R (10 x 10 Mesh).....	78
Fig. 59	Micro air vehicle wing.....	79
Fig. 60	Displacement plot (IBFEM 64N) for micro air vehicle wing (10 x 5 Mesh).....	79

Fig. 61	Displacement plot for micro air vehicle wing (ABAQUS S8R5, 542 elements).....	79
Fig. 62	Oscillating structural mechanism.....	80
Fig. 63	Mode shapes of vibration .....	81
Fig. 64	Solenoid actuator with clapper armature.....	84
Fig. 65	Computed results using IBFEM. A) Contour plot of magnetic vector potential, and B) Magnetic field density .....	85
Fig. 66	Clapper solenoid actuators. A) Design 1, B) Design 2, and C) Design 3 .....	86
Fig. 67	Contour plots of magnetic vector potential for clapper solenoid actuators. A) Design 1, B) Design 2, and C) Design 3 .....	87
Fig. 68	Solenoid actuator with plunger armature.....	88
Fig. 69	Computed results using IBFEM. A) Contour plot of magnetic vector potential, and B) Magnetic field in the y-direction .....	89
Fig. 70	Plunger solenoid actuators. A) Design 1, B) Design 2, and C) Design 3.....	89
Fig. 71	Contour plots of magnetic vector potential for plunger solenoid actuators. A) Design 1, B) Design 2, and C) Design 3. ....	90
Fig. 72	Three combined plunger & clapper solenoid actuators. A) Design 1, B) Design 2, and C) Design 3 .....	91
Fig. 73	Contour plots of magnetic vector potential for combined plunger & clapper solenoid actuators. A) Design 1, B) Design 2, and C) Design 3. ....	92
Fig. 74	Three coil actuators. A) Design 1, B) Design 2, and C) Design 3.....	93
Fig. 75	Magnitude of B fields for three coil actuators. A) Design 1, B) Design 2, and C) Design 3.....	94
Fig. 76	The best magnetic actuator among several designed actuators .....	95
Fig. 77	Solid model of the 3D coil actuator .....	95
Fig. 78	The top view of the 3D coil actuator .....	96
Fig. 79	The magnitude of the magnetic flux density of the coil actuator.....	96
Fig. 80	Lorentz force of the coil actuator versus NI .....	97
Fig. 81	The coil actuator with flapping wings.....	97

Fig. 82	Four structures with flapping wings. A) Design 1, B) Design 2, C) Design 3, and D) Design 4.....	98
Fig. 83	Four surface structures with flapping wings. A) Design 1, B) Design 2, C) Design 3, and D) Design 4. ....	99
Fig. 84	Structured mesh and boundary conditions of the first design.....	100
Fig. 85	Displacement in the z-direction during the wing stroke. A) Design 1, B) Design 2, C) Design 3, and D) Design 4.....	101
Fig. 86	Tip displacement versus NI for wing upstroke.....	102

This page intentionally left blank

## ABSTRACT

In this project, computational tools were developed that help in designing and analyzing multi-functional composite structures that have sensing and actuation capabilities. Magnetic actuation of composite structures using built-in or embedded electromagnetic devices was studied and a method for detecting load and damage in composite structures by determining change in resistivity/conductivity was studied. An algorithm for solving inverse problem to determine average resistivity values in composite structures was demonstrated. The method can use data from an arbitrarily large number of electrodes to compute average values of resistivity or conductivity for the structure. Finite element models for the structure are used to solve the forward problem, making this method very general and applicable to arbitrary shaped structures. Ideally, the electrodes should be embedded in the structures during the manufacturing process itself so that it can be used for quality control, detection of defects as well as subsequent health monitoring.

The idea of using magnetic forces to actuate structural mechanisms was studied. The main application of interest is micro air vehicle wings that are shell like structures. Topology optimization method was studied as a potential method for designing structures that have specified modes of deformation. The structure is then actuated using magnetic actuation means built into or around the structures. Several actuators were studied including solenoid actuators and coil actuators. After systematic comparison of several designs, it was concluded that a coil actuator built into composite structures is an ideal means for actuation of composite structures. A conceptual design of a flapping wing vehicle was developed that is designed to actuate by built in actuation capability of the body, wing and support structures. No external mechanisms, motors or linkages are needed.

Computational tools were developed to design and analyze structures actuated by magnetic forces. Magnetostatic analysis capability was implemented into a pre-existing software (named IBFEM) developed at the University of Florida that can perform finite element analysis without the need for generating mesh. Solid and surface geometry modeled on commercial CAD software can be imported into this software and analysis can be performed without approximating the geometry using a conforming mesh. The structured mesh approach has been demonstrated to work for magnetostatic analysis and validated using several examples with known solutions. The approach has been demonstrated for both 2D and 3D magnetostatic models. Structured mesh is easy to generate and the elements are regular and not distorted as in traditional finite element mesh. Magnetic forces were computed by integrating the magnetic force density. These

forces are then used in a subsequent structural analysis to determine the deflection of the structure. Shell elements based on uniform B-spline shape function were implemented into IBFEM. One of the key advantages of using these elements is that a structured mesh, which is easy generate automatically, can be used for the analysis. Both quadratic and cubic B-spline shape functions were tested and it was found that cubic elements provided very good results with fewer elements than quadratic elements. Computational cost is higher for these elements compared to traditional shell elements but often fewer elements are needed to get accurate results with cubic elements. The time taken to create the model is significantly lower because structured mesh generation is easily automated.



# I. INTRODUCTION

Composite materials have become the structural material of choice in many aerospace, automotive and other applications where low weight, high strength and rigidity are required. For applications such as in micro and unmanned air vehicles, in addition to the above requirement, it is necessary to pack more and more functionality into less and less space. This provides the motivation to make the structure of the air vehicles multifunctional, allowing it to perform important tasks including actuation, sensing, energy storage and energy harvesting in addition to providing structural support and rigidity.

Multifunctional composites can significantly increase the duration of flight and the payload of unmanned air vehicles (UAVs), especially micro-air vehicles (MAVs). Most of the research related to multifunctional materials, in the past, has been in the area of specialized materials such as piezoelectric and magnetostrictive materials that have been used to design and build both actuators and sensors. These specialized materials are typically not good structural materials and therefore are only used as attachments on a structure to achieve sensing capability or to induce/damp vibrations etc. Effect of large currents through metallic plates and shells have been studied in the past to explore potential applications such as providing better impact resistance to armor plates. Conductors carrying large currents through a magnetic field experience a damping force that could potentially provide improved impact resistance. However, metals lose strength at higher temperatures. Therefore the amount of current that can be applied is limited by Joule heating of the plates. For composite materials also heating is a problem that limits the current that it can carry so that electromagnetic damping may not provide significant impact resistance. However, heat generated by currents can be used beneficially to provide better curing of composites as well as for self healing after an impact especially for composites that have thermoplastic polymer matrix. Experimental evidence suggests that electric currents passing through composite structures improve their impact resistance [1-2].

In this project, methods for designing and fabricating multifunctional structures were studied. In particular, the focus was on designing sensors and actuators that can be of great value to applications such as micro air vehicles. Feasibility of sensing applied loads and damage on composites was studied. The idea of using embedded circuits and magnetic forces for actuation of structures was also studied. Analysis tools and design methods were developed for designing structural actuators that are structural mechanisms actuated using magnetic forces generated by embedded circuits and magnets. The main activities are summarized below.

## **1. Sensors**

The conductivity / resistivity of composite plates were studied with the goal of measuring changes in these properties as a means of detecting applied loads and for sensing damages within the structures. For composite plates and shells, the most common types of damage are due to delamination which occurs between layers and fiber breakages. Both these types of damage may not be visually detectable from external appearance. An inverse problem solving algorithm was developed for determining the overall resistivity of a composite structure using voltages measured at external electrodes. This provides a means of detecting damage by comparison with resistivity values of undamaged material. The measurement accuracy was sufficient to detect damage due to delamination and fiber breakage. Strains also cause small changes in resistivity. The inverse method was found to be not accurate enough to determine the magnitude or location of the applied load. The main problem is that the resistivity changes due to applied loads are very small and yet highly nonlinear and lacking repeatability.

## **2. Actuators**

Magnetic fields can be created by currents flowing through fiber networks or embedded conductors within composites. These magnetic fields can be used to actuate or deform the structure which in turn functions as a mechanism. This method can provide means to create very compact devices that have the capability to deform or serve as actuators. The potential applications include morphing (or shape change) of air vehicles and air vehicles that fly by flapping their wings. A key challenge in designing such structures is the lack of suitable design and analysis tools. Many commercial programs provide electrostatic, magnetostatic and electrodynamic analysis capability. However, the ability to perform coupled magneto-elastostatic analysis is needed for this application. Furthermore, the geometry of flapping wing type structures are complex requiring shell like analysis for the composite wings while using solid structures to model the magnetic actuators. Creating models for such systems is difficult in conventional finite element analysis software. A method that does not require conforming mesh was developed for coupled magneto-elastostatic analysis of multi-material systems by extending Implicit Boundary Finite Element Method (IBFEM). This method of analysis was developed at the University of Florida and has been used for linear elastic and heat transfer analysis in the past. The method was extended to enable magneto-elastostatic analysis as part of this research and applied to study several actuator designs for flapping wing design.

### **3. Coupled Magneto-elastostatics using IBFEM**

Implicit boundary finite element method (IBFEM) avoids the need for generating conforming mesh by using structured mesh for the analysis. A structured mesh (also referred to here as a grid) is a non-conforming mesh that is made up of regular shaped elements (rectangles for 2D or cuboids for 3D) and is easier to generate than traditional finite element mesh. The geometry of the analysis domain is represented using equations that are independent of the grid. Boundary conditions are applied using solution structures that are constructed using approximate step functions of the boundary such that these boundary conditions are guaranteed to be enforced. A variety of interpolation functions and approximations such as B-splines can be used with this approach. IBFEM was extended to perform magnetostatic analysis and to compute forces due to magnetic field. Using these forces in a subsequent elastostatic analysis, it is possible to simulate the deformation produced by the structure.

### **4. Analysis of shell-like structures using IBFEM**

Shell-like structures are modeled in traditional finite element method using shell elements. The geometry for such structures is modeled using surfaces that represent the mid-plane. In order to avoid mesh generation on a surface, the Implicit Boundary Finite Element Method (IBFEM) was extended for the analysis of shell-like structures. Three dimensional elements that use uniform B-spline approximation schemes are used to represent the displacement field. The surfaces representing the shell passes through these elements and the equations of these surfaces are used to represent the geometry exactly. B-spline approximations can provide higher order solutions that have tangent and curvature continuity. Numerical examples are presented to demonstrate the performance of shell elements using IBFEM and B-spline approximation. Models of flapping wings were created and analyzed to determine deflections due to magnetic forces produced by the actuators that were designed. Mode shapes of vibration or oscillation of several wings designs were also studied using this analysis tool.

### **5. Design of structural actuators**

Several magnetic actuator designs were studied as potential actuation mechanism within structural actuators. Three traditional designs were studied first: Solenoid actuator, clapper actuator and coil actuators. Potential for using these basic designs to actuate a flapping wing mechanism was studied. The coil actuator was found to be the most promising approach. Structural designs suitable for the flapping wing mechanism were explored. Topology optimization technique appears to be a promising tool to design such actuation mechanism. The basic methodology for 2D structural mechanism design using topology optimization using IBFEM was demonstrated. Further research is needed to extend these ideas to design shell-like composite structures.

This page intentionally left blank

## II. COMPOSITE STRUCTURAL SENSORS

### 1. Overview

A method to estimate the resistivity of composite structures using an inverse problem solving algorithm was developed that uses voltage distribution on the structure as data. Electrodes attached to the surface of the structure are used to obtain voltage data in response to current injection through a pair of these electrodes. The forward problem involves using the finite element method to predict the voltages at the electrodes using known values of resistivity. The inverse problem involves solving for the resistivity values using the experimentally measured voltage data. If the material does not have uniform properties, the computed resistivity values are average values. Damage or defect in a composite structure can significantly alter the average resistivity of the structure. To explore the possibility of using this approach to detect defects in manufacturing or damage due to loading, the effect of artificially induced damage/defect on the overall resistivity of the structure was studied.

### 2. Sensing capabilities of carbon fiber composite structure

Carbon fiber based composites are of interest in multifunctional and smart structure design because they are conductive and there is a correlation between changes in electrical properties and applied strains. The resistance changes under a variety of load types including tension/compression [3]-[8], bending [9], and impact [10]-[16] have been studied in the past. The motivation for these studies has been to explore the possibility of using carbon fiber composite as strain or stress sensor by measuring its change in resistance due to applied strain. The electrical properties are also affected by any damage such as delamination and cracks [18]-[27] that may occur in the structure. This provides a mechanism to sense damage by measuring the change in resistance and to identify delamination or crack or even to quantify the energy of the impact that caused the damage. Both AC and DC measurements have been used as means of non-destructive testing, damage detection and monitoring [18]-[19]. Due to its excellent mechanical properties, carbon fiber composites are widely used as a structural material. If they can also serve as a sensor that can detect applied loads or internal damage without the need for external sensors, then they can serve as a multifunctional or smart structural material.

The resistivity of carbon fiber composite material is orthotropic and therefore it is characterized by the three principal values. In order to measure the resistivity of carbon fiber composite, several specimen shapes and electrode placements schemes have been studied [3], [5], [17]. The simplest scheme would be to apply a uniform current density

on a composite specimen between electrodes on parallel faces and measure the voltage at these electrodes. This is the two-probe approach where, current injection and voltage measurements are made at the same pair of electrodes. Using resistance measured between two electrodes, the resistivity can be calculated when the specimen has simple geometry of known dimensions [17]-[21]. Fig. 1 illustrates both the two-probe method and the four-probe method. The two-probe method is highly sensitive to the contact resistance at the current injection electrodes because the measured voltage difference includes the voltage drop across the electrode and its interfaces. In the four-probe method, one pair of probes is used for the current injection at a pair of electrodes while the other pair is used for voltage measurement on a different set of electrodes. Again, the resistance is determined using Ohm's law and the resistivity can be calculated if the applied current is uniform and the specimen dimensions are known. The four-probe method provides results that are more reliable because it is not sensitive to contact resistance. These approaches for determining the resistivity are suited for simple block like specimen subjected to uniform current where the electrodes cover an entire side of the specimen. It is beneficial to be able to measure resistivity for arbitrary shaped structures that may be subjected to loads. Applied loads on the specimen can cause contact degradation between electrodes and the carbon fiber composite specimen [10]-[14]. It is preferred that the electrodes can be placed anywhere on the specimen so that they can be placed at locations least affected by the loads.

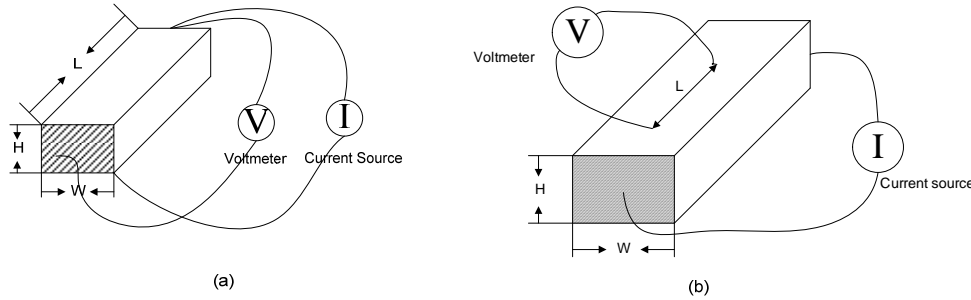


**Fig. 1 Two conventional methods to measure a resistivity: (a) Two-probe method (b) Four-probe method.**

An approach for estimating the average resistivity of arbitrarily shaped carbon fiber composite structures using inverse method was developed as part of this research. An inverse method involves computing the material properties, in this case resistivity, by searching for values of the properties such that a model using these values can correctly predict a set of experimentally measured responses. Inverse methods have been used in the past to detect damage in composites. Todoroki et al [20]-[23] used an array of electrodes placed along the top surface of a plate-like specimen to detect damaged areas using inverse method and response surface models. The electric potential computed tomography (CT) approach [24]-[27] also uses inverse method for

defect identification (delamination or surface crack) using passively observed electric potential values on a thin piezoelectric film attached on the surface of the structure.

In this project, an inverse problem solving method was used to compute the overall or average resistivity values of arbitrarily shaped composite structures using voltages measured on surface electrodes as data. If the resistivity of the undamaged and defect free material is known then the average resistivity computed using this method for a given structure can be compared with the known values to determine if the structure is free of defects or damages. The forward problem is the finite element model of the composite structure that can predict voltages on the set of electrodes distributed over the specimen if the resistivity is known. The inverse problem involves solving for the resistivity values using experimentally measured voltages at the electrode. The primary advantage of using a finite element model, as opposed to an analytical model, in the forward problem is that the specimen can then be of arbitrary shape giving us the flexibility to determine average material properties of real structural components that are in use in automotive or aerospace structures.

### **3. Experimental Procedures and Analysis**

In this study, both unidirectional carbon fiber composite plates and woven fiber composites were used with electrodes attached on the top and bottom surfaces. Voltage differences between pairs of electrodes were measured using one set of probes while current was injected at a different pair of electrodes using a different set of probes. Fig. 2 shows the schematic diagram of the experimental setup with a specimen that has eight electrodes, with four electrodes on the top, and the other four electrodes at the bottom. As shown in the figure, a current source and voltmeter are attached to a multiplexer that can be used to measure the voltage between any two pair of electrodes while current is injected between any other pair of electrodes. Therefore, for any pair of electrodes between which current is applied we can measure voltage difference between all the other combinations of electrodes available. Then by changing the current injection electrode pair, even more data can be obtained that can be used in the inverse method to obtain an average value of resistivity in the three principal directions. This method will be robust even when the structure is under any loading because it is not necessary to generate uniform current distribution between any electrode pairs and electrodes could be located where it is relatively safe from damage due to any external load.

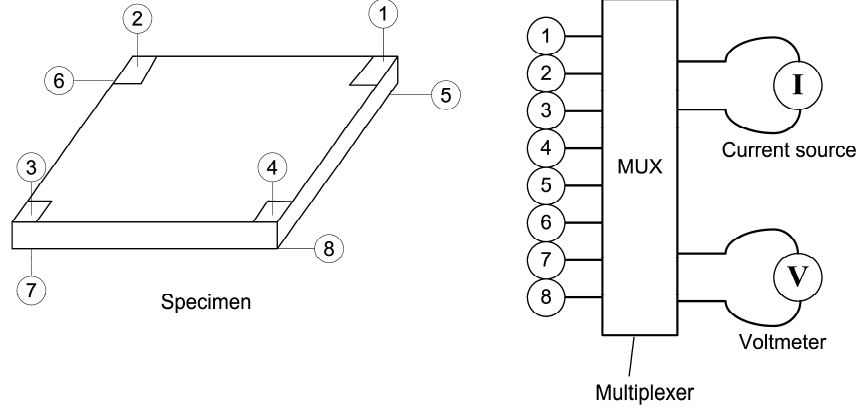


**Fig. 2 A schematic diagram of the experimental setup**

As mentioned earlier, the model used for the inverse problem is a finite element model. A finite element mesh that represents the geometry of the specimen with reasonable accuracy is needed. Using this FEA model, we solve the forward problem, which involves finding the voltage distribution using the known value of applied current and an estimate (or guess) of the resistivity values in the three principal directions. Accurate values of the resistivity are then calculated by minimizing the error between the computed voltages at the electrodes and the measured voltages by varying the resistivity values iteratively. The optimization process involves solving the forward problem repeatedly until good estimates of the resistivity values are obtained. Gauss-Newton algorithm was used for minimizing the least square error [28].

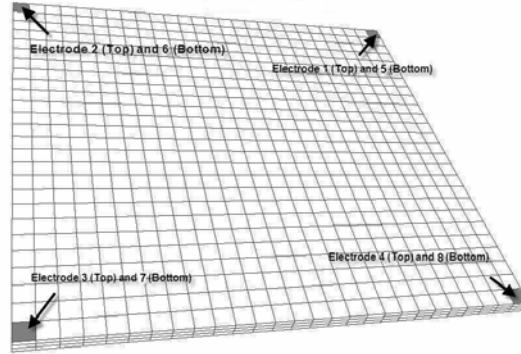


**Fig. 3 FEA model of specimen with eight electrodes**

Fig. 3 shows the FEA model used for the eight electrodes specimen. The size of specimen modeled here is  $54 \times 52 \times 1.5 \text{ mm}^3$ . The model has 3024 hexahedral elements so that the average element size is  $2 \times 2 \times 1.5 \text{ mm}^3$ . Electrodes 1 and 7 were used as the current injection electrode pair, with electrode 7 as source and electrode 1 as drain or reference point. The current injection electrodes were modeled as surfaces (or faces of elements) that have a specified normal component of current density. The voltage at the reference electrode (or associated nodes) was set to zero. For this analysis, the



amplitude of injected current applied was 28.9mA and the resistivity was  $0.01\text{ m}\Omega\text{m}$  in all the three principle directions. Fig. 4 shows the voltages computed by solving the forward problem using FEA.

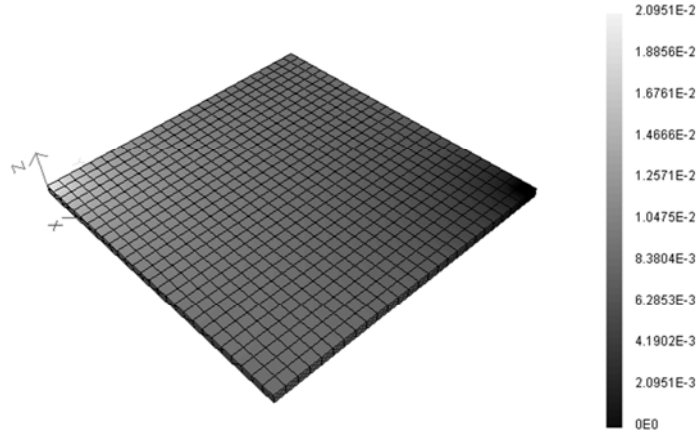


**Fig. 4 The voltage distribution as the solution of a forward problem**

#### 4. Inverse problem

The inverse problem is an optimization problem where the objective is to minimize the error between the outcome predicted by the forward problem (or the model) and the experimentally measured outcome. For the problem of interest in this project, the forward problem involves solving the governing equations of electrostatics using the finite element method to obtain voltage distribution in a composite structure. The governing equation and the natural boundary conditions are

$$\nabla \cdot ([\sigma] \cdot \nabla \phi) = 0 \quad \text{in } \Omega \quad (2.1)$$

$$J_n = -\mathbf{J} \cdot \hat{\mathbf{n}} = [\sigma] \cdot \nabla \phi \cdot \hat{\mathbf{n}} \quad \text{on } \partial\Omega \quad (2.2)$$

where,  $\phi$  is the electric potential or voltage,  $J_n$  is the normal component of the current density along the boundary  $\partial\Omega$  and  $\hat{\mathbf{n}}$  is the outward unit normal vector at the boundary.  $[\sigma]$  is the conductivity matrix of the material which is a diagonal matrix whose components are the inverse of resistivity values in the principal directions. If the material is isotropic, conductivity can be treated as a scalar  $\sigma$ .

The optimization problem for the inverse method is the minimization of the square of the error. The objective can be stated as

$$\text{Minimize } F(\mathbf{p}) = \sum_{m=1}^{n_d} (\phi_m - \phi_m^*)^2 \quad (2.3)$$

where,  $\phi_m$  is the voltage at the  $m^{\text{th}}$  electrode predicted by the model while  $\phi_m^*$  is the voltage measured at the same electrode experimentally and  $n_d$  is the number of data points or electrodes at which voltages are measured. The variables of the optimization problem are the resistivity values in the three principal directions that are the components of the vector  $\mathbf{p}$ . The resistivity values are used as variables instead of the conductivity values because the voltages have an inversely proportional relationship with the conductivities that would make the objective function highly nonlinear.

The Gauss-Newton algorithm linearly approximates the error at each iteration and then minimizes the resultant problem using the Newton's method. Therefore, this approach requires only the computation of the gradient of the error. The application of this approach to compute resistivity by minimizing the error in the computed voltages is summarized below. The gradient of the objective function defined in equation (2.3), can be expressed as

$$\frac{\partial F}{\partial \rho_i} = 2 \sum_{m=1}^{n_d} (\phi_m - \phi_m^*) \frac{\partial \phi_m}{\partial \rho_i} \quad (2.4)$$

Using Newton's method, the optimality criterion,  $\nabla F = 0$  can be solved iteratively by updating the resistivity values at the  $k^{\text{th}}$  iteration as

$$\rho_i^{k+1} = \rho_i^k + \Delta \rho_i^k \quad (2.5)$$

Where the update vector  $\Delta \rho_i^k$  is computed by solving

$$\frac{\partial F(\mathbf{p}^k)}{\partial \rho_i} + \sum_{j=1}^2 \frac{\partial^2 F(\mathbf{p}^k)}{\partial \rho_i \partial \rho_j} \Delta \rho_j^k = 0 \quad (2.6)$$

The second derivative of the objective function or the Hessian matrix can be computed as

$$H_{ij} = \frac{\partial^2 F}{\partial \rho_i \partial \rho_j} = 2 \sum_{m=1}^{n_d} \left( \frac{\partial \phi_m}{\partial \rho_i} \cdot \frac{\partial \phi_m}{\partial \rho_j} + \frac{\partial^2 \phi_m}{\partial \rho_i \partial \rho_j} (\phi_m - \phi_m^*) \right) \quad (2.7)$$

The Gauss-Newton approach involves approximating the error (or in this case voltage) as linear at each iteration so that the second derivative of the voltage is set to zero, approximating the Hessian matrix as

$$H_{ij} = 2 \sum_{m=1}^{n_d} \left( \frac{\partial \phi_m}{\partial \rho_i} \cdot \frac{\partial \phi_m}{\partial \rho_j} \right) \quad (2.8)$$

Using this approximation, equation (2.6) is solved to compute the resistivity update vector  $\Delta\rho_i^k$ . In order to implement this iterative strategy to compute the resistivity values, it is necessary to compute the gradient of the voltage with respect to the resistivity. This gradient is needed for computing both the gradient and the Hessian of the objective function. It can be computed by taking the gradient of the governing equations. The finite element method converts the governing equation (2.1), into a set of linear simultaneous equations, often express in the form,

$$[\mathbf{K}]\{\Phi\} = \{\mathbf{I}\} \quad (2.9)$$

Where  $[\mathbf{K}]$  is the global conductivity matrix,  $\{\Phi\}$  is the voltage vector containing the nodal values of the potential or voltage and the current vector  $\{\mathbf{I}\}$  contains the contribution from current applied at the boundaries. Taking the derivatives of both sides of this equation with respect to the variables  $\rho_k$ , we get,

$$[\mathbf{K}] \frac{\partial \{\Phi\}}{\partial \rho_i} = - \left( \frac{\partial [\mathbf{K}]}{\partial \rho_i} \right) \{\Phi\} \quad (2.10)$$

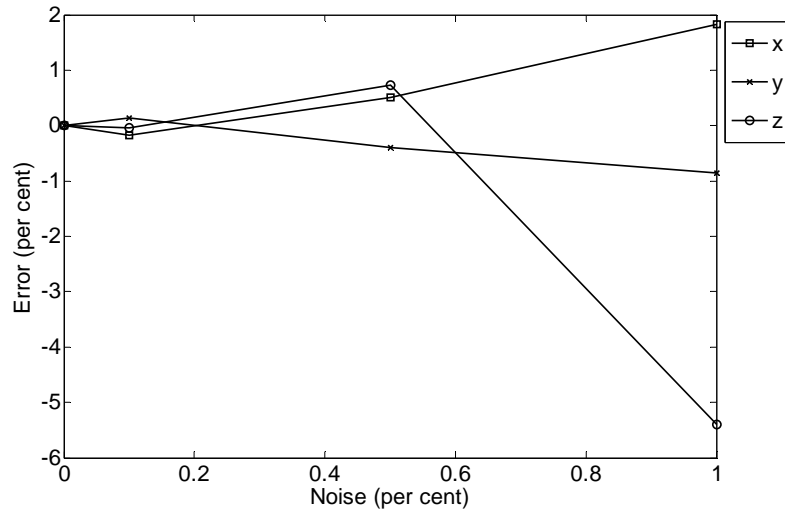
The current sources are clearly not a function of the resistivity values and therefore the current vector's derivative is zero. The right hand side of equation (2.10) can be computed element by element and assembled to create a global vector. Then the gradient of all the nodal voltages with respect to the resistivity values can be obtained by solving equation (2.10). Of course, we need the gradient only for the nodes that are located at the electrodes where the voltages are measured.

## 5. Numerical validation

The inverse approach described in the previous section was implemented on a finite element program for solving electrostatic problems. In order to first verify the validity of the algorithms and the implementation, the model itself was used to create data by computing the voltages at the electrodes using assumed values of resistivity. Then using this data in the inverse approach, the resistivity was computed starting from random values to verify if the known correct value can be computed. A plate whose dimensions are  $54 \times 52 \times 1.5 \text{ mm}^3$  was modeled for the validation. The total number of elements in the FEA model was 3024 where each element is of size  $2 \times 2 \times 0.5 \text{ mm}^3$ . A constant current of 28.9mA was applied at the electrodes. For generating the data used for inverse algorithm validation, the material was modeled as isotropic with a resistivity of  $0.01 \text{ m}\Omega\text{m}$  in all three principal directions. Using the voltage data computed using this model, the inverse problem was solved to estimate resistivity values and in this case exact solution were obtained for the resistivity. Therefore,

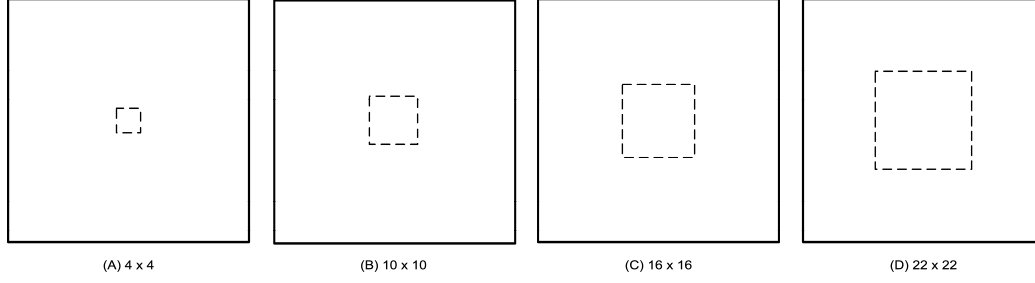
random noise from 0.1 to 1 per cent was added to the voltage data to simulate typical experimental error in measured data. The inverse problem was solved repeatedly for data with different noise levels and the effect of the added noise was evaluated to determine the resultant error in the resistivity computed by the inverse approach.

Fig. 5 shows a plot of the error in the computed resistivity values versus the percentage random noise or error introduced into the voltage data. For data with no error, all three principal resistivity values are computed with zero error but as the noise level increases the errors in the computed values increase. With 0.1% random noise added to the voltage data, the errors in the resistivity values range from 0.03% to 0.17%. In the case of 0.5% random noise, the errors are from 0.38% to 0.73% and for 1% noise, they are from 0.85% to 5.39%. Clearly, the computed values of the resistivity are sensitive to errors in the data. The resistivity in the thickness was found to be the most sensitive to the noise.



**Fig. 5 Error in computed resistivity due to noise in voltage data**

If the material does not have uniform properties, then an average value is obtained using the inverse approach. Therefore, if the material has a region with different properties due to embedded inclusions or due to damage / delamination then the computed average value would be significantly different than the undamaged uniform material's properties. This can serve as an indicator for detecting defects or monitoring damage in composite structures. To simulate this, models with varying size regions with different properties were modeled. Fig. 6 shows models with square regions that represent damaged regions that have different properties than the surrounding material.



**Fig. 6 Size and shape of the damaged region modeled in the forward problem**

All the models are plates of dimensions  $50 \times 50 \times 1 \text{ mm}^3$ , which are assumed to be made of woven composites whose conductivity values are  $\sigma_1 = \sigma_2 = 15 \text{ S/mm}$  and  $\sigma_3 = 1.5 \text{ S/mm}$ . The damaged region is assumed to have very low conductivity values:  $\sigma_1 = \sigma_2 = \sigma_3 = 1 \times 10^{-6} \text{ S/mm}$ . Using these models, voltage data at the electrodes where generated to be used as data for testing using the inverse approach. Fig. 7 shows the average values of conductivity computed by the inverse method. The largest change in conductivity occurs in the through thickness direction in this case where we have assumed that the damaged region is isotropic with very low conductivity.

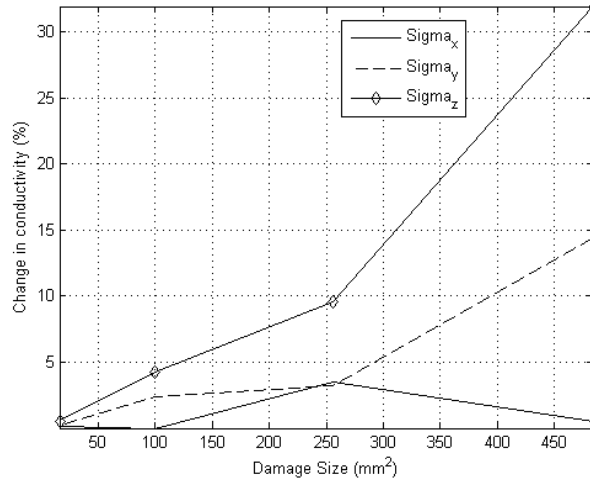


**Fig. 7 Computed average conductivity versus damage size**

## 6. Experimental Results

Several plate-like specimens made of both unidirectional and woven composites were used to make experimental measurements of the voltages on electrodes located on both sides of the plate. The voltage data measured from experimental specimen was used to determine the resistivity values, first for undamaged composite plate like specimen with uniform values of resistivity. Thereafter, specimen with artificial damage or non-uniform properties was used to determine an average value of resistivity.

## Resistivity measurement for undamaged unidirectional composite specimen

Continuous carbon fiber unidirectional composite, with 35% resin content and eleven layers, was used to prepare specimens of two different size, which are  $52 \times 47 \times 1.5 \text{ mm}^3$  for the first, and  $54 \times 52 \times 1.5 \text{ mm}^3$  for the second. Both specimen had eight electrodes, each about  $1 \times 1 \text{ mm}^2$ ; four electrodes on the top surface and the other four electrodes on the bottom surface. The unidirectional composite specimens were made by cutting it out of commercially available composite sheets. In order to make the electrodes, the electrode area was first polished with sandpaper to remove the surface layer. Thereafter, silver paint was applied to this area and after it was dried, a thin copper strip was attached to this areas using silver epoxy to adhere to copper strip and to provide good electrical contact. The measurement probes where attached to the copper strips for measuring voltages and for injecting currents. The eight electrodes were numbered as shown in Fig. 3 .

**Table I: Measurement configurations**

Current Pairs (Source, Drain)		Voltage measurement pairs (Target, Reference)				
(3,1)	(2,1)	(4,1)	(5,1)	(6,1)	(7,1)	(8,1)
(4,1)	(2,1)	(3,1)	(5,1)	(6,1)	(7,1)	(8,1)
(7,1)	(2,1)	(3,1)	(4,1)	(5,1)	(6,1)	(8,1)
(8,1)	(2,1)	(3,1)	(4,1)	(5,1)	(6,1)	(7,1)

In table I, the electrode pairs at which current was injected are listed and for each such pair voltage was measure at six different electrode pairs. Voltage difference is measured by a Keithley 2002 multimeter using the four-probe method and DC constant current magnitude of 7.235mA was injected at the current pairs.

Uncertainty of voltage measurement is about 0.0026% using Keithley 2002. In order to calculate the measurement error, 20 consequent voltage data were taken on each voltage measurement pair to calculate the average value and the standard deviation. Numerical validation results suggest that if the error in voltage data is 0.0026%, the calculated resistivity values should have less 0.1% error. However, in practice, the error can be higher due to inaccuracy in modeling the geometry of specimen, electrodes and also numerical errors in solving the forward problem. The calculated values of resistivity are an average value for the entire specimen, which is assumed to have uniform properties in the model. Two different geometrically accurate FEA models were created corresponding to the two specimens used in the experiments. The FEA model for the first specimen has 10176 elements with the element size of  $1 \times 1 \times 0.5 \text{ mm}^3$ . The second specimen has 11660 with the same element size.

Table II shows computed values of resistivity in each direction for the two specimens. For both specimen, the electrodes where modeled as current injection areas of  $1 \times 1 \text{ mm}^2$ . In the experimental specimen, it is difficult to create accurately sized

electrodes. To study the sensitivity of the results to error in modeling the electrode area, the same voltage data was used with models that used  $2 \times 2 \text{ mm}^2$  current injection regions to model the electrodes. The computed values of resistivity did not change significant indicating that it is not necessary to model the electrodes with great precision. The resistivity values, in table II, show that the resistivity in the transverse and thickness direction are several orders of magnitude larger than the resistivity in the fiber direction.

**Table II: Computed values of resistivity**

Direction	52x47x1.5 mm <sup>3</sup> specimen	54x52x1.5 mm <sup>3</sup> specimen
Fiber direction	0.024 mΩm	0.020 mΩm
Transverse direction	18.6 mΩm	13.4 mΩm
Thickness direction	67.5 mΩm	60.0 mΩm
Least square error:	$5.25 \times 10^{-6}$	$3.68 \times 10^{-3}$

### Woven composite specimen with and without damage

Resistivity values were determined for woven composite specimen also using the same procedure. To study the effect of damage, artificial damage was introduced by embedding Teflon patches between the layers. We fabricated both the damaged and undamaged specimen using four layers of woven carbon fiber prepregs. To create the damaged specimen, Teflon patches were introduced between the first and second layers as well as the third and fourth layers as shown in the Fig. 8 . The specimen size was  $50 \times 50 \times 1 \text{ mm}^3$  and the size of the Teflon patches were  $10 \times 10 \text{ mm}^2$  and they were centrally located within the specimen. Eight electrodes attached at the corners of the specimen were used to gather voltage data. The electrodes were created by inserting copper strips between the first and second layers as well as between the third and fourth layers of prepreg before curing. This method avoids the need for attaching electrodes with silver epoxy and it provides better contact as well as robust connection that are not easily damaged.

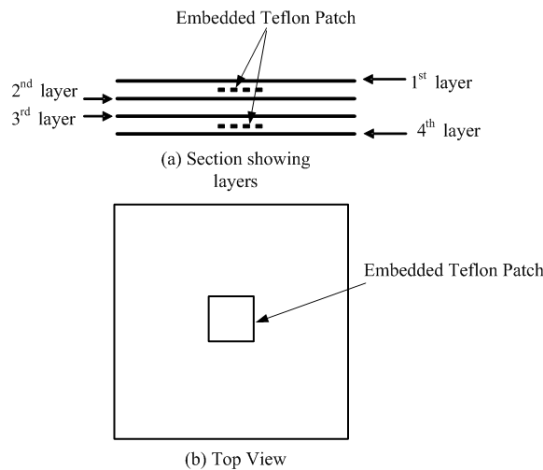


**Fig. 8 Woven fiber composite prepregs with embedded Teflon patches**

To determine the resistivity, three undamaged specimen and three Teflon embedded specimen were used. The results obtained are listed in Table III, which shows values for resistivity for the six specimen and the average values. Clearly, there is significant change in resistivity due to the Teflon embedding that can be detected using the resistivity measurement technique described here. This approach therefore has potential to be used for quality control, to detect manufacturing defects such as voids and air gaps as well as delamination or damage that may occur during usage.

**Table III: Resistivity values for woven fiber composite specimen**

Specimen No.	Specimen without teflon	Specimen with Teflon
1	$\sigma_1 = 15.39[\text{S/mm}]$ $\sigma_2 = 17.25[\text{S/mm}]$ $\sigma_3 = 1.617[\text{S/mm}]$	$\sigma'_1 = 9.4086[\text{S/mm}]$ $\sigma'_2 = 11.88[\text{S/mm}]$ $\sigma'_3 = 0.9708[\text{S/mm}]$
2	$\sigma_1 = 13.46[\text{S/mm}]$ $\sigma_2 = 18.15[\text{S/mm}]$ $\sigma_3 = 1.18[\text{S/mm}]$	$\sigma'_1 = 9.2415[\text{S/mm}]$ $\sigma'_2 = 8.539[\text{S/mm}]$ $\sigma'_3 = 0.7438[\text{S/mm}]$
3	$\sigma_1 = 22.86[\text{S/mm}]$ $\sigma_2 = 22.32[\text{S/mm}]$ $\sigma_3 = 1.02[\text{S/mm}]$	$\sigma'_1 = 8.2043[\text{S/mm}]$ $\sigma'_2 = 8.9204[\text{S/mm}]$ $\sigma'_3 = 0.8232[\text{S/mm}]$
Average	$\sigma_1 = 17.24[\text{S/mm}]$ $\sigma_2 = 19.24[\text{S/mm}]$ $\sigma_3 = 1.272[\text{S/mm}]$	$\sigma'_1 = 8.9515[\text{S/mm}]$ $\sigma'_2 = 9.7798[\text{S/mm}]$ $\sigma'_3 = 0.8459[\text{S/mm}]$

## 7. Discussion

An algorithm for solving inverse problem to determine average resistivity values in composite structures was demonstrated. The method can use data from an arbitrarily large number of electrodes to compute average values of resistivity or conductivity for the structure. Finite element models for the structure are used to solve the forward problem, making this method very general and applicable to arbitrary shaped structures. Ideally, the electrodes should be embedded in the structures during the manufacturing process itself so that it can be used for quality control, detection of defects as well as subsequent health monitoring. One of the advantages of measuring resistivity is that damage can be detected even in structures that were not tested during manufacturing. Damage can be detected for structures that are in use by attaching electrodes on the surface, determining the average resistivity and comparing it to values associated with undamaged material. The main source of error in this approach arises from inaccuracy in the geometric models of the structure and the electrodes. Random noise added to the voltage data used in numerical validation indicates that any error in the voltage data can get amplified due to difficulties in numerical convergence.



In principle, a similar inverse approach can also be used to determine applied loads on the structure. Preliminary experimental studies indicate that this may be difficult because the changes in the electrode voltage due to strains can be very small. Even with amplification, the data is hard to use because of significant non-linearity in the observed behavior. However, the approach we developed is promising for detecting damages or defects because they cause significant changes in resistivity and is therefore easier to detect. Further study is needed to explore ways of determining applied loads and strains.

This page intentionally left blank

### III. COMPOSITE ACTUATING STRUCTURES

#### 1. Overview

Polymer matrix composites are widely used as a structural material in a variety of aerospace applications including commercial jets, unmanned air vehicles as well as micro air vehicles. In many of these applications weight is an important constraint and available space is very limited. This provides an incentive to pack as much functionality as possible into the structure itself by making it multifunctional. For air vehicle applications, structures with actuation ability are particularly desirable for designing active structures such as morphing wings/body panels or flapping wing like structures. Methods of actuation studied in the past have mainly consisted of embedded piezoelectric fibers and patches. In this project, electromagnetic means of actuation were studied wherein embedded ferromagnetic materials are used for the actuation using external or internally generated magnetic fields.

Composite structures made of epoxy matrix and carbon fiber reinforcement have excellent structural properties including stiffness/rigidity and high strength. Therefore, many aircraft structures are made of such composites, particularly in unmanned and micro air vehicles. Due to the conductivity of carbon fibers, it is possible to conduct currents through these composites. Magnetic field can be generated in composite structures by current flowing through the reinforcing fibers/conducting wires as well as due to embedded permanent magnets. The magnetic forces generated on the structure can be large enough to cause deformation if ferromagnetic materials are embedded in the structure and large currents are flowing through the structure. Unlike in traditional electrical machinery, structures that are meant to actuate are designed to deform significantly due to the magnetic forces. Therefore the structure cannot be treated as a rigid body and its deformation needs to be computed using an analysis model that couples the magnetic and structural models. To compute the resultant deformations, strains, and stresses, a two stage analysis approach is adopted here. The magnetostatic problem is solved first to compute the magnetic flux density and field distribution. This result is then used to compute the body forces generated on the structure due to magnetic forces. In the second stage a solid mechanics analysis is performed using these magnetic forces to compute the mechanical deflections. In general if these deflections are large, causing the current carriers and embedded soft and hard magnets to move significantly relative to each other, then the movement would alter the magnetic field, requiring an iterative solution. However, in this project, only linear elastic deformation with a two stage analysis as described was considered. For the type of actuators that is most appropriate for this application, linear models are sufficient as described in later chapters. The structure is also modeled as linear elastic since the deformation of the

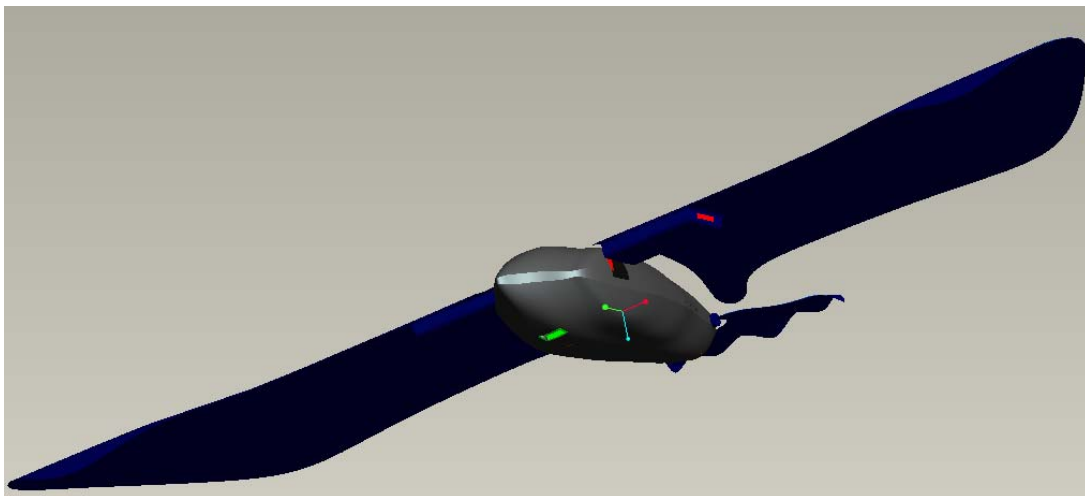
mechanism is reversible. It would be beneficial in future work to incorporate large deformation models to simulate the full range of motion of highly flexible structural mechanisms.

## 2. Motivation for structural actuators

The primary application that serves as motivation for this work is the design of micro air vehicles (MAV) and unmanned air vehicles (UAV). The goal was to develop computational tools for design and analysis of magnetically actuated structural mechanisms for these air vehicles so that structural components of the vehicle including wings, fuselage and tail can be designed function as structural actuators. Therefore, rather than have external mechanisms, linkages, motors or actuators to produce the necessary motions, the structure is designed to deform in specified manner due to built-in magnetic actuation capabilities. This would allow these structures to flex or change shape for morphing applications as well as oscillate or vibrate to produce flapping motion.

Fig. 9 shows the conceptual design of a simple flapping wing actuation mechanism where the wings are attached to a flexible structural support that is actuated by the electromagnets built-into this support. The key design challenges for this concept include:

- (i) Designing magnetic actuators that are strong enough to produce the necessary deformation
- (ii) Designing the support structure and wing such that the desired motion is produced when the actuating magnets are activated
- (iii) Designing the dynamics of the wing so that at resonance the flapping motion will produce the desired mode of vibration that can generate thrust and lift.



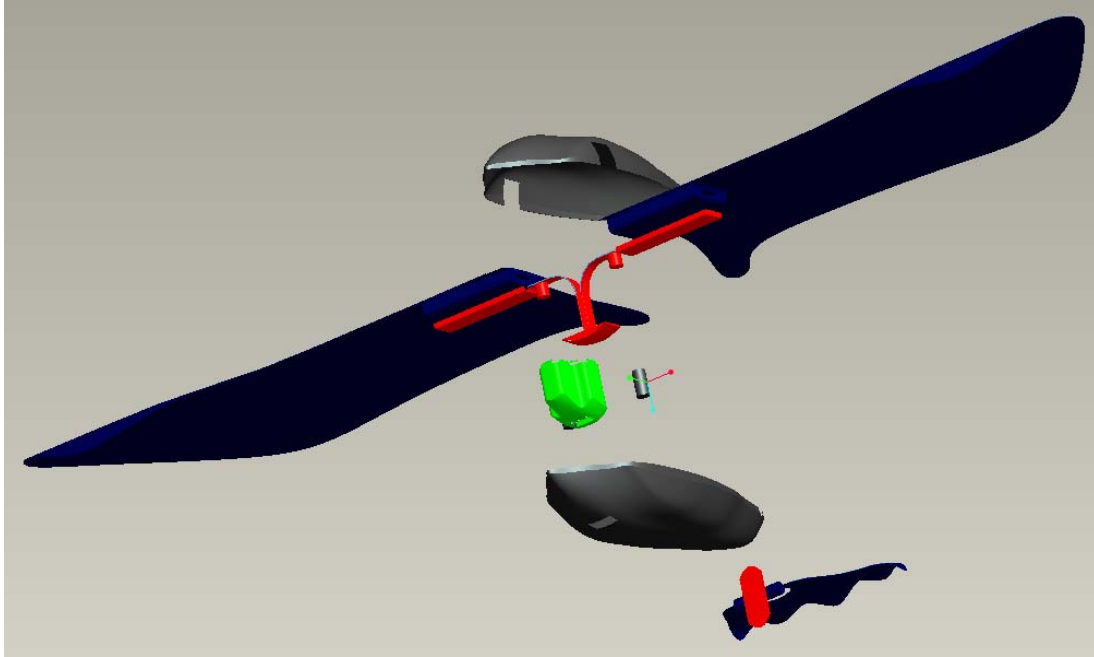


**Fig. 9 Flapping wing conceptual design**

The actuator can be better integrated with the structure if the deforming component is built as part of the wing structure. A design based on this concept is shown in Fig. 10 .

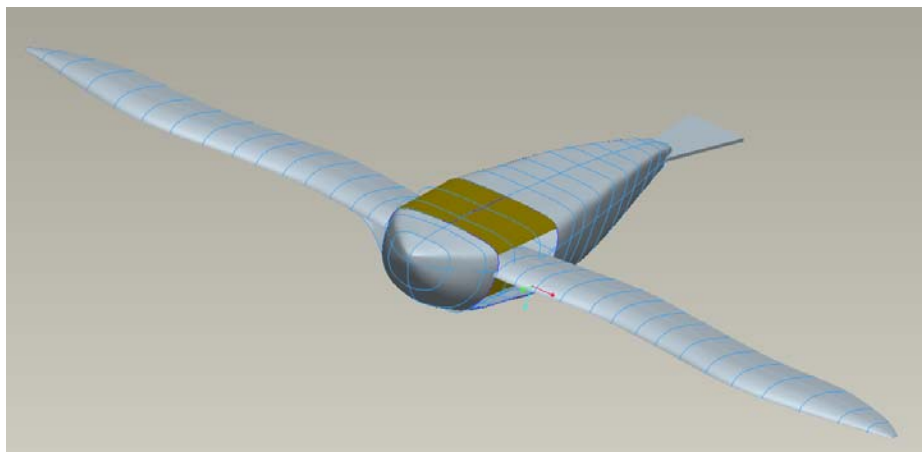


**Fig. 10 Alternate design of actuator**

The structure is designed to be compliant so that it can deform to produce the desired actuation. The idea is illustrated using a simple wing design in Fig. 11 where the magnetic forces are shown as acting along the edge of half of the wing assembly. The force causes the wing structure to deform to produce the flapping motion. The actual deformation mode will depend not only on the shape of the wing and the

support but also on the reinforcements, fiber direction and number layers in the composite shell.



**Fig. 11 Deforming structural mechanism**

In order to design the embedded actuators, it is necessary to have the ability to compute the magnetic field produced by the actuator, compute forces on structures and then compute the deformed shape of the structure due to these forces. To design the structure itself, we would like to compute the shape of the support structure, the orientation of the fibers of the composite, the possible location of holes or reinforcements such that the structure would deform or oscillate in the desired mode. A possible design tool for computing the geometry and reinforcement is topology optimization. This idea was explored as part of this project and some of the results are presented in the next section.

### **3. Designing the shape and topology of structural actuator**

In order to design the shape of the structure that is appropriate for the desired actuation, the geometry design problem is stated as a design optimization problem. Firstly, a region within which the geometry must fit is defined as a feasible region. The geometry is defined within this region as the level set or contour of a density function (or the characteristic function). Contours of this function corresponding to a threshold value are defined as the boundaries of the shape so that regions where the value of the function is below the threshold are not part of the geometry. Hence, the boundary may be defined using the following implicit equation

$$\phi(x, y) - \phi_{th} = 0 \quad (3.1)$$

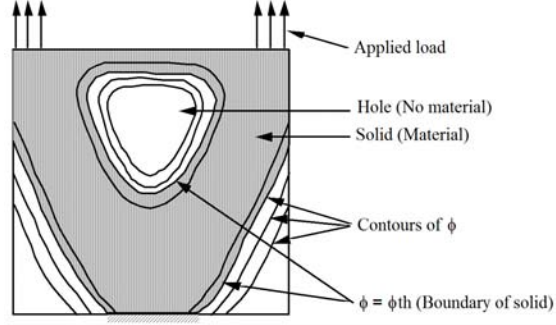


**Fig. 12 Shape representation using shape density function**

In traditional topology optimization methods, porosity or density of the material is treated as constant within each element. In this work, the density was assumed to vary continuously within the feasible region. Fig. 12 illustrates this shape representation where the rectangle represents the feasible region, the arrows at the top represent a uniformly distributed load and the structure is to be supported at the bottom. A mesh is generated for the feasible region and the density function is defined within this feasible region by piece-wise interpolation within elements of the mesh. Contours of the density function are plotted in the figure. The contour of the density function corresponding to the threshold value  $\phi_{th}$  is the boundary of the solid and the regions with higher values of density is the interior of the solid shown as the shaded region in the Fig. 12. In this example, there are multiple contours that correspond to the threshold value each representing part of the boundary. Shape representation using a contour of the density function enables the entire geometry to be treated as a variable. By changing the density function it is possible to not only modify existing boundaries but also to create new internal boundaries.

The density function  $\phi = 1$ , where the material is fully dense and  $\phi \leq \phi_{th}$  where there is no material. The density function can also take on intermediate values but as explained later the relation between density and material properties is selected such that the optimal designs are close to fully dense. A new internal boundary corresponding to a hole, for example, would be created if the value of the density function decreases to the threshold value in a region.

To define the density function, the feasible domain is divided into triangular or rectangular elements. The density function is interpolated within each element. A contour of the density function corresponding to the threshold value passes through the element if some nodes of the element have nodal density values higher than the threshold value while others have values below. In this project, linear or bilinear elements as well as B-spline elements were used. The contour is therefore plotted by joining the points along the contour that has density value equal to the threshold value. A  $C^0$  continuous density function ensures  $C^0$  continuous boundaries for the final shape,

whereas, quadratic and cubic B-spline elements provide a  $C^1$  and  $C^2$  continuous density functions and contours respectively.

The mesh used for defining the density function can also serve as the finite elements for structural analysis. The values of the density function at the nodes serve as the design variables of the optimization problem. Initially, the nodal density values are set equal to unity for all the nodes so that the geometry is identical to the feasible region. During the optimization process the nodal density values,  $\phi_i$  are modified by the optimization algorithm which iteratively searches for the optimal values of the nodal densities such that the defined objective function is minimized.

For the application of interest in this project, the objective is to design a structure that deforms in a particular fashion when subjected to electromagnetic forces. Therefore the objective function is defined as the error between the desired deflection and the actual deflection. In this project, the method was applied only to planar (2D) problems, such as plane stress and plane strain. In addition to minimizing this objective function, a constraint on the total mass of the structure is applied.

Structural synthesis is the inverse of the structural analysis problem. The structural analysis problem is typically stated as a principle of virtual work (PVW),

$$\int_{\Omega} \{\delta \varepsilon\}^t [\mathbf{D}] \{\varepsilon\} d\Omega = \int_{\Omega} \mathbf{f}_b \cdot \delta \mathbf{u} d\Omega + \int_{\Gamma_t} \mathbf{f}_s \cdot \delta \mathbf{u} d\Gamma \quad (3.2)$$

The domain  $\Omega$  represents the shape and topology of the component whose structural properties are being analyzed. The finite element method is used to solve for the displacement field  $\mathbf{u}(\mathbf{x})$  for every  $\mathbf{x}$  belonging to  $\Omega$ .

The shape and topology synthesis problem involves solving for a domain  $\Omega$  that optimizes some structural property for given loading and boundary conditions. The geometry  $\Omega$  is defined as the region within the original feasible domain  $\Omega_0$  where the shape density function has a value greater than the threshold value. The minimization problem can be stated as

$$\text{Minimize } \Pi(\phi) = \sum_{i=0}^m (u_i - u_i^*)^2 \quad (3.3)$$

subject to,

$$M(\phi) = \int_{\Omega} \phi d\Omega \leq M_0 \quad (3.4)$$

$$\int_{\Omega_0} \{\delta \varepsilon\}^t [\mathbf{D}(\phi)] \{\varepsilon\} d\Omega \quad (3.5)$$



$$\phi_{th} \leq \phi \leq 1 \quad (3.6)$$

$\Pi(\phi)$  is the sum of the square of errors in the computed nodal displacement at nodes where a desired value of displacement has been specified, where,  $\phi(\mathbf{x})$  is the density function. It is assumed that a desired value of displacement  $u_i^*$  has been specified at 'm' nodes and  $u_i$  is the computed value of the displacement. Equation (3.4) describes the constraint that the mass  $M$  of the component should be less than or equal to a specified value  $M_0$ .

The optimization problem stated in equations (3.3)-(3.6) can be solved using mathematical programming techniques or optimality criteria methods. The objective function is non-linear and the constraint on weight is linear. Each evaluation of the objective function requires a computationally expensive finite element analysis to compute the displacement at the nodes of the finite element mesh for the structure. Therefore, an algorithm that does not require excessive number of function evaluations is preferred. A modified form of sequential linear programming [29] was used for the results presented in this report.

When the shape defined by the density function varies, the structural properties must vary accordingly. This implies that the material property coefficients defined in the matrix  $[D]$  must depend on the density function  $\phi(x,y)$ . We seek relations that are simple and therefore easy to integrate over each element when density varies linearly within each element. In addition we would like relations that lead to clearly defined topologies so that the final shape obtained is fully dense and the density function transitions sharply at the boundary from full density to the lowest possible (threshold value).

The material property-density relation should be such that if the density decreased in a region, the stiffness should decrease causing the material to become weaker in that region. This would be achieved if the slope of the objective function with respect to the variables,  $\frac{\partial}{\partial \phi_i} \Pi(\mathbf{u})$ , is negative. The optimization algorithm would therefore decrease the density in regions where material is under-utilized causing either new boundaries (holes) to be created in such regions or causing existing boundaries to shrink inwards. We have used some linear and non-linear material property density relations that satisfy this criterion.

Homogenization method has been used to determine the relation between porosity (or density) and elastic constants by assuming a microstructure. Typically a square unit cell with a circular, square or rectangular void is used to determine the elastic constants. The size of the void is changed to vary the porosity (or density) and the elastic constant are computed for various values of porosity. Since the

homogenization process is computationally expensive the elastic constants are computed for a few values of porosity and then a curve is fitted over these computed points to obtain a relation. However, the relation obtained is not unique because it depends on the microstructure assumed. The optimal designs that are obtained will also be therefore different based on the assumption used. This raises the question as to which relation is ideal for computing optimal shapes. Since the real material does not have varying density or porosity it is preferred that the optimal designs are fully dense. Any relation that leads to such design is therefore preferable.

In our implementation, polynomial relation was assumed between elastic constant and the density function. For example, it can be assumed that the elastic modulus of the material is a quadratic function of the density. Similarly, one could use higher order approximations. Just as different microstructure assumptions lead to different optimal designs when homogenization method is used, different polynomial relations between elastic modulus and density lead to different designs. The criterion that we used for selecting the relation is the sharpness of the density transition at the boundary. In other words, we want the material inside the shape to be fully dense ( $\phi=1$ ) and the material to have the lowest possible density where the holes are located. At the boundary we want the density to transition sharply from the highest value to the lowest value, so that we have clear and well defined boundaries. When a linear relation is assumed sharp boundaries are not obtained except when the threshold value is set close to 1. It was found that in general, higher order approximations of the material property-density relations lead to the desired behavior.

Assuming  $p^{\text{th}}$  order polynomial relation between the elasticity modulus and the density function, we get the following material property-density variation for plane stress problems,

$$\begin{aligned} d_{11} &= \frac{E\phi^p}{1-\nu^2} \\ d_{12} &= \frac{E\nu\phi^p}{1-\nu^2} \\ d_{33} &= \frac{E\phi^p}{2(1+\nu)} \end{aligned} \tag{3.7}$$

The coefficients  $d_{ij}$  are the elements of the elasticity matrix. Note that in the above relation we do not assume that Poisson's ratio changes with density and therefore, for this approximation the material coefficients reduce to zero as density goes to zero, that is,  $d_{ij}=0$  for  $\phi=0$ . The elasticity matrix can then be conveniently defined as

$$[\mathbf{D}_p(\phi)] = [\mathbf{D}]\phi^p \tag{3.8}$$

where,  $[D]$  is the elasticity matrix for plane stress or plane strain.

In order to use a mathematical programming algorithm to compute the optimal design, it is necessary to compute the gradient of the objective function and the constraint. The gradient of the objective function is:

$$\frac{\partial \Pi}{\partial \phi_i} = \sum_{i=1}^m 2(u_i - u_i^*) \frac{\partial u_i}{\partial \phi_i} \quad (3.9)$$

The gradient of nodal displacements can be computed using the standard design sensitivity analysis methods. The equilibrium equations are reduced to a set of linear simultaneous equations by the finite element method which is usually expressed as

$$[\mathbf{K}]\{\mathbf{U}\} = \{\mathbf{F}\} \quad (3.10)$$

$\{\mathbf{U}\}$  is the displacement vector that contains  $u_i$ , the displacement components at the nodes and  $\{\mathbf{F}\}$  is the load vector. The gradient of  $u_i$  can be computed by solving the equation

$$[\mathbf{K}] \frac{\partial \{\mathbf{U}\}}{\partial \phi_i} = \{\lambda\} \quad (3.11)$$

where,  $\{\lambda\}$  is the adjoint variable that is computed as

$$\{\lambda\} = -\frac{\partial [\mathbf{K}]}{\partial \phi_i} \{\mathbf{U}\} \quad (3.12)$$

## 4. Examples of Topology Design

### Gripper Mechanism Design

As an example, let us consider the design of a mechanical gripper. The mechanism is supported at the two corners on its left edge and input forces of magnitude 50000 N are applied in the middle of the left edge as shown in Fig. 13 . Vertical displacements desired at the points A and B that causes them to move towards each other or to grip a work-piece. Forces of magnitude 5000 N are applied at the points A and B, where displacements are expected, to model the resistance of the work-piece once the mechanism comes in contact with the work-piece.

The size of the design domain is 5 x 5 m as shown in Fig. 13 . Displacements of magnitude 0.00025 are prescribed at two corner points A and B and displacements of magnitude 0.000025 are prescribed at the points where the input forces are applied.

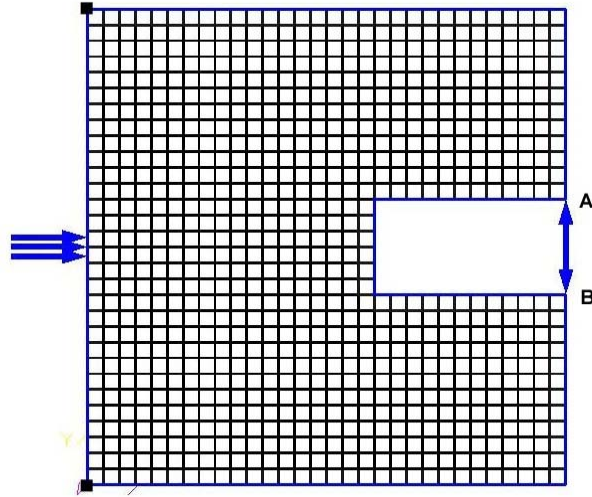


**Fig. 13 Feasible domain for gripper mechanism design with a 30 x 30 mesh**

The material of the domain is assumed to be steel with modulus of elasticity equal to 200 GPa and the Poisson's ratio of 0.3. The original domain has been discretized with a sparse mesh of 30 x 30 elements.

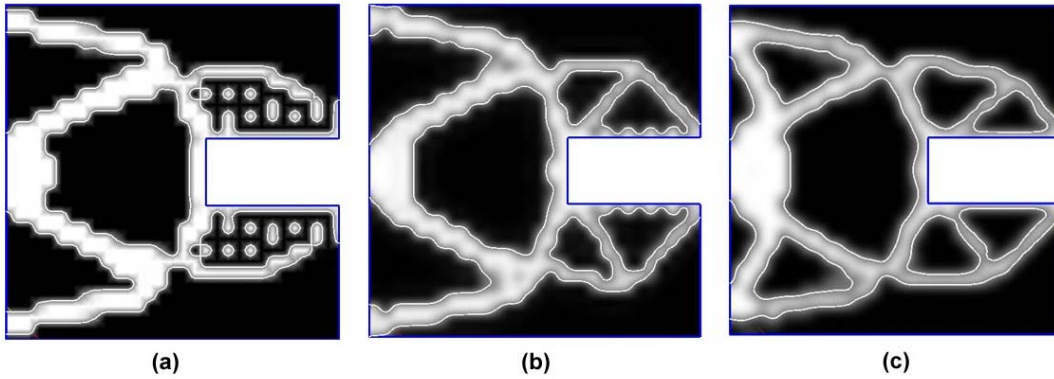


**Fig. 14 Topology results for a mechanical gripper design with a 30 x 30 mesh using (a) Quad 4N elements (b) B-spline 9N elements (c) B-spline 16N elements**

The topology results of the optimal designs are shown in Fig. 14 . The topology designs are obtained using bilinear 4 node quad, B-spline 9 node and B-spline 16 node elements. SIMP interpolation method with the penalty parameter  $p = 4$  for the density function and the allowable material volume fraction of 0.3 is used. It can be observed that with the use of sparse mesh, the bilinear quad 4-noded elements results in a shape that is not well connected and have problems in smooth representation of the boundaries. The optimal geometries obtained using B-spline elements are well connected and smoother without any checkerboard patterns.

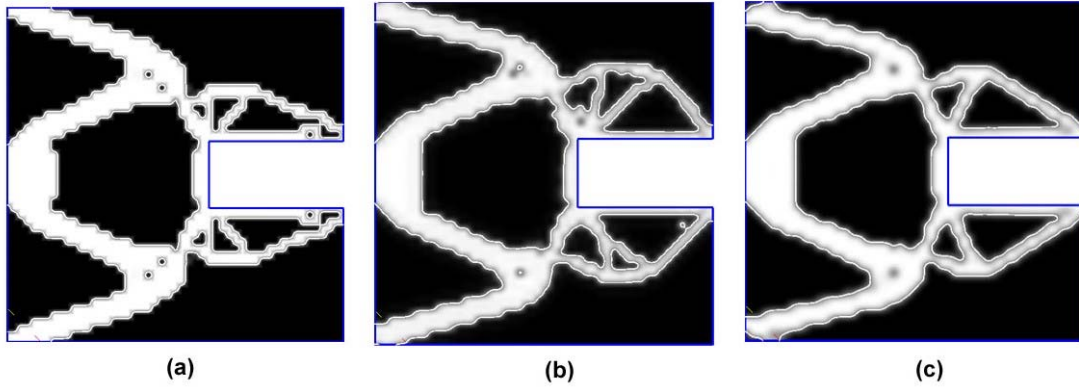


**Fig. 15** Topology results for a mechanical gripper design with a 50 x 50 mesh using (a) Quad 4N elements (b) B-spline 9N elements (c) B-spline 16N elements

The topology results with an increased mesh refinement of 50 x 50 elements are shown in Fig. 15 for quadrilateral 4-node (Q4), B-spline 9-Node and B-spline 16-Node elements. It can be observed that with the increase in mesh refinement, even the Q4 elements converge to a better smooth shape and the B-spline elements also converge to better smooth shapes.

To evaluate the validity of the designs obtained using B-spline elements in IBFEM, finite element models similar to the optimal designs were created using the commercial FEA package ABAQUS. The finite element model of the optimal design along with the loads and boundary conditions are shown in Fig. 16 . Bilinear quadrilateral 4-noded plane stress elements are used for the analysis. A superimposed image of the deformed and un-deformed shapes of the geometry is shown in Fig. 16 (b). The deformation of the mechanism was indeed in the direction as intended. Thus, the designs obtained for the gripper mechanism are indeed valid.

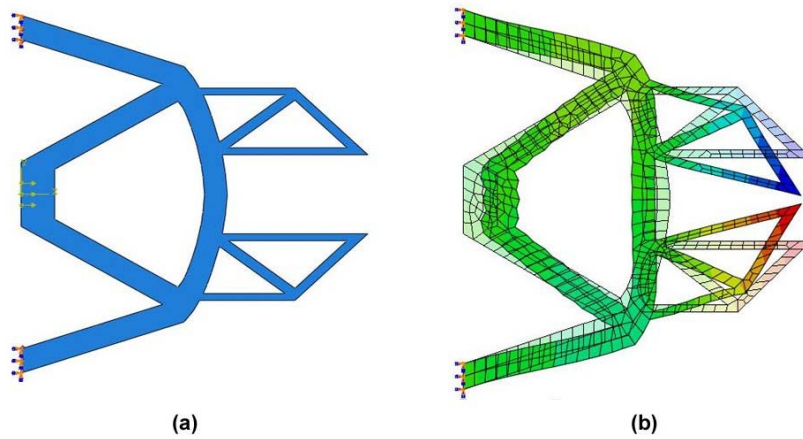


**Fig. 16 Results from ABAQUS for the gripper mechanism (a) FE Model of the gripper mechanism with loads and boundary conditions (b) Deformed shape of the gripper mechanism**

### Displacement Inverter Mechanism Design

The feasible domain for the design of a displacement inverter mechanism is shown in Fig. 17 . The mechanism is supported at the two corners along its left edge and input forces of magnitude 50000 N are applied at the middle of the left edge as shown in Fig. 17 . Displacements are expected at the output ports at the middle of the right edge in the negative x-direction. Forces of magnitude 5000 N are applied at the output ports in the direction x opposite to the direction in which displacements are required.

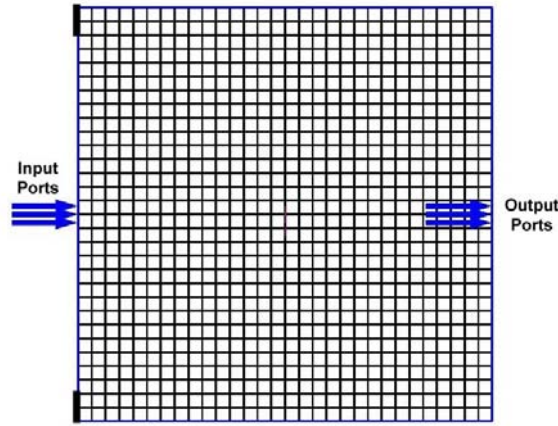


**Fig. 17 Feasible domain for displacement inverter design with a 30 x 30 mesh**

The size of the design domain is 5 x 5 m as shown in Fig. 17 . Displacements of magnitude  $-1 \times 10^{-6}$  (in the negative x-direction) are specified at output ports and displacements of magnitude  $1 \times 10^{-5}$  are specified at the points where the input forces are applied. The material of the domain is assumed to be steel with modulus of elasticity equal to 200 GPa and the Poisson's ratio of 0.3. The original domain has been discretized with a sparse mesh of 30 x 30 elements.

The topology results of the optimal designs for the inverter mechanism are shown in Fig. 18 . The topology designs are obtained using bi-linear 4 node quad, B-spline 9 node and B-spline 16 node elements. SIMP interpolation method with the penalty parameter  $p = 4$  for the density function and the allowable material volume fraction of 0.2 is used.

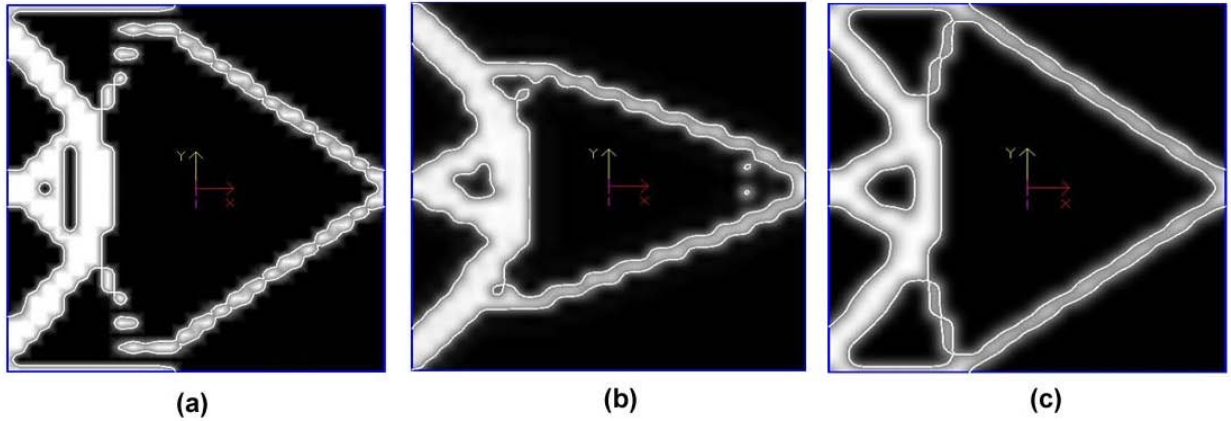


**Fig. 18** Topology results for a displacement inverter design with a  $30 \times 30$  mesh using (a) Quad 4N elements (b) B-spline 9N elements (c) B-spline 16N elements

With the use of a sparse mesh of  $30 \times 30$  elements, the design obtained using bilinear quad 4-noded elements is not well connected and the boundary representation is not smooth. On the other hand, B-spline elements result in geometries that have smooth and clear boundaries. Checkerboard pattern is inherently eliminated in B-spline elements.

The second part of this example is performed on a similar feasible domain with a refined mesh discretization. A refined mesh discretization of  $50 \times 50$  elements was used to validate if the topologies obtained would be any different from the topologies obtained using a sparse mesh. The topology results of the optimal designs are shown in Fig. 19 . With a refined mesh, the design obtained using bilinear Quad 4-node elements has considerably improved with clear boundaries. B-spline elements also result in geometries that have smooth and clear boundaries.

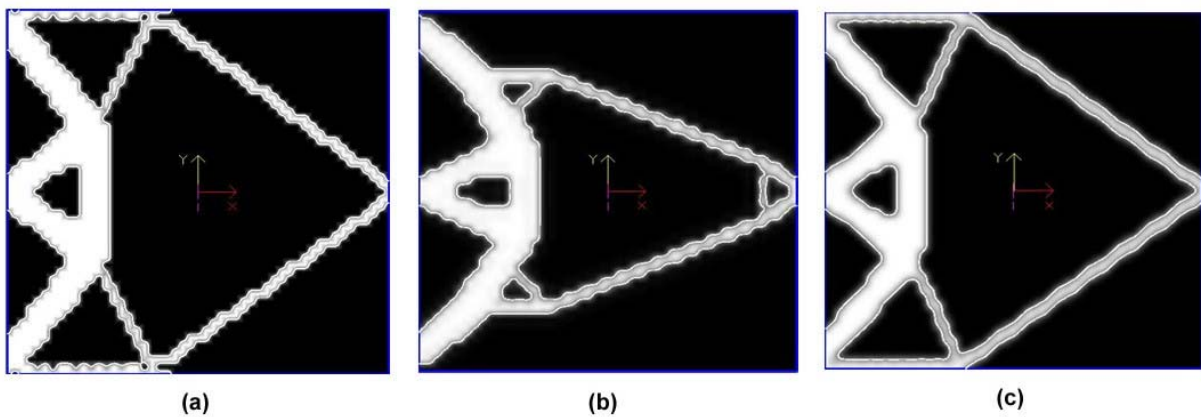


**Fig. 19** Topology results for a displacement inverter design with a  $50 \times 50$  mesh using (a) Quad 4N elements (b) B-spline 9N elements (c) B-spline 16N elements



The designs obtained using B-spline elements in IBFEM were validated using a commercial FEA package to evaluate the working of the displacement inverter mechanism. Commercial FEA package ABAQUS is used to evaluate the designs. The finite element model of the optimal design of the displacement inverter mechanism along with the loads and boundary conditions is shown in Fig. 20 (a). Bilinear 4-noded quadrilateral elements are used for the analysis. Fig. 20 (b) shows the superimposed image of the deformed and un-deformed geometries. The tip of the inverter is expected to move in the negative x-direction when a force is applied in the positive x-direction on left edge. The deformed shape shows that the designs obtained for the inverter mechanism are valid.

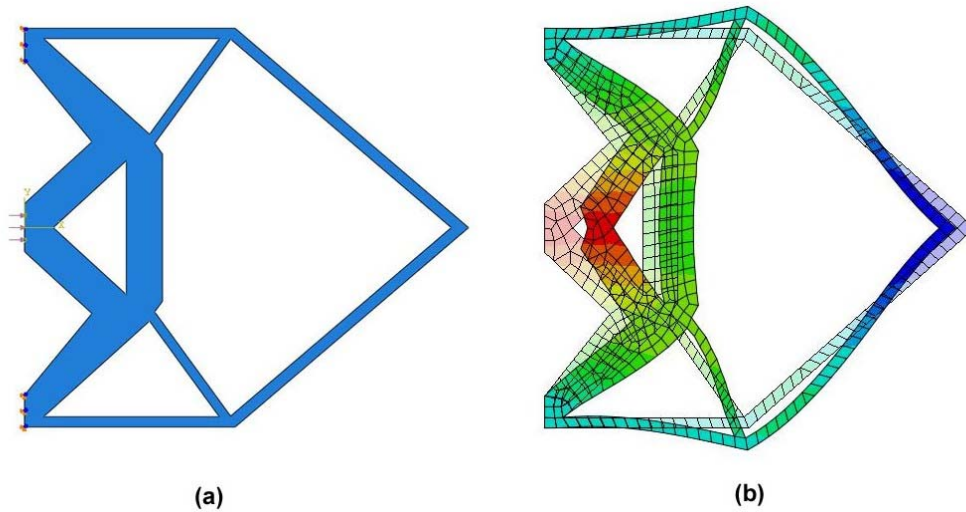


**Fig. 20 Results from ABAQUS for the inverter mechanism (a) FE Model of the inverter mechanism with loads and boundary conditions (b) Deformed shape of the inverter mechanism**

B-spline elements thus demonstrate the ability to obtain the optimal shapes even with sparse mesh discretizations when compared with the bilinear quadrilateral elements which required dense mesh discretization to obtain similar optimal shapes.

### Flapping Wing Mechanism

A flapping wing mechanism for a micro air vehicle is to be designed to obtain large displacements at the tip of the wings. The wings will be activated by an magnetic actuator placed in the fuselage. The shape of the casing for the actuator is to be obtained using topology optimization so that it functions as a compliant mechanism as well as the support for the wing. The feasible domain for the flapping mechanism with a mesh size of  $70 \times 35$  elements is shown in Fig. 21 . A polynomial power of  $p = 3$  and a volume fraction of 0.5 is used to obtain the optimum topology results. The material of the



structure is assumed to be steel with a modulus of elasticity 200 GPa and Poisson's ratio of 0.3.

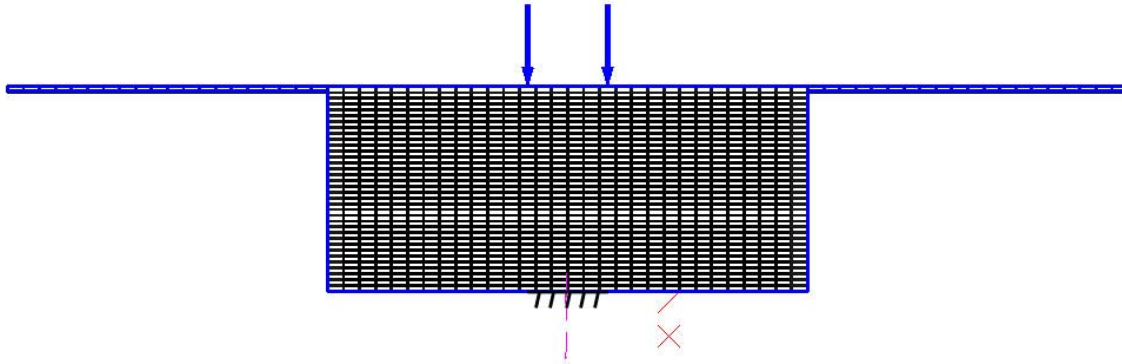


**Fig. 21 Feasible domain for a flapping wing mechanism with 70 x 35 elements**

Displacements of magnitude  $2 \times 10^{-5}$  are specified at the wing tips and the entire structure is fixed at the centre of the bottom edge. The topology results obtained using bilinear 4-node quadrilateral elements, B-spline 9N elements and B-spline 16N elements are shown in Fig. 22 .

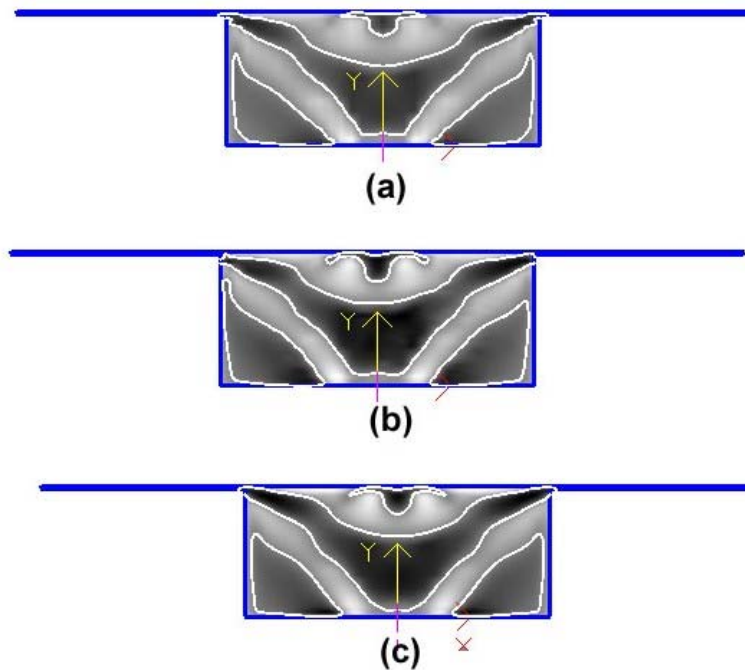


**Fig. 22 Topology results for the flapping mechanism for a 70 x 35 size mesh and a volume fraction of 0.5 (a) Quad 4N elements (b) B-spline 9N elements (c) B-spline 16 N elements**

To validate the design of the mechanism obtained using topology optimization, a finite element analysis is performed on the final topology of the structure. Fig. 23 shows a superimposed image of the deformed shape on the optimum structure. As expected a displacement of  $2 \times 10^{-5}$  is obtained at the wing tips as shown proving the validity of the design.

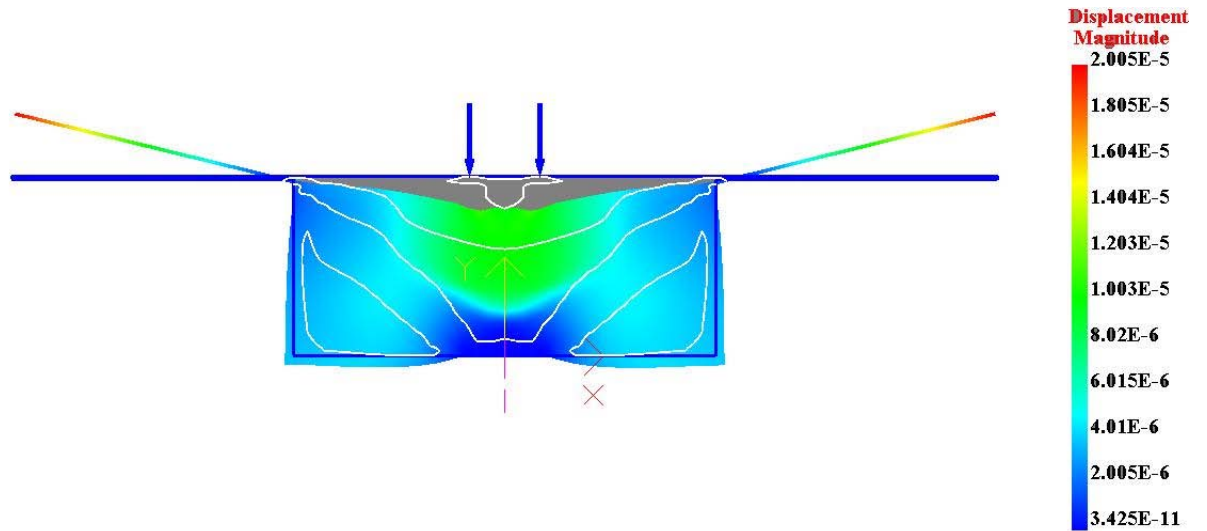


**Fig. 23** Results from a finite element analysis on the optimum structure for the flapping mechanism

## IV. MAGNETOSTATIC ANALYSIS USING IMPLICIT BOUNDARY FINITE ELEMENT METHOD

### 1. Overview

Magnetostatic analysis and force computation for magnetically actuated devices involves modeling an assembly of components with different material properties. When traditional finite element method is used for such analysis, it requires a conforming mesh that approximates the geometry of the assembly. The mesh must contain nodes along the external boundaries and the interfaces between parts. The edges / faces of the elements must approximate these boundaries and interfaces as shown in Fig. 24 . Often the geometry is not well approximated. Generating such a mesh is difficult and, despite decades of research, 3D mesh generation (especially using hexahedral elements) is still not a fully automated process and in fact requires significant user input. To address mesh generation difficulties several meshless methods [30] have been proposed that still need a well-placed distribution of nodes but do not require these nodes to be connected into elements. Some of these methods have been successfully used for magnetostatic analysis [31]-[36]. These methods use interpolation and approximation schemes that do not need connectivity between nodes. However, computationally these methods are significantly more expensive and they still approximate boundaries and interfaces using nodes along them.

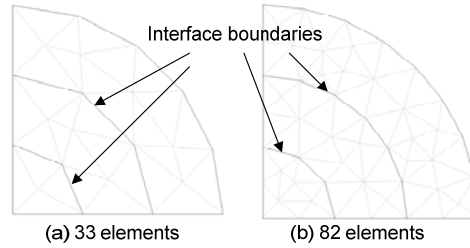
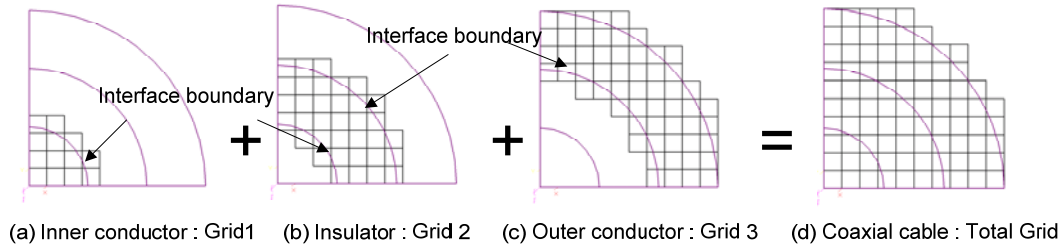


**Fig. 24 2D FEM mesh**

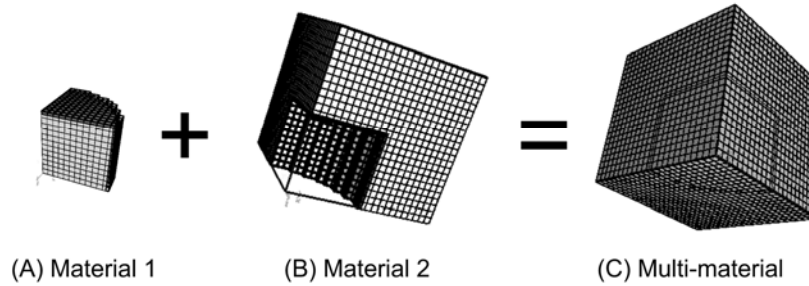
An alternate approach to avoid mesh generation difficulties is to use a structured background mesh to represent the solution while using accurate equations of curves and surfaces to represent the boundaries. A structured mesh consists of uniform regular shaped elements and is therefore easy to generate. Extended finite element method (X-FEM) [37]-[39] is one such method, which uses a structured mesh and implicit equations for the boundaries and interfaces. In the X-FEM approach, the solution is enriched near singularities and discontinuities such as cracks. An important application of this method has been fracture mechanics, where crack propagation [40]-[41] is simulated by modifying the equations of the crack rather than regenerating the mesh. Boundary and

interface conditions have been imposed using Lagrange multiplier and Penalty methods for X-FEM.

The Implicit Boundary FEM (IBFEM), uses solution structures constructed using implicit equations of the boundaries to enforce boundary and interface conditions. This method has been applied to 2D and 3D elastostatics and steady state heat transfer problems [42]-[45]. Structured mesh, which has uniform, undistorted elements, can be used for the analysis because the implicit boundary method does not require nodes on the boundary to impose boundary conditions. Structured mesh, such as the examples shown in Fig. 25 is easy to generate since all elements are regular shaped and the grid does not have to conform to the geometry.



(a) 2D structured mesh



(b) 3D structured mesh

**Fig. 25      Structure mesh for multi-material systems**

For modeling multiple materials and assemblies, a separate grid is generated for each material or part as shown in Fig. 25 . Within overlapping elements at the interface, the piece-wise interpolation within each grid is combined into a single solution structure.

## 2. Governing equation and Weak form for 2D Magnetostatics

Under static and quasi-static conditions, the governing equation for 2D magnetostatics is

$$\frac{\partial}{\partial x_1} \left( \frac{1}{\mu} \frac{\partial A}{\partial x_1} \right) + \frac{\partial}{\partial x_2} \left( \frac{1}{\mu} \frac{\partial A}{\partial x_2} \right) = -J \quad (4.1)$$

where,  $\mu$  is the magnetic permeability,  $A$  is the component of magnetic vector potential in the  $x_3$ -direction (the direction normal to the plane of analysis) and  $J$  is the current density in the  $x_3$ -direction. In the finite element method, essential boundary conditions are specified by assigning values for the nodes along the boundary. When a structured grid is used for the analysis, there may not be any nodes available on the boundary. Solution structures that use the equation of the boundary to impose essential boundary condition have been used by several authors [46]-[48]. For 2D magnetostatics, a similar solution structure for the  $x_3$  component of magnetic vector potential could be defined as

$$A(\mathbf{x}) = D(\mathbf{x})A^g(\mathbf{x}) + A^a(\mathbf{x}) = A^s(\mathbf{x}) + A^a(\mathbf{x}) \quad (4.2)$$

where,  $A^s$  is a grid variable that is defined by piece-wise interpolation or using B-spline approximation [44] over a structured grid.  $A^a$  is the boundary value function which has a value equal to the prescribed boundary conditions at the boundaries.  $D(\mathbf{x})$  is a weighting function defined such that  $D(\mathbf{x})=0$  at boundaries where essential boundary conditions are applied so that  $A=A^a$  at these boundaries. The boundary value function,  $A^a$ , is constructed by interpolating nodal values within elements. The nodal values are selected such that at the boundary it has a value equal to the specified boundary condition. Note that  $D(\mathbf{x})=0$  can be any type of implicit equation of the boundary but in general it is hard to construct a global function that is zero only at the boundaries with essential boundary conditions. Furthermore, a global weighting function can lead to poor convergence especially if it is nonlinear. In the implicit boundary method, approximate step functions referred to as Dirichlet functions or D-functions [43]-[44] are used as the weighting function. At any given point  $\mathbf{x} \in \mathbf{R}^3$ , the D-function is defined as

$$D(\mathbf{x}) = \begin{cases} 0 & \phi(\mathbf{x}) \leq 0 \\ 1 - (1 - \phi(\mathbf{x})/\delta)^2 & 0 \leq \phi(\mathbf{x}) \leq \delta \\ 1 & \phi(\mathbf{x}) \geq \delta \end{cases} \quad (4.3)$$

where,  $\phi(\mathbf{x})=0$  is the signed distance function or the distance from the boundary with a negative value if the point  $\mathbf{x}$  is outside the domain.  $\delta$  is a parameter which controls the width of the *transition band* over which the D-function transitions from 0 to 1. In the limit as  $\delta \rightarrow 0$  the D-function approximates the Heaviside step function. The advantage of using an approximate step function as weighting function is that it

transitions from 0 to 1 within boundary elements. Therefore, they can be locally defined within the required boundary elements and for all other elements  $D(\mathbf{x})=1$ . This implies that the internal elements are not influenced by the weighting function and are therefore identical to traditional finite elements. Moreover, all the internal elements are identical to each other and have the same stiffness matrix since they have the same shape and size. The value of  $\delta$  is chosen to be less than one-tenth of the element length in our numerical implementation so that the D-function closely approximates the Heaviside step function. Using the solution structure defined in (2), the weak form of the 2D magnetostatic equation can be derived as

$$\begin{aligned} \int_V \nabla(\delta A^s) \mu^{-1} \nabla(A^s) dV = \\ \int_V (\delta A^s) J dV + \int_V (\delta A^s) H_t \delta dS - \int_V \nabla(\delta A^s) \mu^{-1} \nabla(A^a) dV \end{aligned} \quad (4.4)$$

where,  $\delta A^s$  is the virtual magnetic potential vector and  $H_t$  is the tangential component of the magnetic field.

The grid variable,  $A^s$ , is interpolated within each element as  $A^s = \{\mathbf{N}\}^T \{\mathbf{A}^s\}$  where,  $\{\mathbf{N}\}^T$  is a row matrix containing the shape functions and  $\{\mathbf{A}^s\}$  is a column matrix containing the nodal values of the grid variable. Similarly, the boundary value function is represented within each element as  $A^a = \{\mathbf{N}\}^T \{\mathbf{A}^a\}$  where,  $\{\mathbf{A}^a\}$  is column matrix containing the nodal values assigned such that  $A^a$  has the prescribed value at the boundary. Note that the same shape functions are used to interpolate  $A^s$  and  $A^a$ . If all the essential boundary conditions are homogeneous, so that  $A=0$  is the only prescribed boundary condition, then the boundary value function  $A^a$  is zero everywhere and can be eliminated from the solution structure. Otherwise, nodes near the boundary are assigned values of  $A^a$  equal to the prescribed value. For 2D problems, the gradients of the boundary value function  $A^a$  is expressed as

$$\nabla A^a = \left\{ \frac{\partial A^a}{\partial x_1} \quad \frac{\partial A^a}{\partial x_2} \right\}^T = \sum_i \frac{\partial N_i}{\partial x_j} A_i^a = [\mathbf{B}] \{\mathbf{A}^a\} \quad (4.5)$$

The gradients of the homogenous part of the solution  $A^s$  is stated as

$$\begin{aligned} \nabla A^s &= \left\{ \frac{\partial A^s}{\partial x_1} \quad \frac{\partial A^s}{\partial x_2} \right\}^T \\ &= \sum_i \left( D \frac{\partial N_i}{\partial x_j} + N_i \frac{\partial D}{\partial x_j} \right) A_i^s = [\bar{\mathbf{B}}] \{\mathbf{A}^s\} \end{aligned} \quad (4.6)$$

$[\bar{\mathbf{B}}]$  is decomposed into two matrices  $[\bar{\mathbf{B}}_1]$  and  $[\bar{\mathbf{B}}_2]$  such that only  $[\bar{\mathbf{B}}_2]$  contains derivatives of the D-function which can have very large values near the boundary.

$$[\bar{\mathbf{B}}_1] = \bar{B}_{ij}^1 = D \frac{\partial N_i}{\partial x_j} \quad \text{and} \quad (4.7)$$

$$[\bar{\mathbf{B}}_2] = \bar{B}_{ij}^2 = N_i \frac{\partial D}{\partial x_j} . \quad (4.8)$$

The element matrix to be assembled into the global equations can be defined as

$$[\mathbf{K}^e] = \int_{\Omega_e} [\bar{\mathbf{B}}]^T \mu^{-1} [\bar{\mathbf{B}}] d\Omega_e = [\mathbf{K}_1^e] + [\mathbf{K}_2^e] + [\mathbf{K}_3^e] \quad (4.9)$$

$$[\mathbf{K}_1^e] = \int_{\Omega_e} [\bar{\mathbf{B}}_1]^T \mu^{-1} [\bar{\mathbf{B}}_1] d\Omega_e \quad (4.10)$$

$$[\mathbf{K}_2^e] = \int_{\Omega_e} [\bar{\mathbf{B}}_2]^T \mu^{-1} [\bar{\mathbf{B}}_2] d\Omega_e \quad (4.11)$$

$$[\mathbf{K}_3^e] = \int_{\Omega_e} \left( [\bar{\mathbf{B}}_1]^T \mu^{-1} [\bar{\mathbf{B}}_2] + [\bar{\mathbf{B}}_2]^T \mu^{-1} [\bar{\mathbf{B}}_1] \right) d\Omega_e \quad (4.12)$$

$[\bar{\mathbf{B}}_2]$  which contains the derivatives of D-function, is non-zero only within the narrow transition band near the boundary. Therefore, for all internal elements and boundary elements without essential boundary conditions  $[\mathbf{K}_2^e]$  and  $[\mathbf{K}_3^e]$  are zero. For boundary elements  $[\mathbf{K}_1^e]$  is evaluated by subdividing these elements into triangles and integrating only within triangles that are inside the geometry. For boundary elements with boundary conditions, the volume integral for computing  $[\mathbf{K}_2^e]$  and  $[\mathbf{K}_3^e]$  can be converted to surface integrals because they contain  $[\bar{\mathbf{B}}_2]$  which is non-zero only within the narrow transition band near the boundary. The components of  $[\mathbf{K}_2^e]$  can be expressed using index notation as

$$K_{2ij}^e = \int_{\Gamma_e} N_i \mu^{-1} N_j \Delta d\Gamma_e \quad (4.13)$$

where,

$$\Delta = \left( \int_0^\delta \sum_k \left( \frac{\partial D}{\partial x_k} \right)^2 \frac{1}{|\nabla \phi|} d\phi \right) \quad (4.14)$$

In the preceding equation, the volume integral in (11) has been converted into a combination of surface integral along the boundary and an integration over  $\phi$ . Similarly, the components of  $[\mathbf{K}_3^e]$  can be stated as

$$K_{3ij}^e = \int_{\Gamma_e} \sum_k \left( \frac{\partial N_i}{\partial x_k} \mu^{-1} N_j + \frac{\partial N_j}{\partial x_k} \mu^{-1} N_i \right) \Delta_k d\Gamma_e \quad (4.15)$$

where,

$$\Delta_k = \left( \int_0^\delta D \frac{\partial D}{\partial x_k} \frac{1}{|\nabla \phi|} d\phi \right) \quad (4.16)$$

All components of  $[\mathbf{K}_1^e]$ ,  $[\mathbf{K}_2^e]$ , and  $[\mathbf{K}_3^e]$  are evaluated using Gaussian quadrature. For surface integrals, the boundary within element is approximated by sufficiently small straight line segments to achieve accuracy.

### 3. Governing equation and Weak form for 3D magnetostatics

Several alternate formulations have been proposed in literature for 3D magnetostatic analysis using finite element method [49]-[57]. A formulation based on magnetic vector potential,  $\mathbf{A}$ , was used in our implementation. The governing equations for 3D magnetostatics expressed in terms of magnetic vector potential is

$$\nabla \times (\nu \nabla \times \mathbf{A}) = \mathbf{J} \quad \text{in } \Omega \quad (4.17)$$

where,  $\Omega$  is the domain of analysis. The boundary of the analysis domain  $\Gamma$  consists of regions with specified natural boundary conditions and regions that are open boundaries, which are used to artificially truncate the analysis domain when in reality it extends to infinity. Often homogeneous essential boundary conditions are used on these open boundaries as an approximation if the boundary is far away from the sources. Several special techniques for modeling such open boundaries have been developed such as the infinite elements and asymptotic boundary condition [58]. Natural boundary conditions can be applied on boundaries (denoted as  $\Gamma_H$ ) with known tangential component of the magnetic field or on boundaries (denoted as  $\Gamma_B$ ) with known normal component of the flux density. If these boundaries are planes of symmetry then  $\mathbf{n} \cdot (\nabla \times \mathbf{A}) = 0$  on  $\Gamma_B$  and  $\mathbf{n} \times (\nu \nabla \times \mathbf{A}) = 0$  on  $\Gamma_H$ . To ensure uniqueness of the solution, the following essential boundary conditions are used to enforce these conditions [51].

$$\mathbf{n} \times \mathbf{A} = 0 \quad \text{on } \Gamma_B \quad (4.18)$$



$$\mathbf{n} \cdot \mathbf{A} = 0 \quad \text{on } \Gamma_H \quad (4.19)$$

Fig. 26 shows an example domain of analysis which may contain regions of different materials ( $\Omega_1$  and  $\Omega_2$ ) as shown.  $\Gamma_{12}$  is the interface surface between the two sub-domains  $\Omega_1$  and  $\Omega_2$  as shown in Fig. 26. At the interface, the tangential component of the magnetic field and the normal component of the flux density are continuous.

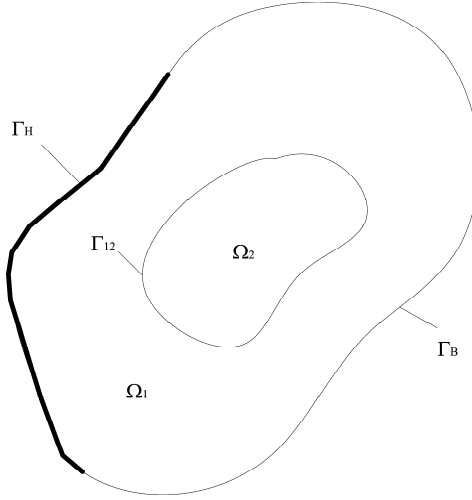


**Fig. 26 Analysis domain and boundaries**

The weak form for these governing equations and boundary conditions, obtained using the weighted residual method [59], is

$$\int_{\Omega} (\nabla \times \delta \mathbf{A}) \cdot (\nu \nabla \times \mathbf{A}) d\Omega = \int_{\Gamma_H + \Gamma_B} \delta \mathbf{A} (\mathbf{H} \times \mathbf{n}) d\Gamma + \int_{\Omega} \mathbf{J} \delta \mathbf{A} d\Omega \quad (4.20)$$

where,  $\delta \mathbf{A}$  is the vector weighting functions. This weak form is used in the traditional FEM to compute the element matrices by integrating the left hand side over the volume of each element. When a structured mesh is used for the analysis, the boundaries pass through the elements so that it is necessary to integrate over partial volume of the element that is inside the boundary. Several techniques [60]-[61] have been developed for integrating over partial elements approximated as polygons. Alternatively, the partial boundary elements can be subdivided into triangles (for 2D) or tetrahedrons (for 3D) for integration purpose. The generated triangles or tetrahedrons are used only for quadrature and not to represent the solution. Even though the tessellation of the boundary elements for integration approximates the boundary, the size of the triangles/ tetrahedrons can be much smaller than the elements of the grid. So the geometry can be represented reasonably accurately even if a sparse mesh is used for the analysis. Essential boundary conditions are applied in traditional

FEM by assigning values to the nodes on the boundary. However, when a structured mesh is used there may not be nodes available on the boundary. In the next section, a solution structure is described that is constructed using the implicit equation of the boundary to enforce essential boundary conditions.

Several structured mesh based approaches for analysis have used solution structures [42]-[48] constructed using implicit equations of boundary, to impose essential boundary conditions. Here we present the implicit boundary method, where step functions are used as implicit equations to construct solution structures. For three-dimensional magnetostatics, a solution structure for the magnetic vector potential  $\mathbf{A}(\mathbf{x})$  could be defined as

$$\mathbf{A}(\mathbf{x}) = [\mathbf{D}(\mathbf{x})] \mathbf{A}^g(\mathbf{x}) + \mathbf{A}^a(\mathbf{x}) = \mathbf{A}^s(\mathbf{x}) + \mathbf{A}^a(\mathbf{x}) \quad (4.21)$$

In the preceding equation,  $\mathbf{A}^g$  is a grid variable vector that is defined by piecewise interpolation or using B-spline approximation [44] over a structured mesh and  $\mathbf{D}(\mathbf{x})$  is diagonal matrix whose components are defined such that  $D_{ii}(\mathbf{x}) = 0$  at the boundaries where essential boundary conditions are applied on the  $i$ th component of  $\mathbf{A}$ . This ensures that  $A_i = A_i^a$  at the boundary.  $\mathbf{A}^s$  is the homogenous part of the solution and  $\mathbf{A}^a$  is the boundary value function. The boundary value function is defined such that it has value equal to the prescribed boundary conditions at the boundaries. Therefore, diagonal components of the  $\mathbf{D}$  matrix,  $D_{ii}(\mathbf{x})$ , are implicit equations of the boundaries on which essential boundary conditions are applied. It is hard to construct such a function that is zero only at the boundaries with essential boundary conditions. Moreover, if this weighting function is nonlinear and defined globally, then this solution structure can lead to poor convergence. In the implicit boundary finite element method, approximate step functions are used as the implicit equation. At any given point  $\mathbf{x} \in \mathbf{R}^3$  this step function, referred to as the D-function, is defined as

$$D_{ii}(\mathbf{x}) = \begin{cases} 0 & \phi_i(\mathbf{x}) \leq 0 \\ 1 - (1 - \phi(\mathbf{x})/\delta)^2 & 0 \leq \phi(\mathbf{x}) \leq \delta \\ 1 & \phi(\mathbf{x}) \geq \delta \end{cases} \quad (4.22)$$

where,  $\phi(\mathbf{x})$  is the signed distance function for the boundary. The signed distance function for a boundary is evaluated at any point  $\mathbf{x}$  as the distance of the point from the boundary. The function has a negative value if the point is outside the domain. The step function  $D_{ii}(\mathbf{x})$  transitions from 0 to 1 over a band whose width is controlled by the parameter  $\delta$ . In the limit as  $\delta \rightarrow 0$  the D-function approximates the Heaviside step

function. In our numerical implementation, the value of the parameter  $\delta$  is chosen to be less than one-tenth of the element length. The advantage of using an approximate step function as weighting function is that it transitions from 0 to 1 within boundary elements. Therefore, they can be locally defined within these elements. For all other elements, which do not have a boundary with prescribed essential boundary conditions, we can set  $D_{ii}(\mathbf{x}) = 1$ . This implies that the internal elements are not influenced by the weighting function and since the structured mesh is made of uniform elements that are identical to each other, all the internal elements have the same stiffness matrix. Substituting the solution structure (5) into the weak form (4), a modified weak form of the 3D magnetostatic equation can be derived as

$$\int_{\Omega} (\nabla \times \delta \mathbf{A}^s) \cdot (\nu \nabla \times \mathbf{A}^s) d\Omega = \int_{\Omega} \mathbf{J} \delta \mathbf{A}^s d\Omega - \int_{\Omega} (\nabla \times \delta \mathbf{A}^s) \cdot (\nu \nabla \times \mathbf{A}^a) d\Omega \quad (4.23)$$

where,  $\delta \mathbf{A}^s$  is the virtual magnetic potential vector.

The grid variable vector,  $\mathbf{A}^s$ , is interpolated within each element as  $\mathbf{A}^s = [\mathbf{N}]^T \{\mathbf{A}^s\}$  where,  $[\mathbf{N}]^T$  is a matrix containing the shape functions and  $\{\mathbf{A}^s\}$  is a column matrix containing the nodal values of the grid variable vector. For brick elements with 8 nodes, the size of  $\{\mathbf{A}^s\}$  is 24 because the nodal degree of freedom is 3. Similarly, the boundary value function,  $\mathbf{A}^a$ , is defined by interpolating nodal values within each element as  $\mathbf{A}^a = [\mathbf{N}]^T \{\mathbf{A}^a\}$  where,  $\{\mathbf{A}^a\}$  is column matrix containing the nodal values of  $\mathbf{A}^a$ . These nodal values are assigned such that, at the boundaries, this function will have a values prescribed by the boundary condition. Using the solution structure, the magnetic flux for the boundary value function can be derived as

$$\nabla \times \mathbf{A}^a = [\mathbf{B}^c] \{\mathbf{A}^a\} \quad (4.24)$$

The 'curl' matrix  $[\mathbf{B}^c]$  for the boundary value function is defined as  $[\mathbf{B}^c] = [[\mathbf{B}_1^c] \quad [\mathbf{B}_2^c] \quad \dots \quad [\mathbf{B}_n^c]]$ , where,

$$[\mathbf{B}_i^c] = \begin{bmatrix} 0 & -\frac{\partial N_i}{\partial z} & \frac{\partial N_i}{\partial y} \\ \frac{\partial N_i}{\partial z} & 0 & -\frac{\partial N_i}{\partial x} \\ -\frac{\partial N_i}{\partial y} & \frac{\partial N_i}{\partial x} & 0 \end{bmatrix} \quad (4.25)$$

for  $i \in Z = [1, N]$ . The curl of  $\mathbf{A}^s$  can be computed as

$$\nabla \times \mathbf{A}^s = [\bar{\mathbf{B}}^C] \{ \mathbf{A}^g \} \quad (4.26)$$

For convenience,  $[\bar{\mathbf{B}}^C]$  is defined as a sum of two matrices such that the first one only contains derivatives of the shape function and the second matrix contains the derivatives of the D-function.  $[\bar{\mathbf{B}}^C] = [\bar{\mathbf{B}}_1^C] + [\bar{\mathbf{B}}_2^C]$ , where

$$\begin{aligned} [\bar{\mathbf{B}}_1^C] &= \begin{bmatrix} [\bar{\mathbf{B}}_{11}^C] & [\bar{\mathbf{B}}_{12}^C] & \dots & [\bar{\mathbf{B}}_{1n}^C] \end{bmatrix} \\ [\bar{\mathbf{B}}_2^C] &= \begin{bmatrix} [\bar{\mathbf{B}}_{21}^C] & [\bar{\mathbf{B}}_{22}^C] & \dots & [\bar{\mathbf{B}}_{2n}^C] \end{bmatrix} \end{aligned} \quad (4.27)$$

$$[\bar{\mathbf{B}}_{1i}^C] = \begin{bmatrix} 0 & -D_{22} \frac{\partial N_i}{\partial x_3} & D_{33} \frac{\partial N_i}{\partial x_2} \\ D_{11} \frac{\partial N_i}{\partial x_3} & 0 & -D_{33} \frac{\partial N_i}{\partial x_1} \\ -D_{11} \frac{\partial N_i}{\partial x_2} & D_{22} \frac{\partial N_i}{\partial x_1} & 0 \end{bmatrix} \quad (4.28)$$

$$[\bar{\mathbf{B}}_{2i}^C] = \begin{bmatrix} 0 & -N_i \frac{\partial D_{22}}{\partial x_3} & N_i \frac{\partial D_{33}}{\partial x_2} \\ N_i \frac{\partial D_{11}}{\partial x_3} & 0 & -N_i \frac{\partial D_{33}}{\partial x_1} \\ -N_i \frac{\partial D_{11}}{\partial x_2} & N_i \frac{\partial D_{22}}{\partial x_1} & 0 \end{bmatrix} \quad (4.29)$$

In the preceding equations,  $i = 1, 2, \dots, n$ , where,  $n$  is the number of nodes per element. The element matrix that is assembled into the global equations can be defined as

$$[\mathbf{K}^e] = \int_{\Omega_e} \left\{ [\bar{\mathbf{B}}^C]^T \nu [\bar{\mathbf{B}}^C] \right\} d\Omega_e = [\mathbf{K}_1^e] + [\mathbf{K}_2^e] + [\mathbf{K}_3^e] \quad (4.30)$$

$$[\mathbf{K}_1^e] = \int_{\Omega_e} \left\{ [\bar{\mathbf{B}}_1^C]^T \nu [\bar{\mathbf{B}}_1^C] \right\} d\Omega_e \quad (4.31)$$

$$[\mathbf{K}_2^e] = \int_{\Omega_e} \left\{ [\bar{\mathbf{B}}_2^C]^T \nu [\bar{\mathbf{B}}_2^C] \right\} d\Omega_e \quad (4.32)$$

$$[\mathbf{K}_3^e] = \int_{\Omega_e} \left( \left\{ [\bar{\mathbf{B}}_1^C]^T \nu [\bar{\mathbf{B}}_2^C] \right\} + \left\{ [\bar{\mathbf{B}}_2^C]^T \nu [\bar{\mathbf{B}}_1^C] \right\} \right) d\Omega_e \quad (4.33)$$

Since  $[\bar{\mathbf{B}}_2^c]$  contains the derivatives of  $D_{ii}(\mathbf{x})$ , it is non-zero only within the narrow transition band near the boundary. Therefore, for all internal elements and boundary elements without essential boundary conditions  $[\mathbf{K}_2^e]$  and  $[\mathbf{K}_3^e]$  are zero. Within the transition band, the derivatives of  $D(\mathbf{x})$  can have large magnitude. For the boundary elements with boundary conditions, the volume integral for computing  $[\mathbf{K}_2^e]$  and  $[\mathbf{K}_3^e]$  must be converted to surface integrals as follows to compute them accurately.

$$[\mathbf{K}_2^e] = \int_{\Gamma_e} \left\{ \int_0^\delta \left( [\bar{\mathbf{B}}_2^c]^T \nu [\bar{\mathbf{B}}_2^c] \right) \frac{1}{|\nabla \phi|} d\phi \right\} d\Gamma_e \quad (4.34)$$

$$[\mathbf{K}_3^e] = \int_{\Gamma_e} \left\{ \int_0^\delta \left( [\bar{\mathbf{B}}_1^c]^T \nu [\bar{\mathbf{B}}_2^c] + [\bar{\mathbf{B}}_2^c]^T \nu [\bar{\mathbf{B}}_1^c] \right) \frac{1}{|\nabla \phi|} d\phi \right\} d\Gamma_e \quad (4.35)$$

To derive the preceding equations, we make use of the fact that  $[\bar{\mathbf{B}}_2^c]$  is zero except in the narrow band  $0 \leq \phi \leq \delta$ . Therefore, the volume integral is converted into a surface integral along the boundary  $\Gamma_e$  and an integral over the transition band (normal to the surface). Note that if  $\phi$  is a signed distance function then  $|\nabla \phi| = 1$ . If the width of the band  $\delta$  is very small, then one can assume that the shape functions are constant within the band, allowing the integral over  $\phi$  to be determined analytically. Alternatively, the integration over  $\phi$  can also be evaluated numerically.

#### 4. Solution structure for multi-material models

At the interface between materials with different magnetic permeability, the normal component of magnetic field and the tangential component of flux density can be discontinuous. The tangential component of the magnetic field and normal component of the flux density are continuous. The required interface conditions, expressed in terms of the magnetic vector potential are

$$\mathbf{n} \times (\nu_1 \nabla \times \mathbf{A}_1) = \mathbf{n} \times (\nu_2 \nabla \times \mathbf{A}_2) \quad (4.36)$$

$$\mathbf{n} \cdot (\nabla \times \mathbf{A}_1) = \mathbf{n} \cdot (\nabla \times \mathbf{A}_2) \quad (4.37)$$

It is obvious that if the magnetic vector potential is continuous, that is  $\mathbf{A}_1 = \mathbf{A}_2$ , then the second condition (21) is automatically satisfied. The requirement for continuity of the tangential component of the magnetic field (20) requires that the derivatives of the vector potential should be discontinuous. To allow this discontinuity in the magnetic field, separate grids are used for each material as shown in Fig. 25. At the interface, the elements from neighboring grids overlap. A solution structure is needed

for overlapping elements, which ensures that the vector potential,  $A$ , is continuous while flux density  $B$  and magnetic field  $H$  can be discontinuous. The following solution structure was used for interface elements

$$\mathbf{A}^g = (1 - D(\mathbf{x}))\mathbf{A}^{g1} + D(\mathbf{x})\mathbf{A}^{g2} \quad (4.38)$$

where,  $\mathbf{A}^{gi}$  is the field interpolated or approximated within the element from grid  $i$ , ( $i = 1, 2$ ),  $D(\phi_1(\mathbf{x}))$  is the approximate step function defined in (6) and  $\phi_1(\mathbf{x})$  is the implicit equation of the interface curve (represented using signed distance function). Similar solution structure has been used to model material discontinuity for elasticity problems [45]. The solution structure in (22) blends the solutions from the two grids such that the vector potential is continuous at the interface. Note that this method for blending the solutions uses a partition of unity as weighting functions. This solution structure ensures the continuity of the solution throughout the analysis domain. It also allows the derivatives (and magnetic field and flux density) to be discontinuous at the interface. The gradient of the vector potential components are

$$\frac{\partial A_i}{\partial x_j} = \left( (1 - D) \frac{\partial A_i^{g1}}{\partial x_j} - \frac{\partial D}{\partial x_j} A_i^{g1} + D \frac{\partial A_i^{g2}}{\partial x_j} + \frac{\partial D}{\partial x_j} A_i^{g2} \right) \quad (4.39)$$

For small values of  $\delta$ , the gradient of  $D(\mathbf{x})$  can have large magnitude which in turn acts as a penalty that tries to enforces  $\mathbf{A}^{g1} = \mathbf{A}^{g2}$  at the interface so that the second and third terms cancel each other. Therefore, the grid variable is approximately continuous while the vector potential is exactly continuous. The slope of the grid variable and therefore the vector potential can be continuous or discontinuous as dictated by the equilibrium equations.

Substituting (22) into the weak form, the element matrices for the interface elements can be computed. Again, since gradient of  $D(\mathbf{x})$  is very large near the interface, it helps to decompose the matrices into terms that only contain derivatives of the shape functions and those that contain derivative of  $D(\mathbf{x})$ . As illustrated in the previous section, all the terms that involve derivatives of  $D(\mathbf{x})$  can be converted from volume integrals into surface integrals for accurate numerical evaluation. These techniques are described in detail in [45] for elastostatics and have been adopted here for magnetostatics.

## 5. Magnetic force computation

Several techniques for computing magnetic forces can be found in literature [62]. These include the Maxwell's stress tensor, equivalent source method and the virtual work principle [63]-[66] to list a few. These approaches have been implemented using

FEM and therefore can also be used with the implicit boundary FEM. Since we assume that the exact equation of the surface is available (preferably as a parametric equation), it is easier to implement a method that integrates surface force densities to compute the nodal forces. The basic equation for magnetic force density [67] can be derived from energy balance equations and is given by

$$\mathbf{f}_m = -\frac{1}{2} H^2 \nabla \mu + \mathbf{J} \times \mathbf{B} \quad (4.40)$$

The first term in (19) involves the gradient of magnetic permeability. Therefore, this term is of significance only at the boundary between ferromagnetic materials and surrounding non-ferromagnetic materials. The second term is a body force that exists on current carrying conductors in the presence of magnetic flux density. To compute the structural response due to these magnetic forces, a subsequent solid mechanics analysis is necessary. The weak form for solid mechanics problems is the principle of virtual work which can be stated as follows:

$$\int_V \{\delta \boldsymbol{\varepsilon}\}^T [\mathbf{C}] \{\boldsymbol{\varepsilon}\} dV = \int_V \mathbf{f}_m \cdot \delta \mathbf{u} dV + \int_S \mathbf{t} \cdot \delta \mathbf{u} dS \quad (4.41)$$

The first term on the right hand side of the weak form is the virtual work done by magnetic forces. This term can be evaluated as follows:

$$\int_V \mathbf{f}_m \cdot \delta \mathbf{u} dV = -\int_V \frac{1}{2} H^2 \nabla \mu \delta \mathbf{u} dV + \int_V (\mathbf{J} \times \mathbf{B}) \cdot \delta \mathbf{u} dV \quad (4.42)$$

If we assume that the permeability is constant within the materials then the first term in (21) makes a contribution only at the boundary. For a ferromagnetic object with permeability,  $\mu_1$ , surrounded by a medium whose permeability is  $\mu_2$ , the permeability can be considered to change from one value to the other over a band along the boundary whose width, measured in the normal direction, is  $\Delta n$ . The limit of  $\Delta n \rightarrow 0$  represents the discontinuous variation at the boundary. The gradient of the permeability within this band can then be written as:

$$\nabla \mu = \frac{\partial \mu}{\partial n} \hat{\mathbf{n}} \quad (4.43)$$

The unit vector  $\hat{\mathbf{n}}$  is the direction normal to the boundary between the two materials with different permeability and points in direction of increasing permeability. Using this expression in the first term of (21), we get,

$$\begin{aligned}
-\int_V \frac{1}{2} H^2 \nabla \mu \delta \mathbf{u} dV &= -\frac{1}{2} \int_{S_F} \left[ \int_0^{\Delta n} H^2 \left( \frac{\partial \mu}{\partial n} \hat{\mathbf{n}} \cdot \delta \mathbf{u} \right) dn \right] dS \\
&= -\frac{1}{2} \int_{S_F} \left[ \int_{\mu_2}^{\mu_1} H^2 (\hat{\mathbf{n}} \cdot \delta \mathbf{u}) d\mu \right] dS
\end{aligned} \tag{4.44}$$

Therefore the volume integral can be converted to a surface integral where,  $S_F$  is the surface separating two materials with different permeability. The virtual work due to magnetic body forces can now be evaluated as

$$\int_V \mathbf{f}_m \cdot \delta \mathbf{u} dV = \int_{S_F} \mathbf{f}_s \cdot \delta \mathbf{u} dV + \int_V \mathbf{f}_b \cdot \delta \mathbf{u} dV \tag{4.45}$$

where,  $\mathbf{f}_b = \mathbf{J} \times \mathbf{B}$  is body force and  $\mathbf{f}_s = -\frac{1}{2} \int_{\mu_2}^{\mu_1} H^2 \hat{\mathbf{n}} d\mu$  is a surface force density (or traction). The surface force density term can be evaluated by expressing the square of magnetic field as a function of permeability. If there is no surface current then the tangential component of the magnetic field does not vary across the boundary and can be treated as a constant. Similarly, the normal component of the magnetic flux density is constant (by Gauss's law) and does not vary across the boundary even though the permeability is different on the two sides of the boundary. The square of the magnetic field can be expressed as the sum of the squares of the tangential and normal components of the field as:

$$H^2 = H_t^2 + H_n^2 = H_t^2 + \frac{B_n^2}{\mu^2} \tag{4.46}$$

Both the tangential component of magnetic field ( $H_t$ ) and the normal component of the magnetic flux density ( $B_n$ ) can be treated as constants for the integration in computing surface traction since these quantities do not vary in the direction normal to the interface between the two materials. Using the preceding equation for the square of magnetic field to compute the surface traction due to magnetic forces we get

$$\begin{aligned}
\mathbf{f}_s &= -\frac{1}{2} \int_{\mu_2}^{\mu_1} \left( H_t^2 + \frac{B_n^2}{\mu^2} \right) \hat{\mathbf{n}} d\mu \\
&= \left[ -\frac{1}{2} H_t^2 (\mu_1 - \mu_2) + \frac{1}{2} \left( \frac{B_n^2}{\mu_1} - \frac{B_n^2}{\mu_2} \right) \right] \hat{\mathbf{n}} \\
&= \left[ \frac{1}{2} \left( \frac{B_{1t}^2}{\mu_1} - \frac{B_n^2}{\mu_1} \right) \hat{\mathbf{n}}_1 + \frac{1}{2} \left( \frac{B_{2t}^2}{\mu_2} - \frac{B_n^2}{\mu_2} \right) \hat{\mathbf{n}}_2 \right]
\end{aligned} \tag{4.47}$$



where,  $\mu_i$  and  $\hat{\mathbf{n}}_i$  are the permeability and the outward normal vector of the  $i^{\text{th}}$  material and  $B_{it}$  is the tangential component of the magnetic flux density within the  $i^{\text{th}}$  material. If  $\mu_2 < \mu_1$  it follows that  $f_s < 0$  therefore the direction of the surface traction  $\mathbf{f}_s$  is opposite to  $\hat{\mathbf{n}}$ , which means that it acts in the direction of decreasing permeability. In [66] an expression for the surface force densities, similar to (26), between two linear media has been deduced from a more general expression for magnetic force.

At the interface elements, magnetic forces can be computed by integrating the magnetic force density over the interface boundary. The nodal forces at the boundary elements of each grid can be computed by integrating over the piece of the boundary that passes through the element. In other words, for a boundary element whose material property is  $\mu_i$  the nodal forces are computed as:

$$\{\mathbf{F}_s\} = \int_{S_e} [\mathbf{N}]^T \frac{1}{2} \left( \frac{B_{it}^2}{\mu_i} - \frac{B_n^2}{\mu_i} \right) \hat{\mathbf{n}}_i dS \quad (4.48)$$

The unit normal  $\hat{\mathbf{n}}_i = n_{i1}\hat{\mathbf{i}} + n_{i2}\hat{\mathbf{j}}$  is constructed such that it points outwards from the material or part boundary. The tangential and normal components of the flux density are computed from the vector potential as

$$\begin{aligned} B_{it} &= \frac{\partial A}{\partial x_2} n_{i1} + \frac{\partial A}{\partial x_1} n_{i2} \\ B_n &= \frac{\partial A}{\partial x_2} n_{i1} - \frac{\partial A}{\partial x_1} n_{i2} \end{aligned} \quad (4.49)$$

In traditional FEM the integration over the interface boundary requires finding the elements at the interface and determining which edge or face lies along the interface. In the implicit boundary approach, since the equations of the interface are available for each part/material, it is very easy to integrate (27) over these boundaries to evaluate the nodal forces for each part separately. The boundary passing through each element is approximated by straight lines or triangles for the purpose of integration and Gauss Quadrature is used to perform the integration.

## 6. Results and discussion

Several examples are presented here that were used to validate the implicit boundary method. Some of these examples have analytical solutions with which to compare the computed results. This allows us to not only verify the accuracy of the results but also study the rate of convergence and compare with similar results using the traditional finite element method. Some examples are modeled using 2D and 3D elements for comparison and validation.

## Coaxial cable

A coaxial cable, which consists of an inner conductor, an insulator, and an outer conductor, is modeled as shown in Fig. 27 using three separate structured grids. Due to circular symmetry of the geometry, only a quadrant of the coaxial cable cross-section is created. The radii of the inner conductor, the insulator and the outer conductor are  $a$ ,  $b$  and  $c$ . The inner and outer conductors carry the same amount of total current in opposite directions. The total current flowing through each conductor is  $I$ . The current flows in the axial direction (z-direction) and the current density is assumed to be uniform.

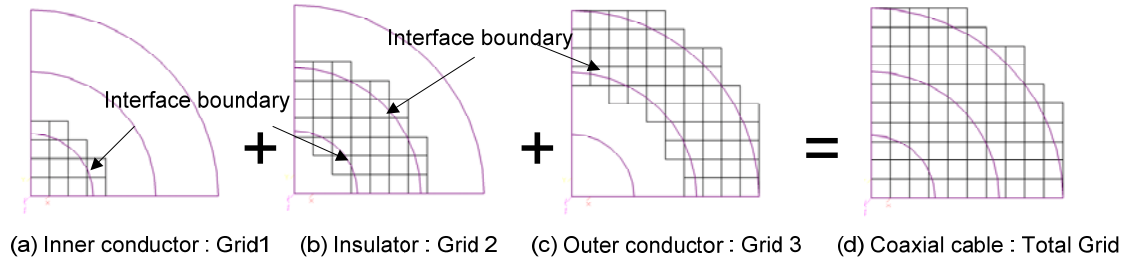


**Fig. 27      Structured mesh**

The analytical solution of the magnetic field in circumferential direction can be derived as

$$H_{\theta} = \begin{cases} r(2\pi a^2)^{-1} I & , 0 \leq r < a \\ (2\pi r)^{-1} I & , a \leq r < b \\ (c^2 - r^2)(c^2 - b^2)^{-1} (2\pi r)^{-1} I & , b \leq r < c \\ 0 & , c \leq r \end{cases} \quad (4.50)$$

where,  $r$  is the radial distance. The following values of current and radii were used in the numerical model:  $I = 1000A$ ,  $a = 0.5$ ,  $b = 1$ , and  $c = 1.5$  mm.

Fig. 28 shows the magnitude of the magnetic field that was computed using the quadratic B-spline elements. It shows that the maximum magnetic field value is at the interface between the inner conductor and the insulator and has a value of  $3.182 \times 10^2$  A/mm. This is very close to the value obtained from the analytical solution which is  $3.183 \times 10^2$  A/mm.

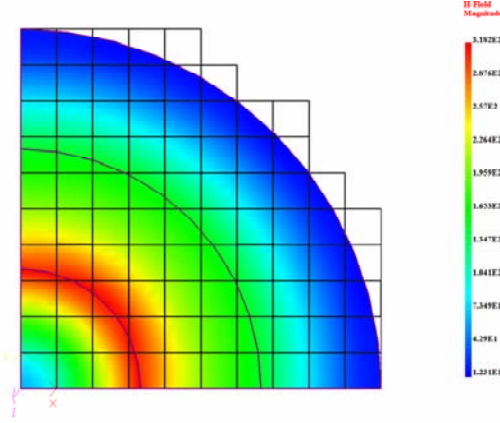
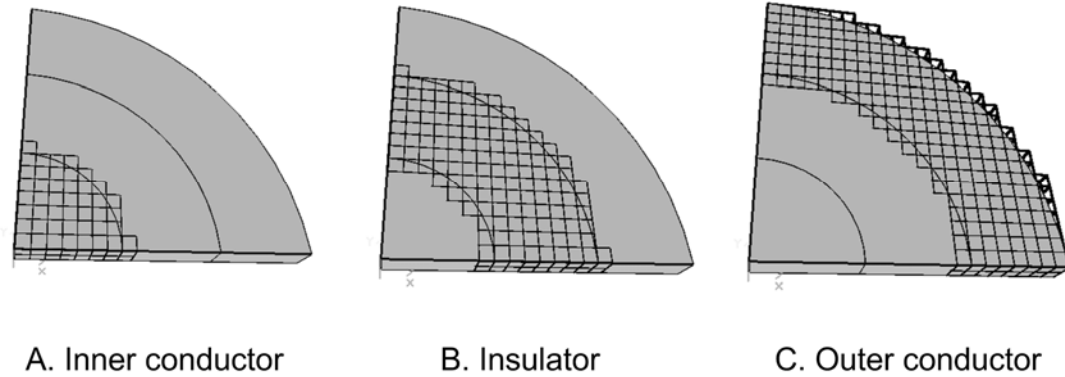


**Fig. 28 Magnitude of the magnetic field**

For 3D analysis it is necessary to first compute the current density by solving the electrostatics equations. Then using the computed current density, magnetic field is obtained through 3D magnetostatic analysis. The governing equations for the electro-magnetostatic problem is

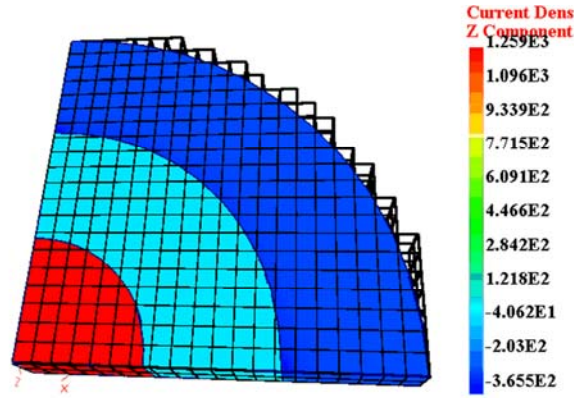
$$\begin{aligned} -\nabla \cdot (\sigma \nabla V) &= 0 & \text{in } \Omega \\ \nabla \times (\nu \nabla \times \mathbf{A}) &= \mathbf{J} & \text{in } \Omega \end{aligned} \quad (31)$$

where, the current density for magnetostatics is  $\mathbf{J} = -\sigma \nabla V$ . Fig. 29 shows the coaxial cable model using three separate structured grids.



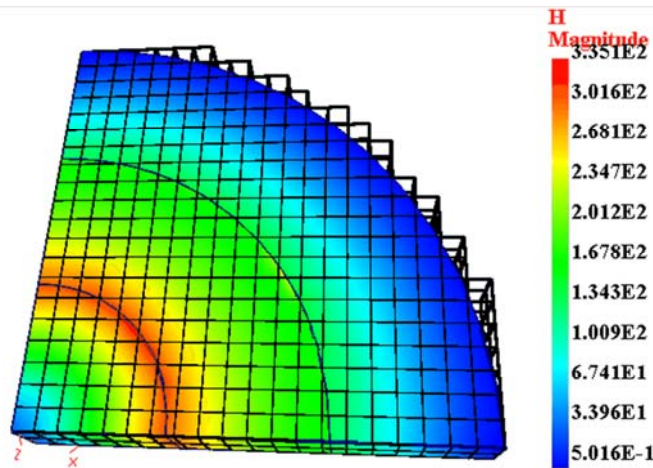
**Fig. 29 3D coaxial cable model with the structured grid**

The electric conductivity in the conductors is set to  $10^3 S/mm$  and  $10^{-3} S/mm$  in the insulator. In order to obtain  $I = 1000A$ , the voltage difference in the top and the bottom surfaces is set to 0.25 V in the inner conductor and 0.05 in the outer conductor. The current density of the inner conductor is computed as 1273 A/mm<sup>2</sup> and 254.6 A/mm<sup>2</sup> in the outer conductor to carry the amount of current.



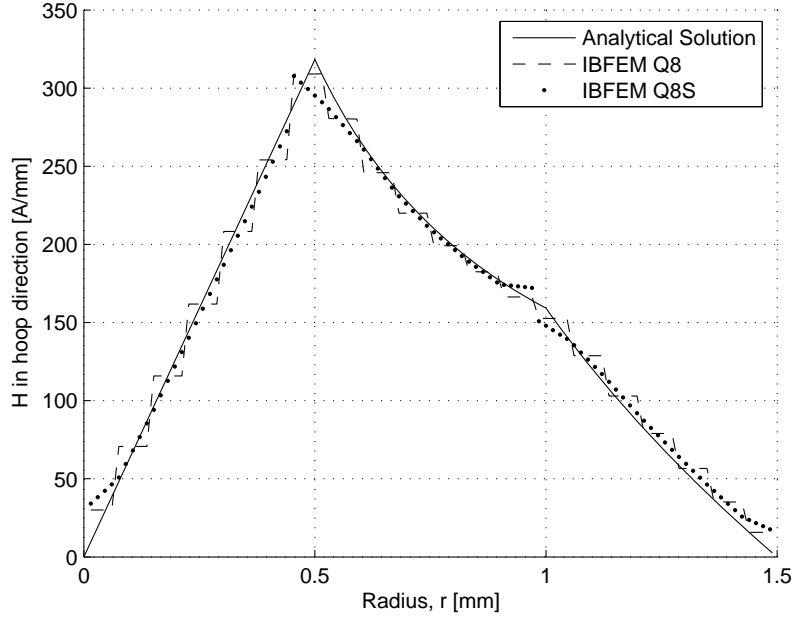
**Fig. 30** Current density in z-direction for 3D coaxial cable

Fig. 30 shows computed current density in z direction by 3D electrostatic analysis. The calculated current densities of the inner conductor and the outer conductor are 1259 and 365  $A/mm^2$ .



**Fig. 31** Magnetic field for 3D coaxial cable

Fig. 31 shows the magnitude of the magnetic field that was computed using 8 brick node elements. It shows that the maximum magnetic field value is at the interface between the inner conductor and the insulator and has a value of  $3.351 \times 10^2 A/mm$ . This is close to the value obtained from the analytical solution which is  $3.183 \times 10^2 A/mm$ .



**Fig. 32 Magnetic field versus radius**

Fig. 32 shows the magnetic field in the hoop direction varying with the radius. In the figure, results obtained by hexahedral 8-node elements are denoted as H8. This element provides a piece-wise trilinear interpolation for the vector potential. Therefore, the derivatives are not continuous without smoothing. The same results after smoothing are denoted in the figure as H8S. After smoothing, the result of IBFEM is very close to the analytical solution. Fig. 33 shows the convergence of H1 error norm for this problem using trilinear (H8) elements which is the root mean square error in flux density field over the domain and can be defined as

$$\|H_1\| = \left( \int_{\Omega} (\mathbf{B}^e - \mathbf{B}^h)^T \cdot (\mathbf{B}^e - \mathbf{B}^h) d\Omega \right)^{\frac{1}{2}} \quad (33)$$

where,  $\mathbf{B}^e$  is the exact value of the magnetic flux from the analytical solution and  $\mathbf{B}^h$  is the corresponding computed value.

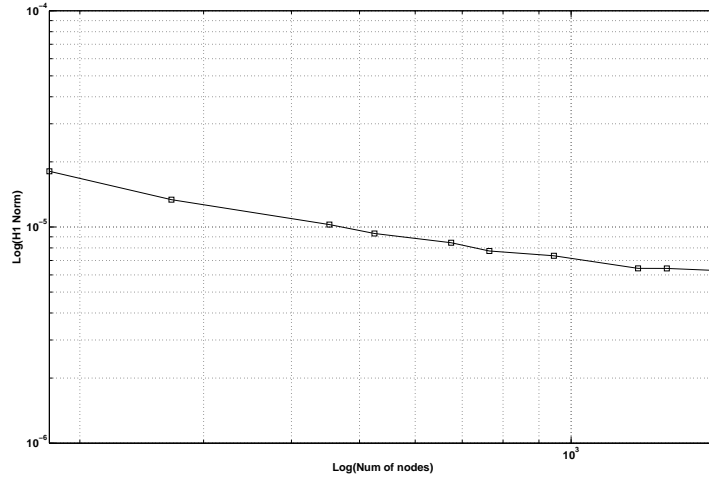


**Fig. 33 Convergence of H1 norm6.3. Plunger solenoid actuator**

### Switched Reluctance Motor

A 2D planar model of the Switched Reluctance Motor (SRM) is shown in Fig. 34 . SRM is a DC motor where the stator has windings around the poles while the rotor does not have any windings. Current is applied to the coils around the poles of the stator sequentially to produce a torque on the rotor as it rotates.

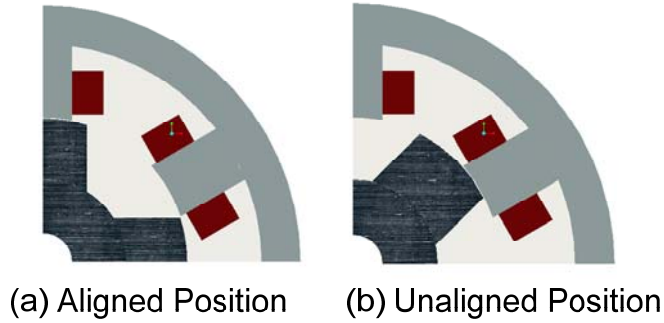


**Fig. 34 Switched reluctance motor**

Reference [68] provides the dimensions of the motor that are used in this example. The stator and the rotor are made of iron with relative permeability of 2000. A quarter of the motor is modeled in both its aligned and unaligned orientation. The number of turns in the coil is assumed to be 500 and the current is 2 A. Currents only flows into coils attached to the top pole of the stator. Essential boundary condition ( $A=0$ ) is imposed on peripheries of the shaft and the stator and the vertical axis. B-spline elements are used for the analysis so that accurate results are obtained even with a sparse grid as shown in Fig. 35 . The flux lines computed here are similar those computed by FEM [68]. Note that the air gap is very small compared to the average

element size in the grid. Despite the geometric complexity and large number of parts and materials involved, this approach for analysis yields results using structured grids comparable to results from traditional FEM using conforming mesh.

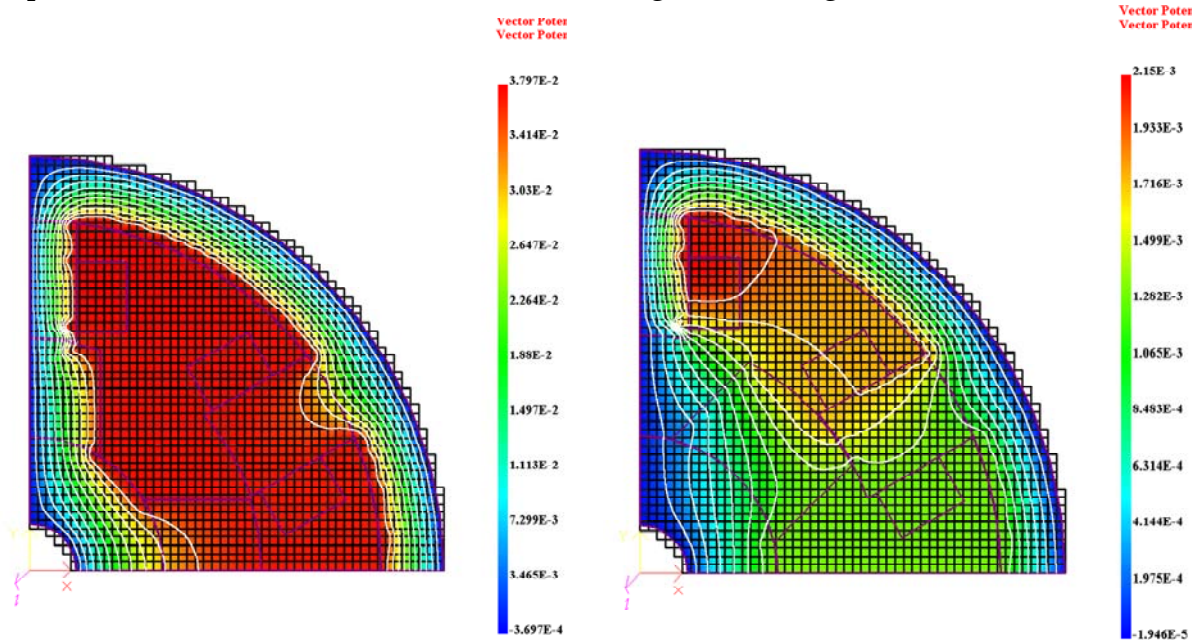
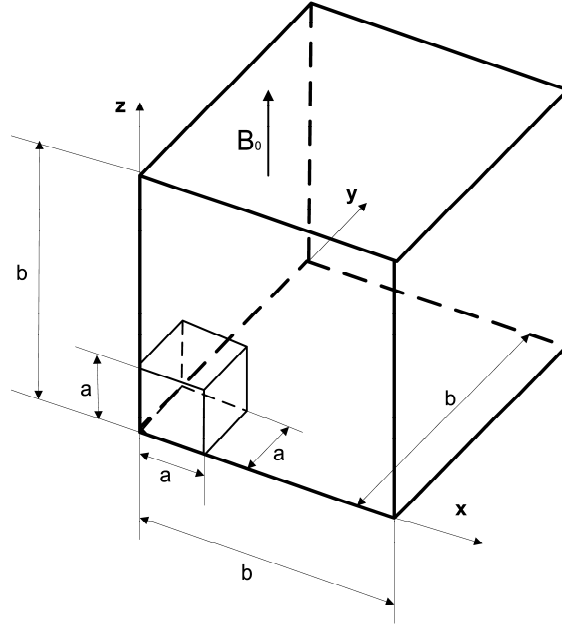


Fig. 35 Field lines

### Iron block in a homogeneous magnetic field

The example of an iron cube in air subject to homogenous magnetic field has been used in literature to verify a variety of formulations. Fig. 36 shows one-eighth of the system modeled considering its symmetry. The relative permeability of iron cube is 1000. The modeled region is subjected to a homogenous magnetic flux density  $\mathbf{B}_0$  in the z-direction.



**Fig. 36 Iron cube in homogeneous magnetic field**

The half-length of the iron cube edge is 'a'. The symmetry plane are  $x=0$ ,  $y=0$  and  $z=0$ . The planes  $x=b$ ,  $y=b$ , and  $z=b$  represent the far boundaries. A homogeneous magnetic field is applied in the  $z$ -direction with the aid of boundary conditions. On the far boundaries, the Dirichlet boundary conditions are:  $A_y = \frac{B_0 b}{2}$  and  $A_z = 0$  on  $x=b$  and  $A_x = -\frac{B_0 b}{2}$  and  $A_z = 0$  on  $y=b$ . The dimensions used are  $a = 20mm$ ,  $b = 40mm$  and the flux density magnitude is  $B_0 = 1.0 \text{ T}$ . In addition to this, the following essential boundary conditions are also imposed

$$\mathbf{n} \times \mathbf{A} = 0 \quad \text{on } \Gamma_B \text{ (} x=0 \text{ and } y=0 \text{)} \quad (29)$$

$$\mathbf{n} \cdot \mathbf{A} = 0 \quad \text{on } \Gamma_H \text{ (} z=0 \text{ and } z=b \text{)} \quad (30)$$

As the magnetic flux density only exists in the  $z$ -direction, the normal components of magnetic flux density must be zero on the symmetry planes and the tangential component of magnetic field must be zero on planes normal to the  $z$  direction.



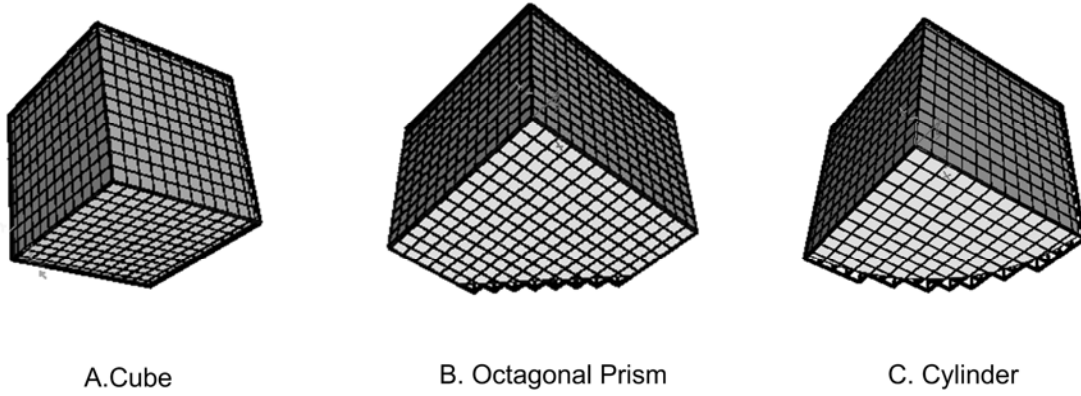


**Fig. 37 Iron objects with the same grid density**

In addition to modeling the iron cube, we have modeled two other shapes as shown in Fig. 37 , where the iron part is modeled as an octagonal prism and a cylinder. The height of the parts is the same and equal to 20mm. The edge length of the right octagonal prism is 20mm and the cylinder has radius = 20mm. The total number of elements used in the model is 12167.

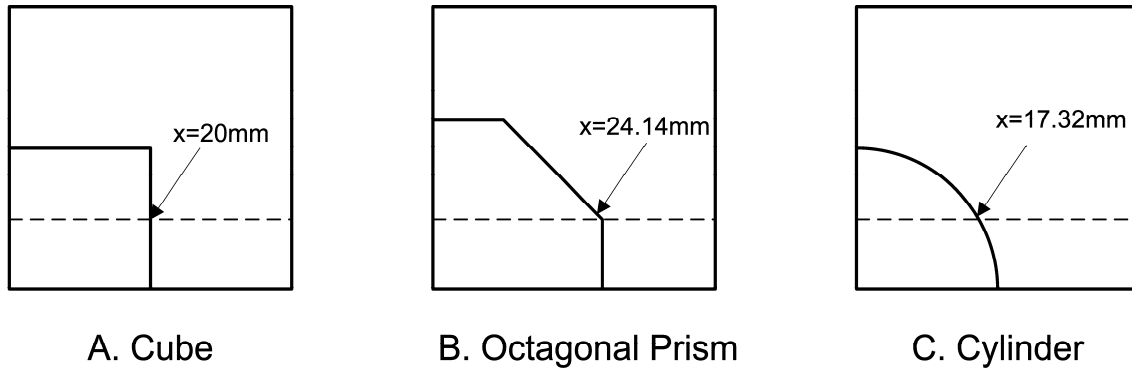
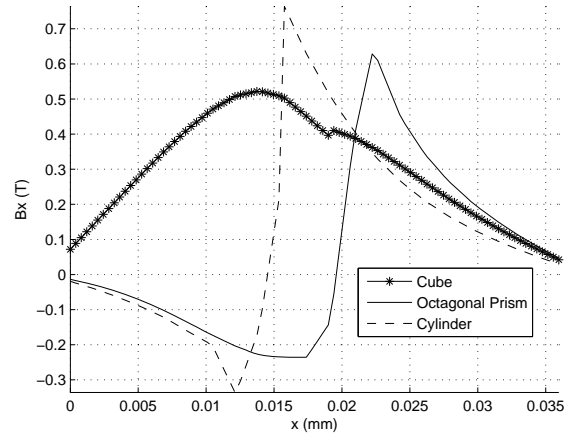
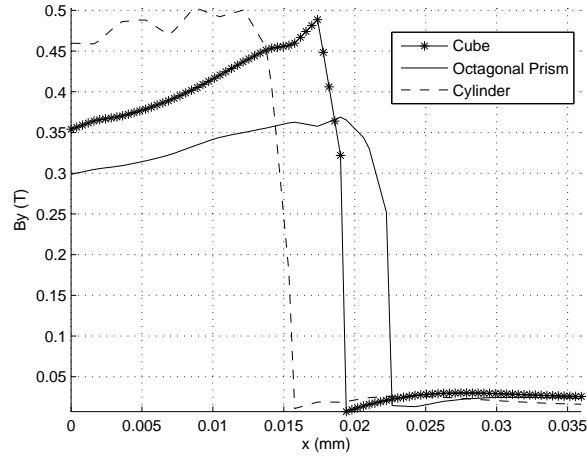


**Fig. 38 Cross-sections with the line  $y=z=10\text{mm}$**

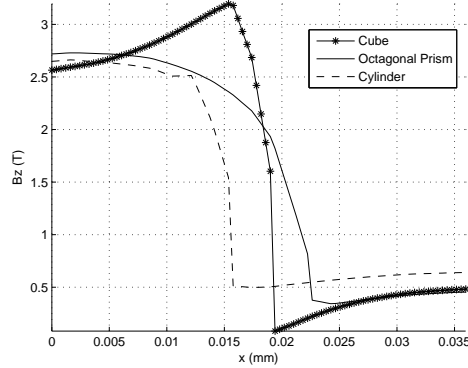
As shown in Fig. 38 , along the line  $y=z=10\text{mm}$ , the interface between iron and air is at  $x=20\text{mm}$  for the cube, at  $x=24.14\text{mm}$  for the right octagonal prism and at  $x=17.32\text{mm}$  for the cylinder. Using the same number of elements and the same boundary conditions for all three cases, the variation on the three components of magnetic flux B along the line  $y=z=10\text{mm}$  are obtained as shown in Fig. 39



(a)



(b)



(c)

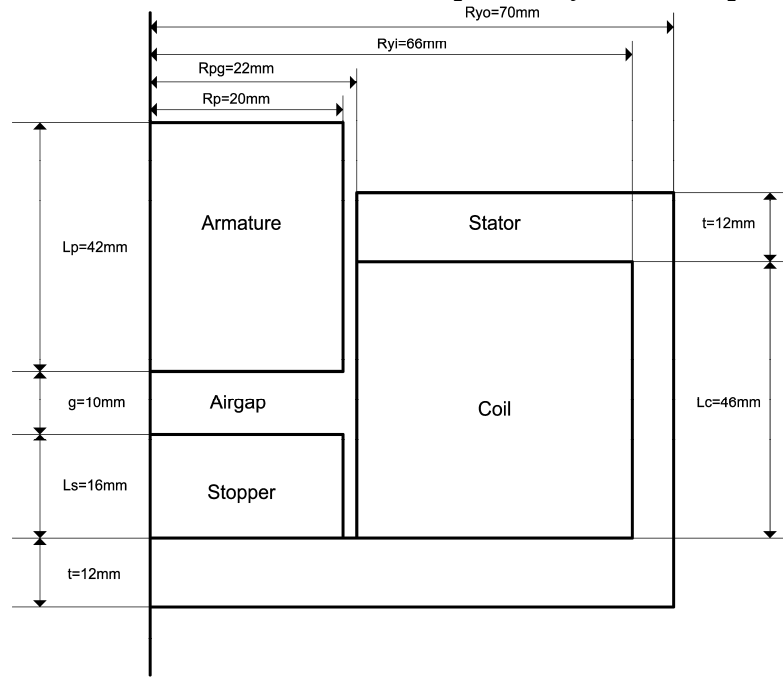
**Fig. 39 Components of B along the line  $y=z=10\text{mm}$ . (a)  $B_x$  (b)  $B_y$  (c)  $B_z$**

Fig. 39 (a) shows that only the magnetic flux density in x-direction is continuous when the shape of the iron is cubic because the normal direction of the interface is along the x-direction. The other components are tangential components and are discontinuous

as expected. Similarly, for other shapes none of the components of  $B$  are normal components and therefore none of them are continuous at the interface. The results obtained for this example are similar to that obtained using the traditional FEM that uses conforming mesh.

### Plunger solenoid actuator

Solenoid actuators are designed to produce small linear motion of an armature and are of several types depending on the shape of the armature. A solenoid actuator with a plunger armature [69], as shown in Fig. 40 is considered in this example. The armature and stator are made of steel laminates in order to reduce eddy current effect. The stator has solenoidal coil, wound in the shape of a cylinder, or parallelepiped.



**Fig. 40 Plunger solenoid actuator**

In Fig. 41 (a) the plunger is cylindrical and the solenoid is axisymmetric, while in Fig. 41 (b), the plunger has square cross-section with rounded edges. We have referred to the later actuator with square cross-section as the brick plunger actuator. For both models, the number of turns  $N=400$  and the current  $I=4\text{A}$ . The relative permeability of the stator, the armature and the stopper is  $\mu_r = 2000$  and  $\mu_r = 1$  in the coil.

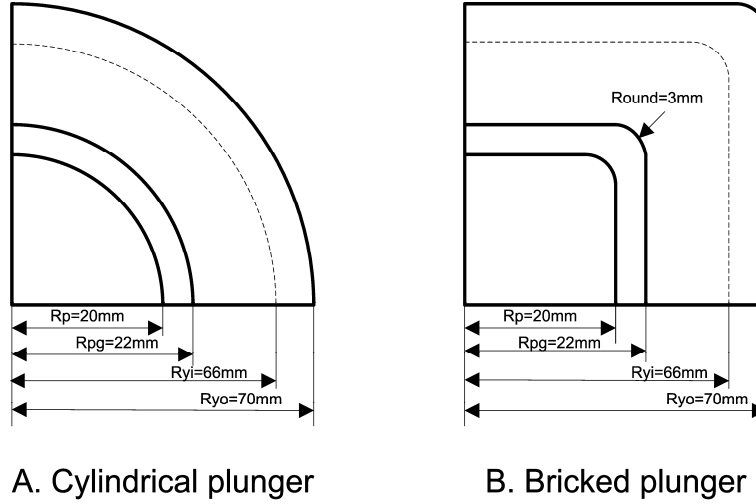


**Fig. 41 Top view of plunger actuators**

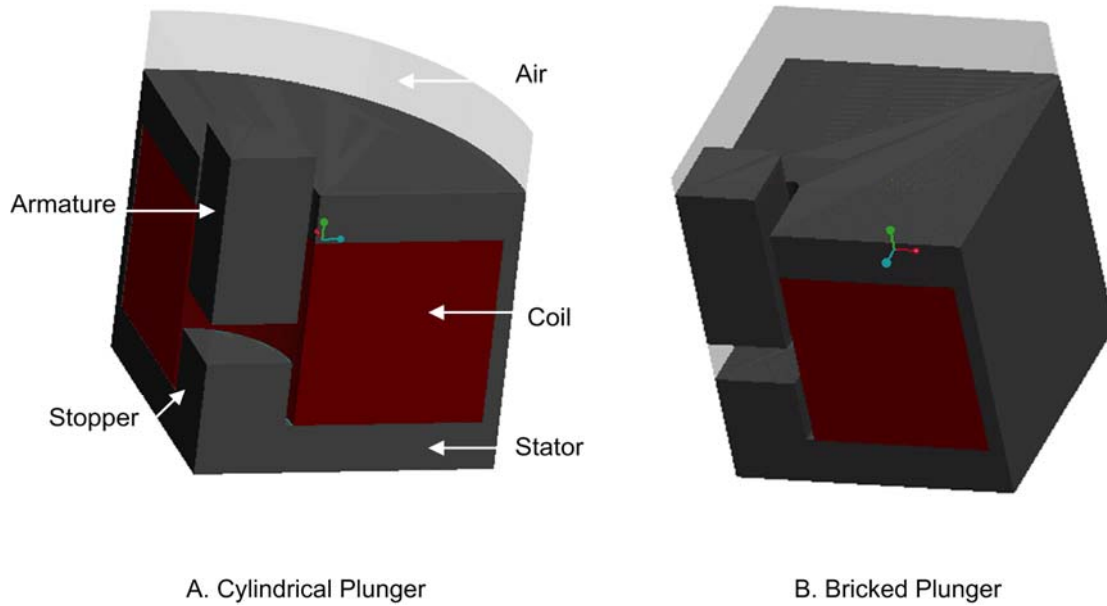


**Fig. 42 3D solid models of the solenoid actuators**

Fig. 42 shows 3D solid models of the solenoid actuator model, which were used for the analysis. In order to reduce the computational effort, only a fourth of the whole system is modeled. The current density in the coil is in the circumferential direction and is obtained by first solving an electrostatic problem. A voltage difference of 0.0546 V was applied between the symmetry planes of the coil. Assuming the conductivity of the coil to be  $\sigma = 10^6 S/m$  the current density obtained will be on average the same as the current density applied for the 2D axisymmetric model. The same voltage boundary

conditions are applied for the brick plunger actuator. Using 3D electrostatic analysis, the computed current density is obtained as shown in Fig. 43 .

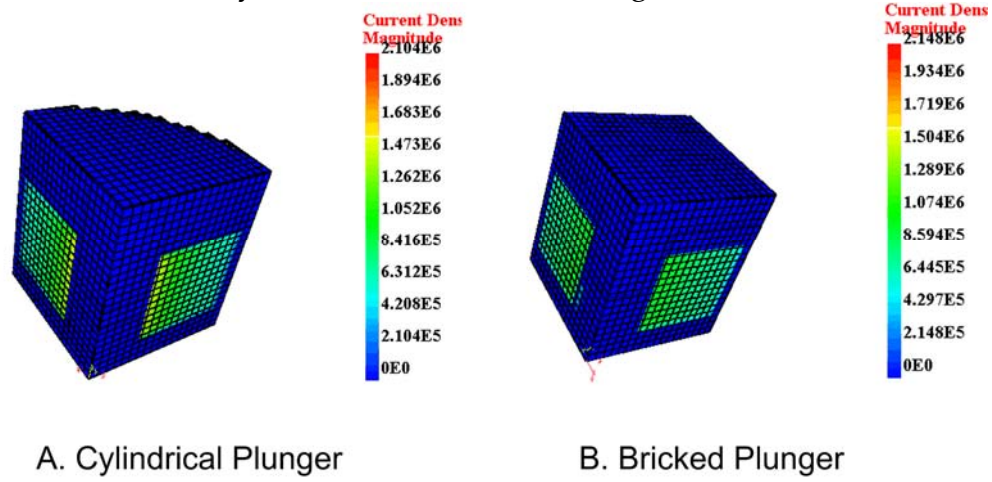


**Fig. 43 Magnitude of current density**

The computed current density is then used to perform the magnetostatic analysis, to compute magnetic flux density and magnetic field. At the symmetric planes, the essential boundary conditions,  $\mathbf{n} \times \mathbf{A} = 0$  , are applied. The computed magnetic flux density is shown in Fig. 44 .

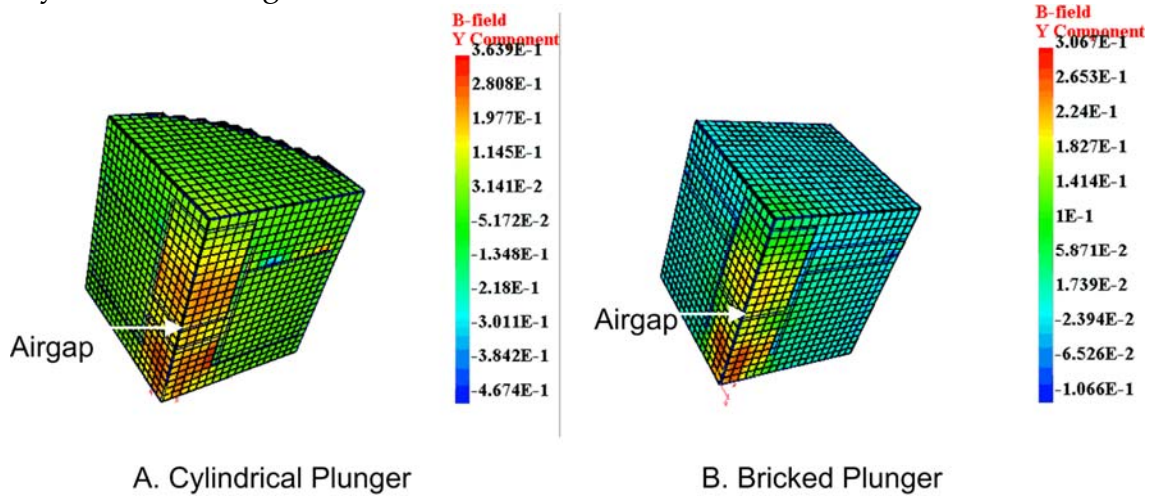


**Fig. 44 Magnetic flux density in y direction**

For the axisymmetric case, using the reluctance method, the magnetic flux density in the air gap can be calculated as  $B=0.1715$  T and the magnetic force is  $F=14.7$  N. Brauer [69] has also provided 2D FEM results;  $B=0.170$  T and  $F=19.34$  N. The magnetic flux density computed using IBFEM is also roughly in this range. The computed magnetic field density in the y- direction is shown in Fig. 45 .

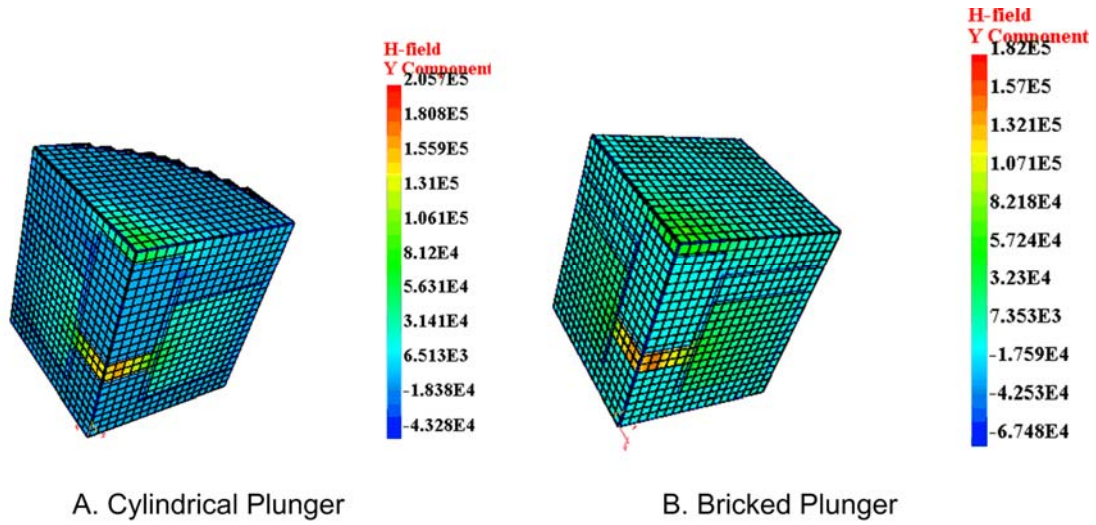


**Fig. 45 Magnetic field in y direction**

Fig. 45 (A) shows that the computed magnetic field in y direction is close to the value of  $1.364 \times 10^5$  A/m computed using the reluctance method [69]. Using the magnetic field and flux density, the computed magnetic force on the cylindrical armature is 18.33 N, which is quite close to the force calculated by 2D FEM. For the brick plunger armature, the computed force is 19.56 N. According to this analysis, the force on the brick shaped armature is larger than on the cylindrical armature because the cross-sectional area of the bricked armature ( $1.592 \times 10^{-3} \text{ m}^2$ ) is larger than that of the cylindrical armature ( $1.257 \times 10^{-3} \text{ m}^2$ ).

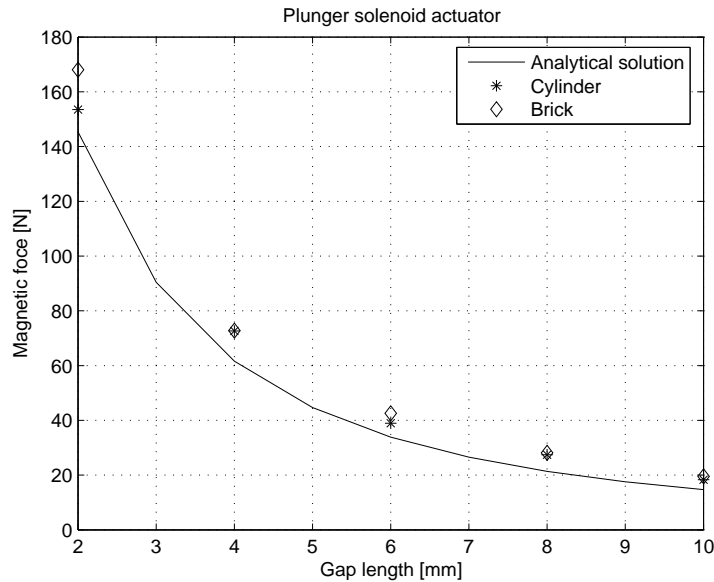


**Fig. 46 Magnetic force versus gap**

Fig. 46 shows magnetic force versus gap between the armature and the stopper. The analytical solution plotted was obtained using the reluctance method for the case when the armature is cylindrical. When the gap is changed from 2mm to 10mm, the magnetic force decreases. Structured mesh with the same number of nodes and elements was used for each analysis as the gap was varied. For the cylindrical plunger solenoid, the number of nodes is 10984. For the brick plunger solenoid, the total number of nodes is 10876. The computed values are higher than the analytical values because the reluctance method ignores fringe effects. Magnetic force of the brick plunger is a little higher than the force of the cylindrical plunger.

## 2D Clapper solenoid actuator with cantilever beam

A cantilever beam is attached to the top surface of the armature. The cantilever beam is a beam fixed at one end and attached to the moving armature at the other end. The attachment location varies as shown in Fig. 47 . The distances from the center axis to the tip of the beam are 10mm, 20mm, and 28mm. The thickness of the beam is 5mm and the length of the beam is 80mm. The beam is made of aluminum whose material properties are  $E = 69 \text{ Gpa}$ ,  $\nu = 0.29$  and  $\mu_r = 1$ .

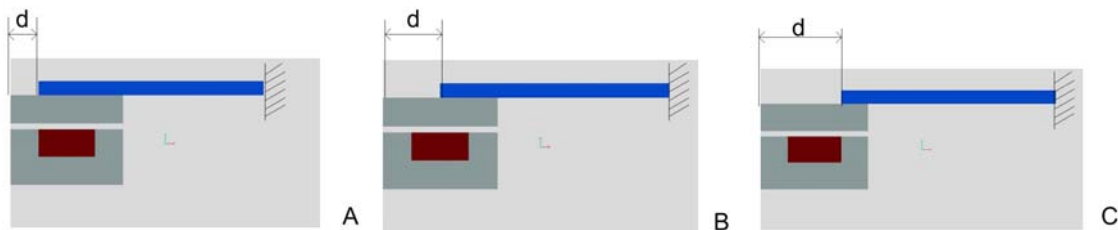


**Fig. 47 Planar clapper solenoid actuator with a cantilever beam. A)  $d=10\text{mm}$  B)  $d=20\text{mm}$  and C)  $d=28\text{mm}$**

For this analysis, 4 node bilinear elements were used. The total number of elements in the model was 1550. Fig. 48 shows the tip displacement versus ampere-turns. As NI increases, the displacement on the tip increases. When  $d=20\text{mm}$  or  $28\text{mm}$ , the displacements at the tip is much larger than when  $d=10\text{mm}$ . However, there is very small difference in tip deflection between the two cases where  $d=20\text{mm}$  and  $d=28\text{mm}$ .

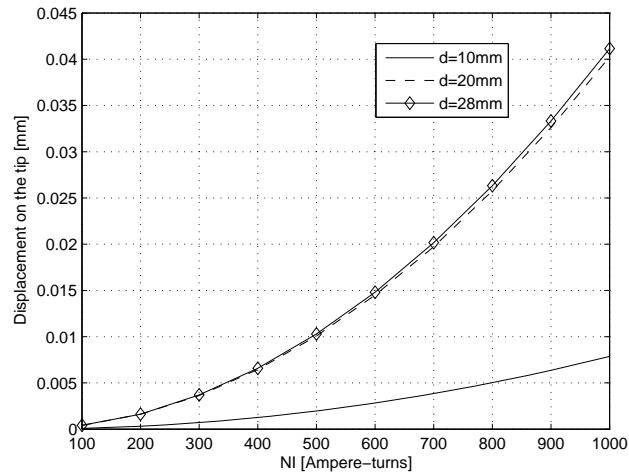


**Fig. 48** Displacement on the tip versus. NI according to the location of the beam

### 3D Plunger solenoid actuator with structures

The plunger solenoid actuator with one of the three plates shown in Fig. 49 attached to its armature, was modeled using 3D elements. The top views of each the plate structures and dimensions are shown in the figure. The first structure is a solid plate, the second is a plate with one hole, and the third one is a plate with two holes. The thicknesses of all plates are 2mm. All of the three structures is attached on the top surface of the plunger armature as shown in Fig. 50 . The structures are made of aluminum.

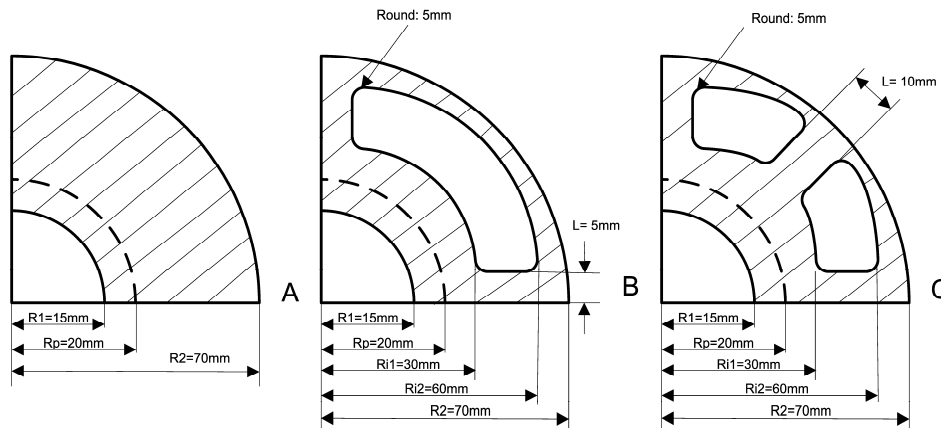


**Fig. 49** Top views of structures attached on the plunger armature. A) Solid plate, B) plate with one hole, and C) plate with two holes



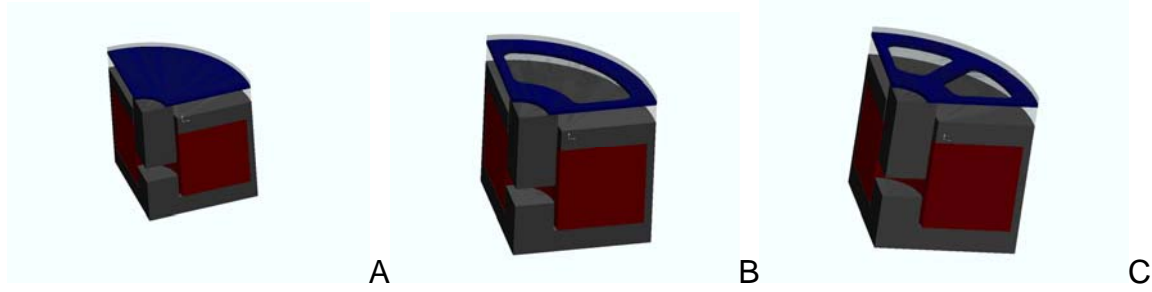


**Fig. 50** 3D plunger solenoid actuators with attached structures. A) Solid plate, B) plate with one hole, and C) plate with two holes

When  $NI=800$  and the fixed boundary conditions are applied on the surfaces of the structure at  $R=70\text{mm}$ , the magnetic force from the actuator results in the deflection of the plate structures as shown in Fig. 51 .

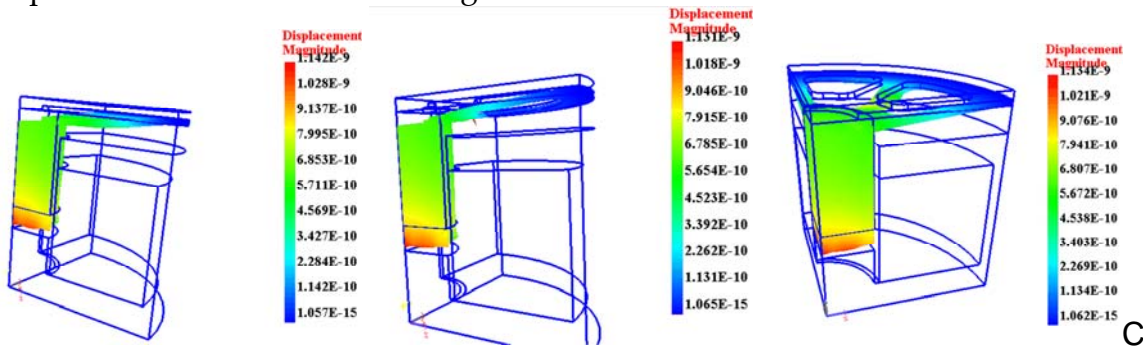


**Fig. 51** Deformed structures: A) Solid plate, B) plate with one hole, and C) plate with two holes

The maximum displacements for the structures are  $7.24 \times 10^{-7} \text{mm}$  in the solid plate,  $1.086 \times 10^{-6} \text{mm}$  in the plate with one hole, and  $8.539 \times 10^{-7} \text{mm}$  in the plate including two holes. Fig. 52 shows the maximum displacement versus  $NI$  (ampere-turns) for each plate. Among the three structures, the plate with one hole has the largest deformation while the solid plate has the highest stiffness.

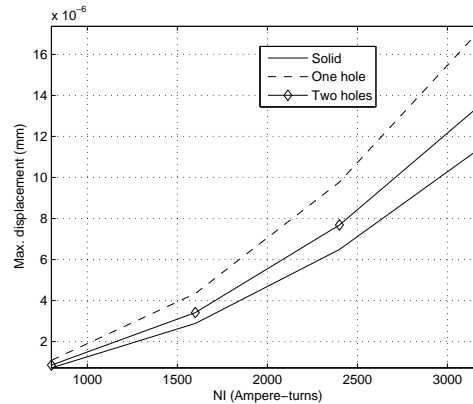


**Fig. 52      Maximum displacement versus NI**

## **7. Discussion**

Magnetostatic analysis using structured mesh has been demonstrated using solution structures for applying boundary and interface conditions. The method allows geometry imported from solid modeling systems to be directly used for analysis without approximation using a mesh. The approach has been demonstrated for both 2D and 3D magnetostatic models. Structured mesh is easy to generate and the elements are regular and not distorted as in traditional finite element mesh. Furthermore, the internal elements are identical to each other and have the same stiffness matrix thus reducing the computation required. The global equations were solved using direct solvers rather than iterative solvers whose performance deteriorates when the global matrix is ill-conditioned.

Magnetic forces were computed by integrating the magnetic force density. Alternative approaches such as the virtual work principle can also be implemented with the implicit boundary approach. If the force generated by magnetic forces significantly deform the structures on which the magnets are mounted then it is necessary to perform a fully coupled magneto-elastostatic analysis to compute the resultant deformation. In this case, since the magnetic field can be altered by the deformation of the structure, it leads to a nonlinear formulation of the coupled problem. The approach presented in this report needs to be extended in the future to such nonlinear problems as well as dynamics problems. Since 3D analysis is computationally expensive, it is not always desirable to use a uniform mesh everywhere. Mesh refinement techniques are needed that locally refine the mesh while still using a structured mesh that has regular shaped elements. Development of such local refinement techniques is part of the future work needed to make 3D magnetostatic analysis more feasible.

## V. MODELING SHELLS USING IBFEM

### 1. Overview

Shell theories are extended from the traditional plate theories. The two plate theories that have been extensively studied and implemented in FEM are the classical or Kirchhoff's plate theory and the first order or Mindlin plate theory. The classical plate theory is also called the thin plate theory because it is based on Kirchhoff's assumption that for thin shells shear strain energy is negligible. Mathematically, this assumption implies that the rotation at any point in plate is the slope of deflection at that point. The weak form of the plate equations derived using this assumption contains volume integral of the second derivatives of deflection. As a result, the test and trial functions constructed for this weak form must be  $C^1$  continuous interpolation or approximation of the nodal values. This is difficult to achieve using traditional interpolation schemes and therefore the results obtained using these elements are not reliable for thick plates and shells. Due to these drawbacks, the thick plate theory or first order plate theory, based on Mindlin's assumption [70], are often preferred. In this theory, the deflection and rotation at any point in the plate are independent of each other. The shear strain is assumed to be constant and equal to the difference between the slope and rotation. This assumption allows the plate elements to be  $C^0$  continuous because the weak form derived using Mindlin's assumption involves only the first derivatives of the deflection. Plate elements can be extended to simple flats shells by incorporating in-plane strains, allowing it to handle both in-plane forces as well as bending forces. Curved structures are approximated by adequate number of flat elements [71]. The flat shell elements uses linear or bilinear approximation which is typically  $C^0$  continuous. More advanced shells based on curvilinear coordinates have also been formulated based on Mindlin theory.. Straightforward implementation of Mindlin plate theory is good for thick plates but under-predicts deflections for relatively thin plates. Very thin plates or shells, exhibit the so called shear-locking in plates and shells [72]-[75]. Various techniques have been proposed to circumvent shear locking. Reduced integration is the best-known solution for shear locking [76]. Increasing the order of the polynomials used for the interpolation also improves the solution. A variety of mixed formulations have also been successfully employed to eliminate locking and to explain why reduced integration works [75]-[77].

The analysis of shells using 3D structured mesh is presented in this chapter. A structured mesh is a non-conforming mesh in which all the elements are regular in shape (rectangles/cuboids). In traditional FEM, shell elements are two dimensional flat or curved elements that approximate the geometry as shown in Fig. 53 . Fig. 53 (b) shows a shell modeled using a 3D structured mesh where the shell geometry, represented using parametric surfaces, passes through the elements of the grid.

Therefore, the geometry is independent of the mesh and could be represented using the exact equations imported from CAD models. The use of structured mesh also allows uniform B-spline basis functions to be used to represent the solution so that the displacement field is represented as  $C^1$  or  $C^2$  continuous function.

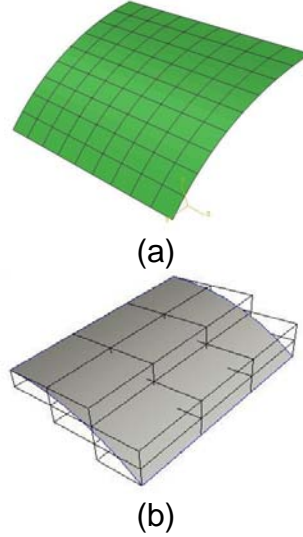


**Fig. 53 FEM mesh versus structured mesh for shells**

A structured mesh is much easier to generate than a conforming finite element mesh. Automatic mesh generation algorithms for FEM can be unreliable for complicated geometries often resulting in poor or distorted elements and such distorted elements is one of the main causes of errors in FEM solution. Significant amount of user intervention is required rectify the mesh. Moreover, the analysis geometry is poorly approximated using elements, especially when flat shell elements are used. These limitations associated with mesh generation can be avoided by using a structured mesh for analysis.

The nodes of a structured mesh are not guaranteed to lie on the analysis boundary, and therefore the traditional methods used in FEM for applying essential boundary conditions cannot be used. Implicit boundary method [42]-[45] has been shown to be an efficient and accurate method for applying boundary conditions when the equations of the boundary are available. We extended this method to handle boundary conditions for shells. The performance and capabilities of IBFEM shell elements are studied by solving several shell problems in structural analysis.

## **2. Implicit Boundary Method**

The implicit boundary method uses approximate step functions of the boundary  $\phi(\mathbf{x})=0$  to construct solution structures for the solution such that the displacement

boundary conditions are guaranteed to be satisfied. Let  $u_i$  be displacement component that must satisfy the boundary condition  $u_i = a_i$  along a subset of the boundary of the domain. If  $D_i(\mathbf{x})=0$  is an implicit equation of the boundary  $\Gamma_a$ , then the solution is constructed as [44]-[45].

$$u_i(\mathbf{x}) = D_i(\mathbf{x})u_i^s(\mathbf{x}) + u_i^a(\mathbf{x}) \quad (5.1)$$

The solution structure for the solution defined in Eq. (5.1) is then guaranteed to satisfy the condition  $u_i = u_i^a$  along the boundary defined by the implicit equation  $D_i(\mathbf{x})=0$ . The boundary value function,  $u_i^a$ , must be defined such that at the boundary  $\Gamma_a$  it has the prescribed value  $u_i^a = a_i$ . The variable part of the solution structure is the function  $u_i^s(\mathbf{x})$  which is defined by piece-wise interpolation or approximation over the elements of the grid. The functions,  $D_i(\mathbf{x})$ , referred to here as the D-functions, are constructed as approximate step functions, if essential boundary conditions are imposed on the  $i^{\text{th}}$  component of displacement. These functions are defined using implicit equations of the boundary,  $\phi(\mathbf{x})=0$ , as

$$D_i(\mathbf{x}) = \begin{cases} 0 & \phi(\mathbf{x}) \leq 0 \\ 1 - \left(1 - \frac{\phi(\mathbf{x})}{\delta}\right)^k & 0 \leq \phi(\mathbf{x}) \leq \delta \\ 1 & \phi(\mathbf{x}) \geq \delta \end{cases} \quad (5.2)$$

If no boundary conditions are applied on a boundary, then we set  $D_i(\mathbf{x})=1$  at that boundary. The D-functions take a value of zero and has non-zero gradient at boundaries. In the limit as  $\delta \rightarrow 0$  this D-function approximates the Heaviside step function which has a unit value inside the domain where  $\phi > 0$  and is zero at the boundary and outside ( $\phi \leq 0$ ). The use of an approximate step functions as the D-functions in implicit boundary method ensures that only the boundary elements are affected by this function. The variable part of the solution structure  $u_i^s(\mathbf{x})$  can be defined using B-spline or other approximations that provide a high order continuity. Uniform B-spline elements applicable to structured mesh have been studied in the past [44],[46] to demonstrate that the implicit boundary method can be used to apply boundary conditions even when the approximation used does not have Kronecker's delta properties. In other words, even though the nodal values are not equal to the B-spline approximation values at the nodes, the solution structure in Eq. (5.1) guarantees that the essential boundary conditions are imposed.

For shells, the boundary is a curve on a surface and essential boundary conditions specify values of displacements along the curved boundary or the local slopes on these curves. Both these boundary conditions can be imposed by appropriately constructing

the characteristic functions  $\phi(\mathbf{x})$  for the boundary curves. To apply displacement boundary conditions, where the slope is not fixed, the characteristic function is defined as the radial distance from the curve. In order to model clamped boundary condition, where both slope and displacement are fixed, the characteristic function is defined as the distance from a imaginary surface that passes through the boundary curve and is normal to the shell surface.

The weak form of the elastostatic boundary value problem is the principle of virtual work which can be written in the following form:

$$\int_{\Omega} \delta \boldsymbol{\varepsilon}^T \boldsymbol{\sigma} d\Omega = \int_{\Gamma_f} \delta \mathbf{u}^T \mathbf{t} d\Gamma + \int_{\Omega} \delta \mathbf{u}^T \mathbf{b} d\Omega \quad (5.3)$$

Using the solution structure in Eq. (5.1) the stresses and strains can also be decomposed into a homogeneous part and a boundary value part.

$$\begin{aligned} \boldsymbol{\varepsilon} &= \boldsymbol{\varepsilon}^s + \boldsymbol{\varepsilon}^a \\ \boldsymbol{\sigma} &= \mathbf{C} \boldsymbol{\varepsilon} = \mathbf{C}(\boldsymbol{\varepsilon}^s + \boldsymbol{\varepsilon}^a) = \boldsymbol{\sigma}^s + \boldsymbol{\sigma}^a \end{aligned} \quad (5.4)$$

Where,

$$\varepsilon_{ij}^s = \frac{1}{2} \left( \frac{\partial u_i^s}{\partial x_j} + \frac{\partial u_j^s}{\partial x_i} \right), \quad u_i^s = D_i u_i^g, \quad \varepsilon_{ij}^a = \frac{1}{2} \left( \frac{\partial u_i^a}{\partial x_j} + \frac{\partial u_j^a}{\partial x_i} \right).$$

The Dirichlet function,  $D_i$ , is defined as per Eq. (5.2) for each displacement component for which essential boundary condition is specified. Substituting the preceding equations into the weak form, the following relation is obtained, where the known quantities have been moved to the right hand side of the equation.

$$\int_{\Omega} \delta \boldsymbol{\varepsilon}^T \mathbf{C} \boldsymbol{\varepsilon}^s d\Omega = - \int_{\Omega} \delta \boldsymbol{\varepsilon}^T \boldsymbol{\sigma}^a d\Omega + \int_{\Gamma_f} \delta \mathbf{u}^T \mathbf{T} d\Gamma + \int_{\Omega} \delta \mathbf{u}^T \mathbf{b} d\Omega \quad (5.5)$$

The boundary value function  $\mathbf{u}^a$  must be constructed such that at the boundary where Dirichlet boundary conditions are applied it must have value equal to the specified boundary condition at that boundary. When Dirichlet boundary conditions are specified at multiple boundaries and the assigned values are not the same for all boundaries, the boundary value function must take on appropriate values at respective boundaries and transition smoothly in between. To accomplish this, the boundary value function is constructed by piecewise interpolation or approximation using the shape functions  $N_i$  of the elements through which the boundary is passing. A displacement component  $u_i^a$  is defined within an element as  $u_i^a = \sum_j N_j u_{ij}^a$ , where  $u_{ij}^a$  are the nodal values of the displacement component.

### 3. B-Spline approximations

B-spline shape (basis) functions are traditionally constructed using a recursive definition (Farin, 2002). The parameter space is partitioned into elements using a knot vector (equivalent to a collection of nodes). General methods are available to insert knots and elevate the order of the polynomial. However, for implementation in structured mesh finite element analysis, it is convenient to define shape functions within each element of the mesh such that the parametric domain of the element is  $[-1,1]$  in the three parametric directions. The use of such shape functions for such uniform B-splines shape functions have been demonstrated in past work for 3D elastostatic elements [44]. Here we briefly summarize the main ideas and provide the shape functions that were used for shell analysis.

The shape functions for one dimensional elements are derived using the continuity requirements between neighboring elements. Any  $k^{th}$  order B-spline has  $k+1$  support nodes. A quadratic B-spline element in one-dimension has three nodes and therefore it is represented by three shape functions. The coefficients of the shape function are determined by requiring the approximations and its slope to be continuous between elements. Additionally, the shape functions are required to be partition of unity. The expression of the shape functions are given below,

$$\begin{aligned} N_1 &= \frac{1}{8}(1-2r-r^2) \\ N_2 &= \frac{1}{8}(6-2r^2) \\ N_3 &= \frac{1}{8}(1+2r+r^2) \end{aligned} \tag{5.6}$$

The plots of the shape functions in Eq. (5.6) are shown in Fig. 54

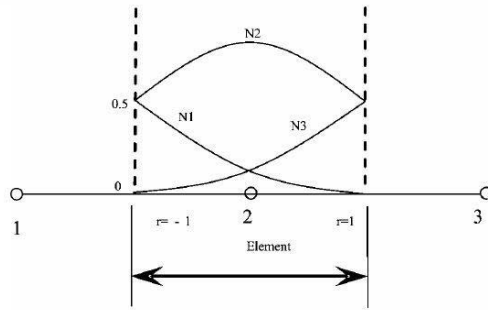


**Fig. 54** Shape function of one dimensional quadratic B-spline element

A cubic B-spline element in one-dimension has four nodes and therefore it is represented by four shape functions. These shape functions are derived by requiring the approximation, its slope and curvature to be continuous between elements. These shape

functions are also required to be a partition of unity. The expression of the shape functions are given below,

$$\begin{aligned}
 N_1 &= \frac{1}{48}(1 - 3r + 3r^2 - r^3) \\
 N_2 &= \frac{1}{48}(23 - 15r - 3r^2 + 3r^3) \\
 N_3 &= \frac{1}{48}(23 + 15r - 3r^2 - 3r^3) \\
 N_4 &= \frac{1}{48}(1 + 3r + 3r^2 + r^3)
 \end{aligned} \tag{5.7}$$

The plots of the shape functions in Eq. (5.7) are shown in Fig. 55. This figure shows that the B-splines are not unity at respective nodes and do not vanish at other nodes. This shows that they do not interpolate nodal values. Instead, smooth approximations of the nodal values are created.

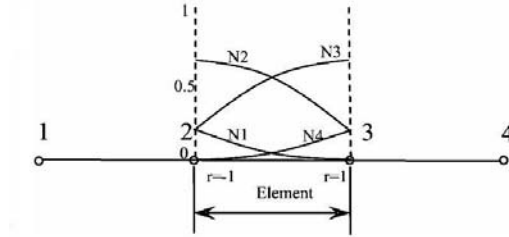


**Fig. 55 Shape function of one dimensional cubic B-spline element**

The shape functions for the higher dimensional B-spline elements are constructed as products of the shape functions for one-dimensional B-splines. The structured grid consists of regular hexahedra (cube/cuboid), so the mapping from parametric space to the physical space is linear. The mapping between parametric and physical space can be defined as

$$x_i = \frac{1-r_i}{2} x_i^l + \frac{1+r_i}{2} x_i^u \tag{5.8}$$

where,  $x_i^l$  and  $x_i^u$  are the lower and upper bounds respectively for nodal coordinates of any given element.

The shape functions for two and three-dimensional cubic B-splines are constructed as a product of one-dimensional corresponding one-dimensional shape functions. The shape functions can be expressed as,

$$\begin{aligned}
 N_{4(j-1)+i}^{2D}(r, s) &= N_i(r)N_j(s) \\
 N_{16(k-1)+4(j-1)+i}^{3D}(r, s, t) &= N_i(r)N_j(s)N_k(t)
 \end{aligned} \tag{5.9}$$



#### 4. Numerical Implementation

The B-spline shell elements are implemented as three-dimensional regular elements (cube/cuboid) that are part of a structured mesh and each element contains a portion of the surface representing the shell as shown in Fig. 53. The stiffness matrix for linear elastic elements is computed as

$$K^e = \int_{V_e} [B]^T [C] [B] dV \quad (5.10)$$

Only a portion of the shell surface that intersects with the element contributes to its stiffness. The volume integration in Eq. (5.10) is evaluated as a combination of area and thickness integration. In order to integrate accurately over the portion of the surface passing through the element, intersection between the surface and the element is computed and triangulated. The stiffness is then computed by integrating over these triangles and adding the results as follows

$$[K] = \sum_{i=1}^{n_t} \int_{-\frac{h}{2}}^{\frac{h}{2}} \left( \int_{A_i} [B]^T [C] [B] dA_i \right) dh \quad (5.11)$$

In Eq. (5.11)  $A_i$  is the area of the  $i^{th}$  triangle and  $h$  is the thickness of the shell.

For boundary elements that contain boundaries with essential boundary conditions, the D-functions sharply dip from unit value to zero near the boundary over a narrow band of width  $\delta \approx 10^{-5}$ . The gradients of D-function over these narrow bands can have large values. In order to accurately compute the contribution of the D-function and its gradient to the stiffness matrix, strain-displacement matrix,  $[B]$  is split into two parts as  $[B] = [B_1] + [B_2]$ , such that  $[B_1]$  contains only derivatives of the shape functions while  $[B_2]$  contains derivatives of the D-function [42]-[44]. Away from the boundaries with specified boundary conditions,  $D_i$  is unity and therefore  $[B_2] = 0$  because the derivative of  $D_i$  are zero. Now the stiffness matrix can be expressed as

$$[K]_i = \int_{-\frac{h}{2}}^{\frac{h}{2}} \int_{A_i} ([B_1] + [B_2])^T [C] ([B_1] + [B_2]) dA_i dh \quad (5.12)$$

Expanding this expression, it can be seen that the stiffness matrix has the following three components.

$$[K]_i = [K_1] + ([K_2] + [K_2]^T) + [K_3] \quad (5.13)$$

$$[K_1] = \int_{-\frac{h}{2}}^{\frac{h}{2}} \left( \int_{A_i} [B_1]^T [C] [B_1] dA_i \right) dh \quad (5.14)$$

$$[K_2] = \int_{-\frac{h}{2}}^{\frac{h}{2}} \left( \int_{A_i} [B_1]^T [C] [B_2] dA_i + \int_{A_i} [B_2]^T [C] [B_1] dA_i \right) dh \quad (5.15)$$

$$[K_3] = \int_{-\frac{h}{2}}^{\frac{h}{2}} \left( \int_{A_i} [B_2]^T [C] [B_2] dA_i \right) dh \quad (5.16)$$

$[K_1]$  must be computed by sub-dividing the surface into triangles.  $[K_2]$  and  $[K_3]$  contain terms involving gradients of D-functions and zero everywhere except in the vicinity of boundaries that have essential boundary conditions specified. Using this fact the computation of  $[K_2]$  and  $[K_3]$  can be converted into line integrals along the boundary curves as shown below.

$$[K_2] = \sum_{j=1}^{n_i} \int_{-\frac{h}{2}}^{\frac{h}{2}} \int_{l_j} \int_{\phi} [B_1]^T [C] [B_2] \frac{1}{|\nabla \phi|} d\phi dl_j dh \quad (5.17)$$

In Eq. (5.17),  $n_i$  is the total number of line segments  $l_j$  used to represent the boundary curve within the element  $e$ . Similarly, the last term can be written as

$$[K_3] = \sum_{j=1}^{n_i} \int_{-\frac{h}{2}}^{\frac{h}{2}} \int_{l_j} \int_{\phi} [B_2]^T [C] [B_2] \frac{1}{|\nabla \phi|} d\phi dl_j dh \quad (5.18)$$

The boundary load terms are computed again by approximating the shell boundaries within each element as a set of line segments and evaluating the load integral along each line using Gauss quadrature as

$$\{f\} = \sum_{i=1}^{n_i} \int_{-\frac{h}{2}}^{\frac{h}{2}} \int_{l_i} \{N\}^T \{t\} d\Gamma dh \quad (5.19)$$

In Eq. (5.19),  $\{t\}$  is the traction acting on the boundary,  $l_i$  are the line segments and the shell thickness is  $h$ . Pressure loads and body forces require integration of the shell surface which must be approximated as triangles for integration purpose. For example, body force contribution is evaluated as

$$\{F^e\} = \int_{-\frac{h}{2}}^{\frac{h}{2}} \int_A \{N\}^T \{b\} dA dh \quad (5.20)$$

In Eq.(5.20), the body forces are evaluated as a combination of through thickness and area integrals. The integration over area is computed as a summation of the integration over triangles generated on the surface.

## 5. Results and Discussion

In this section, the 3D structures mesh approach to shell analysis is demonstrated using several examples and the results obtained by this approach has been referred to as IBFEM results. Quadratic B-splines have 27 nodes are referred to as IBFEM27N and cubic B-spline elements are IBFEM64N.

### Centrally Loaded Square Clamped Plate in Bending

A square plate as shown in Fig. 56 is loaded by a uniform pressure of 100 psi. The material used is structural steel. The problem description including dimensions and loads are shown in the figure. The plate is clamped along all its edges. Both the 64-node cubic B-spline elements and 27-node quadratic B-spline elements were used for the analysis and compare with results obtained using traditional shell elements implemented in commercial software (ABAQUS).

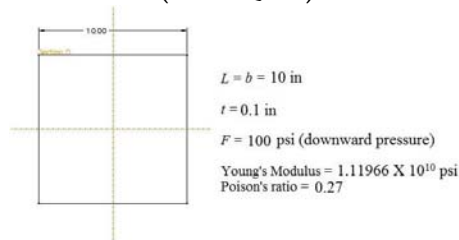


Fig. 56 Centrally loaded square plate

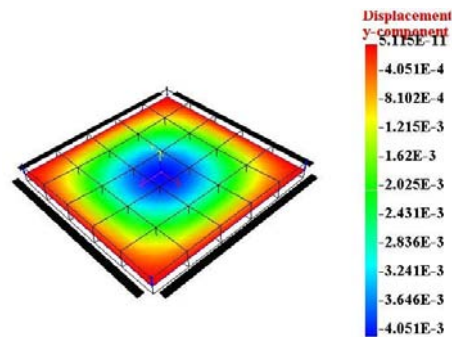
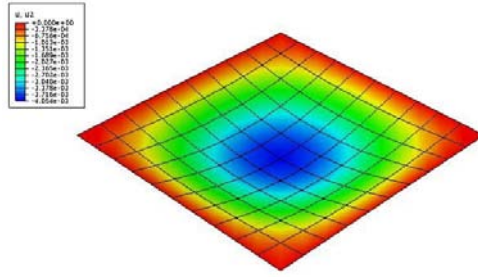


Fig. 57 IBFEM results (using cubic B-spline 64 node elements (5 x 5 Mesh))



**Fig. 58 Abaqus result using S4R (10 x 10 Mesh)**

**Table IV. Square plate: results for vertical displacement at the middle of the square plate, based on various meshes and element types**

Element type	Mesh	Max.Vertical displacement $\times 10^{-3}$ (in)
IBFEM 64N	2 x 2	3.562
	5 x 5	4.051
	10 x 10	4.055
IBFEM 27N	10 x 10	3.966
	20 x 20	4.043
	40 x 40	4.059
ABAQUS S4R	5 x 5	3.703
	10 x 10	4.054
	20 x 20	4.055

The results obtained using various elements are listed in table IV. Using traditional FEM shell elements (ABAQUS S4R elements), the maximum deflection at the center numerically converges to a value of  $4.055 \times 10^{-3}$  inch of vertical displacement at the middle of the square plate. The table shows that the results of IBFEM 64 node shell elements converge to the same answer with fewer number of elements. These elements use cubic polynomial representation of the solution and hence represent shear strains through thickness as parabolic and hence are able to represent the exact solution more closely. The quadratic 27 node B-spline shell elements require a much larger number of elements to reach the same solution.

### Micro Air Vehicle Wing design

The dimensions of the structure for this problem are shown in Fig. 59 . The wing is subjected to a normal pressure. One end is fixed to the fuselage while the side edges are free. The material properties, loads and constraints are shown in the figure. The thickness of the shell is 0.1 inch. Results computed using 64 node B-spline elements and traditional FEM (ABAQUS S8R5) are compared here.

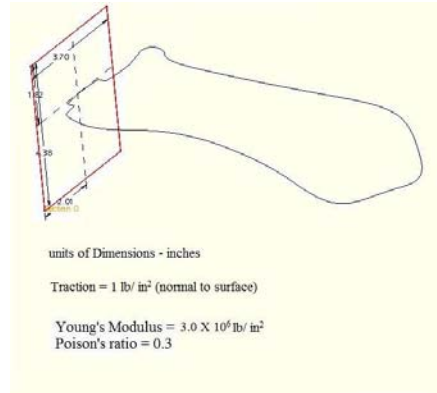


**Fig. 59 Micro air vehicle wing**

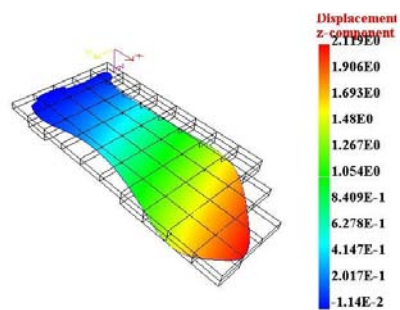


**Fig. 60 Displacement plot (IBFEM 64N) for micro air vehicle wing (10 x 5 Mesh)**

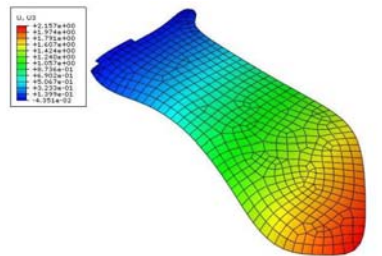


**Fig. 61 Displacement plot for micro air vehicle wing (ABAQUS S8R5, 542 elements)**

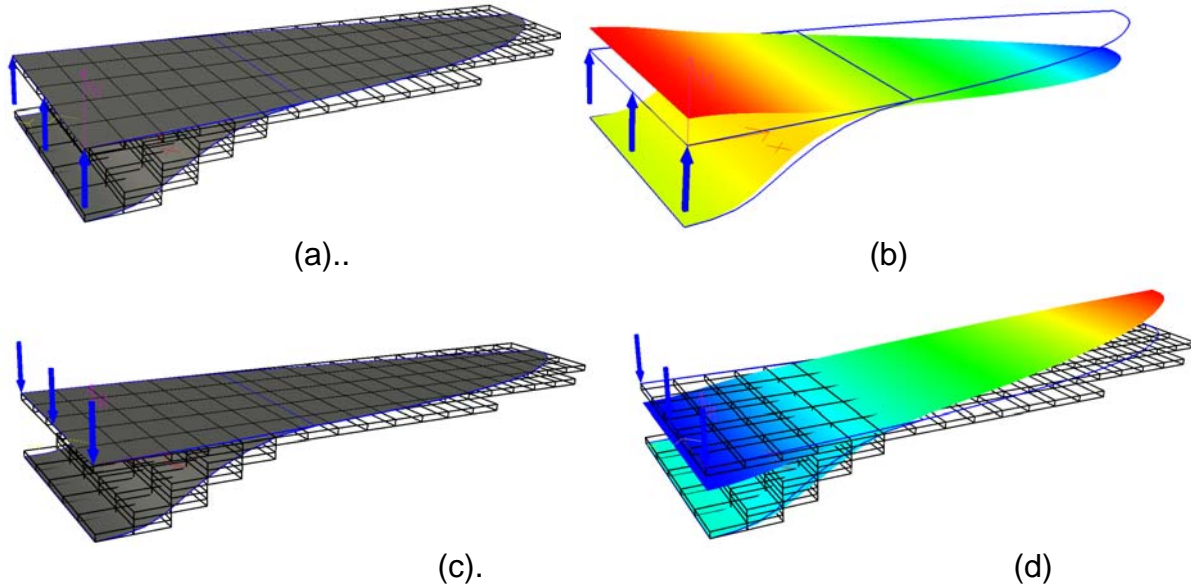
The figures show that the results of IBFEM shell elements the ABAQUS 8 node iso-parametric reduced integration elements are very close.

### Design of vibrating / oscillating wings for MAV

To design oscillating structures such as flapping wings it necessary to analyze the dynamics of structures. Modal analysis computes the natural frequencies and the mode shapes of vibration of a structure. New concepts for oscillating wing design were studied using modal analysis capability that was recently added to IBFEM software.

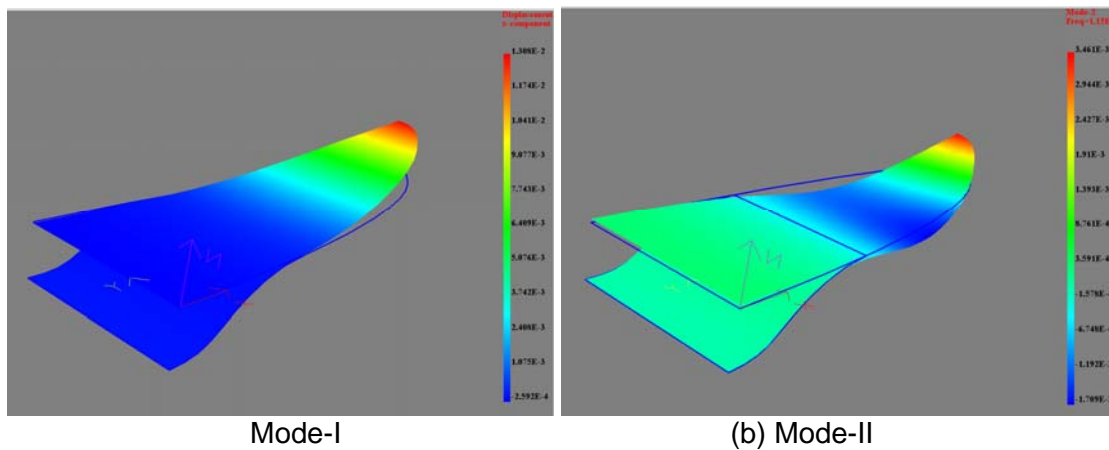
Fig. 62 shows a structural mechanism that can oscillate using internally applied forces generated using embedded electromagnetic actuators. The analysis was

performed using novel shell elements implemented in IBFEM software that can perform the analysis for relatively complex geometry without needing a conforming surface mesh. Fig. 62 (a) and (c) show the 3D grid and the applied forces that were used for the analysis. The deformed shape of the wing like geometry is shown in Fig. 62.



**Fig. 62 Oscillating structural mechanism**

The modes of vibration of this structure were computed to understand the shapes in which this structure can be made to vibrate or oscillate by inducing resonance. Fig. 63 shows the four modes of vibration of this structure.



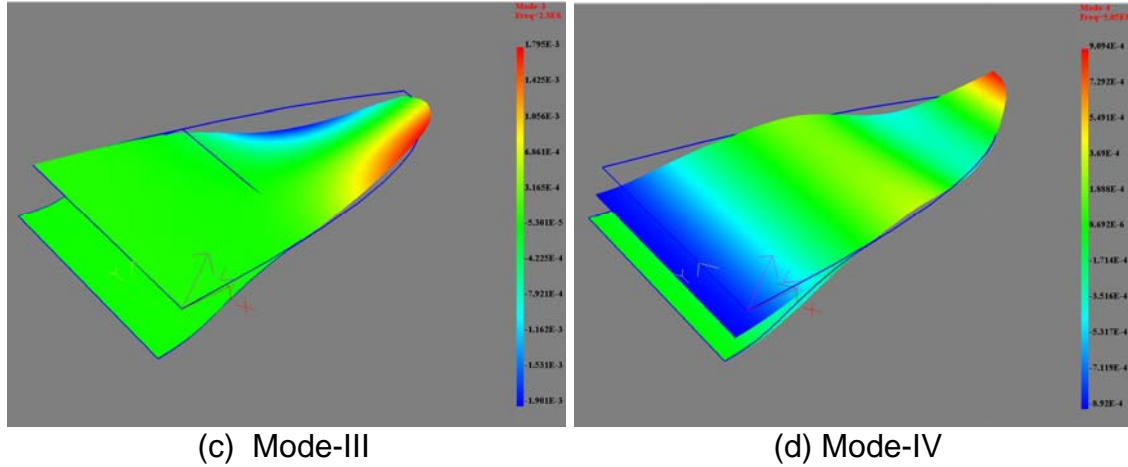


**Fig. 63 Mode shapes of vibration**

Modes I-, II and IV are similar to cantilever beam oscillations but Mode-III involves twisting. Clearly none of these modes are ideally suited for producing lift and thrust for flapping flight for MAVs. Therefore, the design challenge is to compute the right shape and reinforcement for the wing such that the first mode of vibration will produce a fanning action that produces thrust. This will be attempted in future designs using intuitive changes to the design. In future work, it is hoped that we will develop topology optimization techniques to compute appropriate reinforcements for a desired mode of vibration.

## 6. Discussion

Shell elements based on uniform B-spline shape function were studied and shown to be accurate when compared with traditional FEM shell elements implemented in commercial software. One of the key advantages of using these elements is that a structured mesh, which is easy generate automatically, can be used for the analysis. Moreover, the geometry is represented accurately using equations rather than approximated by the mesh. Implicit boundary method for applying boundary conditions is extended to shells. Both quadratic and cubic B-spline shape functions were tested and it was found that cubic elements provided very good results with fewer elements than quadratic elements. Computational cost is higher for these elements compared to traditional shell elements but often fewer elements are needed to get accurate results with cubic elements. The time taken to create the model is significantly lower because structured mesh generation is easily automated. Future work in this area includes extending these elements to non-linear applications involving large elastic deformation and elasto-plastic deformations. The performance of the IBFEM shell elements can be further improved by incorporating adaptive mesh refinement. The stress concentrations problems can be analyzed faster with adaptive mesh refinement.

The shell elements using IBFEM can also be extended to mixed solid-shell type analysis where thin shells are attached to solid structures.



## VI. DESIGN OF ACTUATORS FOR FLAPPING WING

### 1. Design criteria

In this chapter, IBFEM is used as an actuator design tool. Solenoid actuators with clapper armature or plunger armature and coil actuators are designed under given design criteria. The main application of interest is actuators for flapping wing micro- air vehicles. The micro air vehicles are small size aerial vehicles with a wing span of about 15 cm. For a micro air vehicle actuator, three main design criteria were used: coil winding area, iron weight and size.

To illustrate the analysis and design methodology using IBFEM, the process is demonstrated here using a set of assumed specification. An acceptable value for coil winding area  $S_w$  was assumed to be  $12mm^2$ . The entire coil winding area cannot be assumed to be only copper because the coil includes copper and other materials including insulator and air gaps. The relation between the coil winding area and the copper conductor is defined as the packing factor  $F_p$  [68]. When the coil is wound tightly, the packing factor can be up to 75% . Thus, the packing factor is assumed to be 70% . The area of the coil wire is  $S_c = 5.01 \times 10^{-3} mm^2$  when the number of the American Wire Gauge (AWG) is 40. Therefore, the number of coil turns  $N$  is given as following equation

$$N = \frac{F_p S_w}{S_c} = 1680 \quad (6.1)$$

When the coil is wound to a cylindrical bobbin with the diameter of 4 mm, the total length of the coil becomes about 21.1 m. As the resistance per meter for the given AWG is  $3.44 \Omega/m$ , the total resistance of the coil is approximately  $72 \Omega$ . In this research, it is assumed that the coil wire can allow current of 100mA to flow. The allowable current of the wire is based on plastic insulation. In case of the current source, LT3092, manufactured by Linear technology, the maximum output current is 200mA. The input voltage range is from 1.2 V to 40 V so that LT3092 can be operated by using a small size battery. Thus, the current of 100mA can be obtained using LT3092. If  $N=1680$  and the amount of current  $I$  can be controlled by a digital processor,  $NI$  (ampere-turns) can vary from 0 to 168.  $NI$  is also called magnetomotive force. In order to compare several designed actuators in the later section, the magnetomotive force,  $NI=30$ , is used. When the maximum current (100mA) flows in the coils, the coils can have maximum energy dissipation as  $W = I^2 R = 0.72 [W]$ .

Another design criterion is the iron weight of the actuator. The iron core contributes most to the weight of the actuator. Iron has high relative permeability so that using iron for the core of the actuator can intensify the magnetic force of the actuator. Therefore, there is a trade-off between the iron weight of the actuator and the usage of the iron. As the second design criterion, we assume that the total iron weight can be up to 10g. In order to compute the iron weight of an actuator design, the mass density of iron is assumed to be  $7874 \text{ kg/m}^3 = 7.874 \times 10^{-3} \text{ g/mm}^3$ . The third design criterion is the size of the actuator. In order to install an actuator inside the micro air vehicle, we have assumed that the actuator should fit inside of a cube with edge length of 2cm.

Here we first compare several actuator designs by computing the force generation capacity using the magneto-elastostatic analysis capability implemented in IBFEM. Both solenoid type actuators and coil actuators were studied.

## 2. Solenoid actuators with clapper armature

A solenoid actuator with a clapper armature is shown in Fig. 64. The clapper armature can move in the y-direction when the coils carry current. The armature and the stator are made of thin steel laminations with relative permeability of 2000, a thin steel lamination that can reduce heating caused by eddy current. When the current flows through a coil, magnetic flux is created as shown in Fig. 64. The magnetic flux follows a closed path. If the magnitude of the magnetic flux is known, a magnetic force can be estimated using the Maxwell stress tensor method.

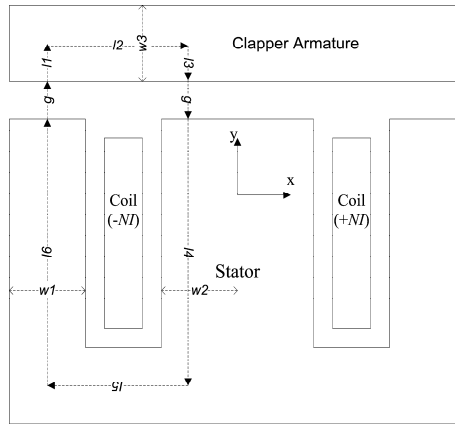


**Fig. 64 Solenoid actuator with clapper armature**

We assume the dimensions are  $l1 = l3 = 0.5 \text{ mm}$ ,  $l2 = l5 = 3 \text{ mm}$ ,  $l4 = l6 = 6.5 \text{ mm}$ ,  $g = 1 \text{ mm}$ , and  $w1 = w2 = w3 = 1 \text{ mm}$ . Using the reluctance method, the magnetic in the air gap is estimated to be approximately  $\phi = 6.285 \times 10^{-7} \times NI [\text{Wb}]$ . Using this estimate, the

magnetic flux density and the magnetic field density is  $B_{gap} = 6.285 \times 10^{-4} \times NI$  [T] and  $H_{gap} = 500 \times NI$  [A/m]

Using Maxwell's stress tensor method, the normal magnetic pressure can be obtained as

$$F = \frac{\mu_0}{2} (H_{gap})^2 (4 \times w_1) = 6.283 \times 10^{-4} \times (NI)^2 \text{ [N]} \quad (6.2)$$

When  $NI = 30$ , the magnetic force per unit length becomes 0.565 N/m. The magnetic flux and the magnetic field density are  $1.886 \times 10^{-2}$  [T] and  $1.5 \times 10^4$  [A/m]. Using the same geometry of the actuator, Fig. 65 (A) shows contour plot of magnetic vector potential computed using IBFEM. Fig. 65 (B) shows magnetic field density in the y-direction. The computed magnetic field density in the gap is approximately equal to the analytical value of  $1.5 \times 10^4$  [A/m]. For this analysis, the asymptotic boundary conditions are applied on the outer boundaries. The computed force is 0.633 N/m. The computed force and the analytical solution are quite close. The difference between them results from a fringing flux, which the reluctance method ignores. As the iron domain is  $40\text{mm}^2$ , the iron weight per unit depth is  $0.315\text{g/mm}$ .

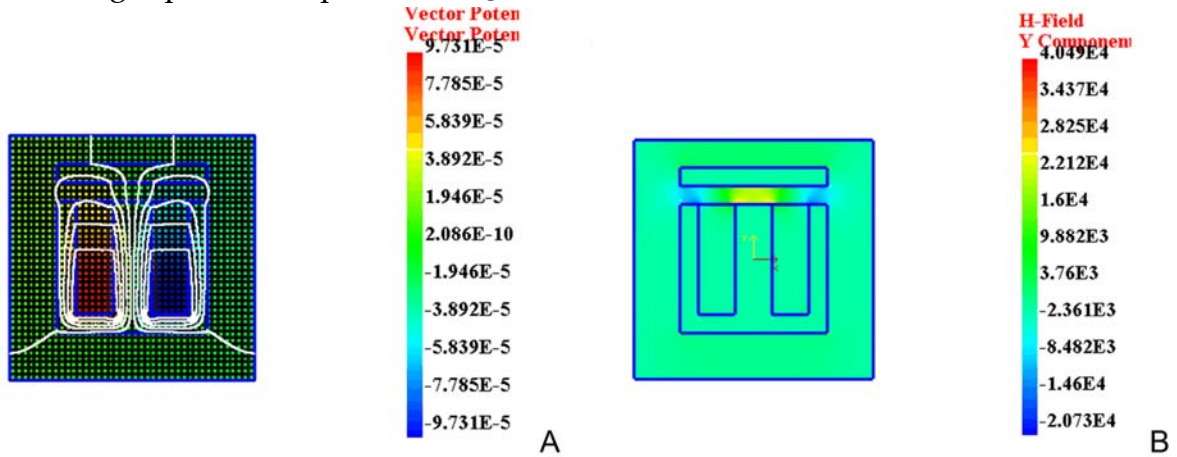


**Fig. 65 Computed results using IBFEM. A) Contour plot of magnetic vector potential, and B) Magnetic field density**

Based on the initial design shown in Fig. 64, three different designs are created by changing the geometry of the armature and the stator. Fig. 66 shows three designs with dimensions. The dimensions shown are all in  $\text{mm}$ . Even though the geometry is different for each actuator, same mesh densities was used in the structured mesh created for all the three designs. Nine node B-spline elements were used for the analysis. The total number of nodes was 2586. The asymptotic boundary conditions were applied on the outer boundaries. The magnetomotive force,  $NI = 30$ , was applied.

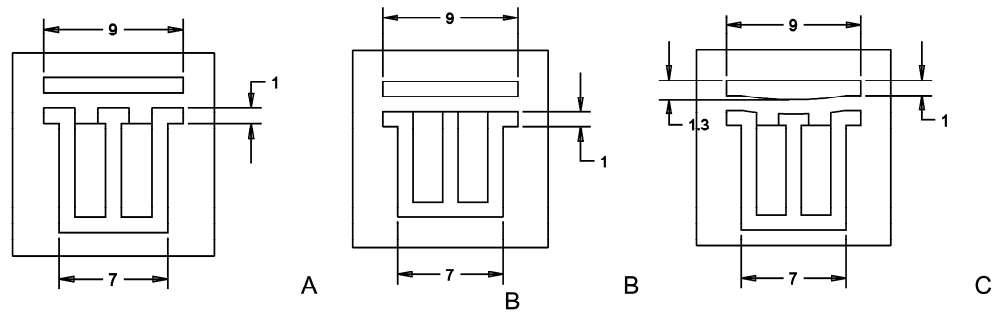


**Fig. 66 Clapper solenoid actuators. A) Design 1, B) Design 2, and C) Design 3**

Fig. 67 shows contour plots of magnetic vector potentials for all designs. Based on those computations, Table V shows comparison between the three designs in terms of the magnetic force and the iron weight.

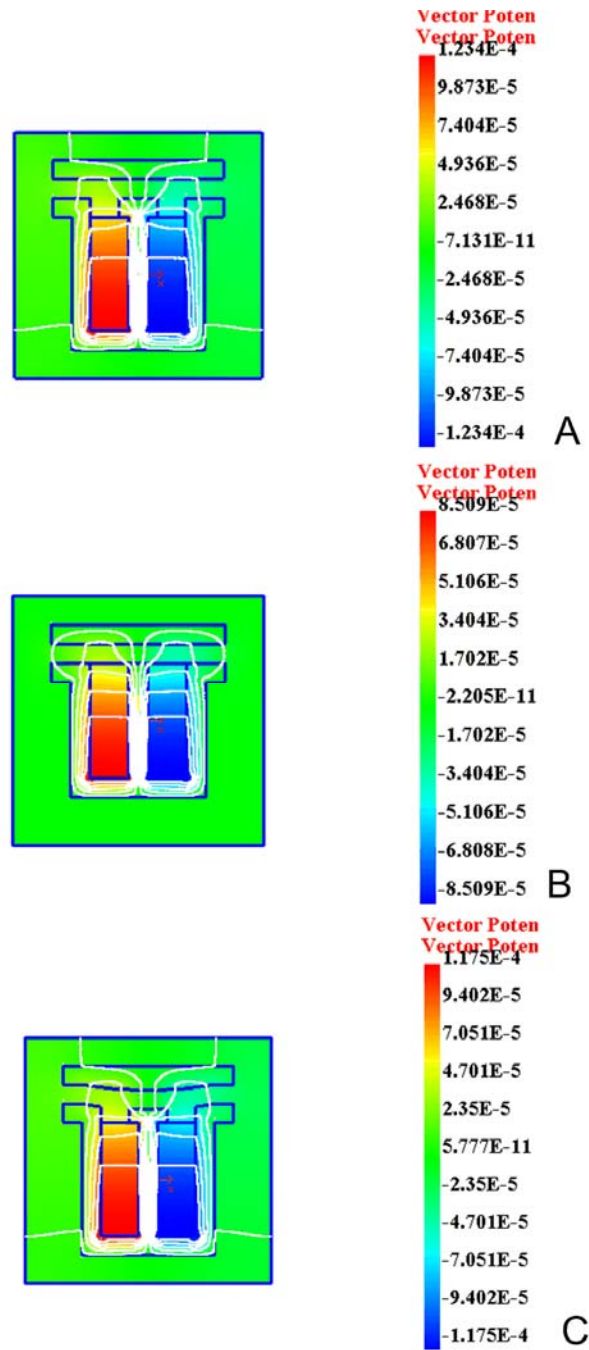


Fig. 67 Contour plots of magnetic vector potential for clapper solenoid actuators. A) Design 1, B) Design 2, and C) Design 3

Table V. Comparison for three clapper solenoid actuators ( $Nl=30$ )

	Design 1	Design 2	Design 3
Force per $m$	0.691 $N/m$	0.509 $N/m$	0.681 $N/mm$
Iron weight per $mm$	0.315 $g/mm$	0.283 $g/mm$	0.320 $g/mm$

According to Table V, the first actuator design produces the largest force among them. The second actuator is the lightest one.

### 3. Solenoid actuators with plunger armature

A solenoid actuator with a plunger armature is shown in Fig. 68 . The shape of the plunger armature can be a brick, cylinder, or conics. There are two gaps of  $g$  and  $g_s$  that the flux can enter and leave the plunger armature. Useful magnetic force is produced only at  $g$ .

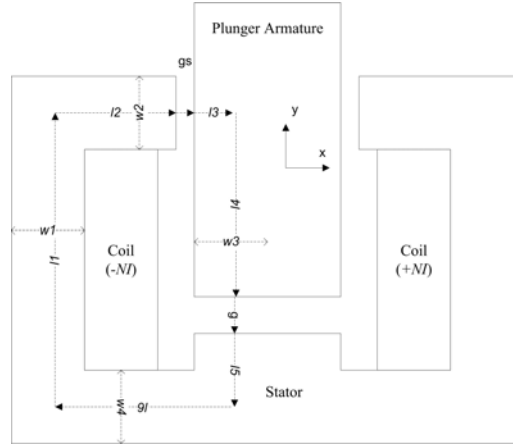


**Fig. 68 Solenoid actuator with plunger armature**

The armature and the stator are made of steel with the relative permeability of 2000. The dimensions are  $l1 = 7mm$  ,  $l2 = 2.5mm$  ,  $l3 = 0.9mm$  ,  $l4 = 4.5mm$  ,  $l5 = 1.5mm$  ,  $l6 = 3.5mm$  ,  $gs = 0.1mm$  ,  $g = 1mm$  and  $w1 = w2 = w3 = w4 = 1mm$  . Using the reluctance method, the magnetic flux is  $\phi = 1.132 \times 10^{-6} \times NI$  [Wb]. Based on the magnetic flux, the magnetic flux density and the magnetic field density in each air gap can be computed as follow  $B_{gap} = 1.132 \times 10^{-3} \times NI$  [T] and  $H_{gap} = \frac{1}{\mu_0} B_{gap} = 900.8 \times NI$  [A/m]. Using the magnetic

field in the gap, the useful magnetic force can be calculated as follow. When  $NI = 30$ , the force becomes 0.918 N. The magnetic flux and the magnetic field density are  $3.4 \times 10^{-2}$  [T] and  $2.702 \times 10^4$  [A/m]. Fig. 69 shows the computed results: contour plot of magnetic vector potential and magnetic field density in the y-direction. For the analysis, the same mesh density was used in the clapper solenoid actuator model. Nine node B-spline elements were used. Asymptotic boundary conditions were applied on the outer boundaries. The computed total force on the plunger armature is 0.9130 N/m. As the total area of the iron is  $38.8mm^2$  , the iron weight per unit depth is  $0.306g/mm$  .

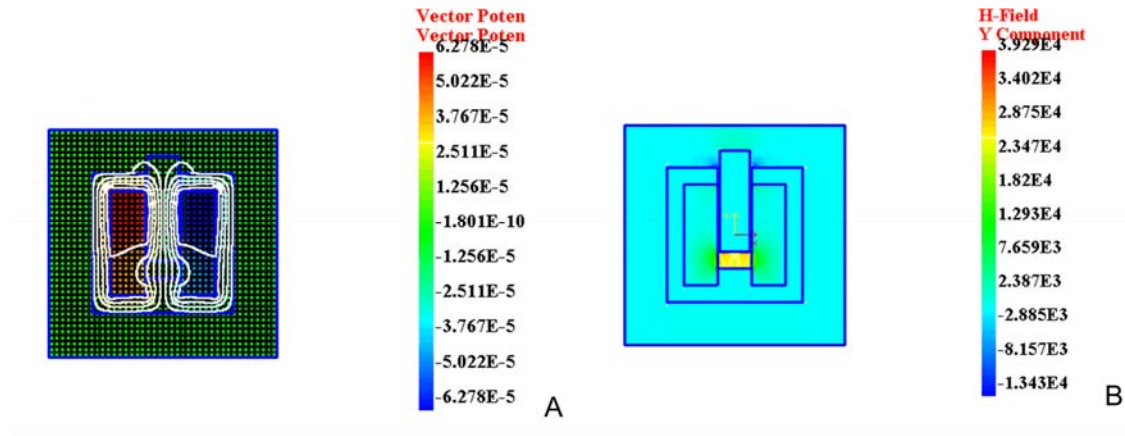


**Fig. 69** Computed results using IBFEM. A) Contour plot of magnetic vector potential, and B) Magnetic field in the y-direction

Modifying the initial design in shown in , three different designs are created as shown in Fig. 70 . The dimensions shown are all in *mm*. For all designs, the area of the 2D model is as same as one of the clapper solenoid actuator. Nine node B-spline elements were used for the analysis. The total number of nodes was 2548. The asymptotic boundary conditions were applied on the outer boundaries. The magnetomotive force,  $NI = 30$ , was used.

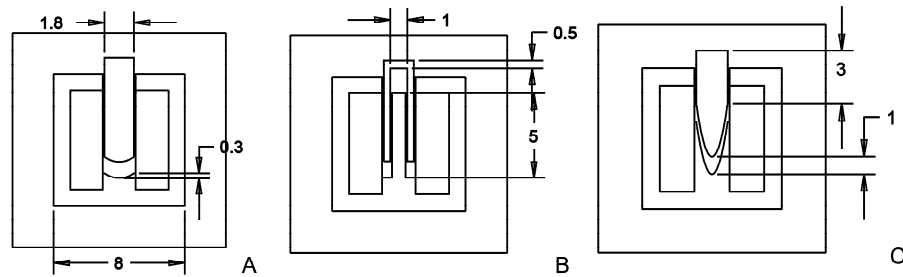


**Fig. 70** Plunger solenoid actuators. A) Design 1, B) Design 2, and C) Design 3

Fig. 71 shows contour plots of magnetic vector potentials for all designs. Based on those results, Table VI shows comparison for three designs in terms of the magnetic force and the iron weight.

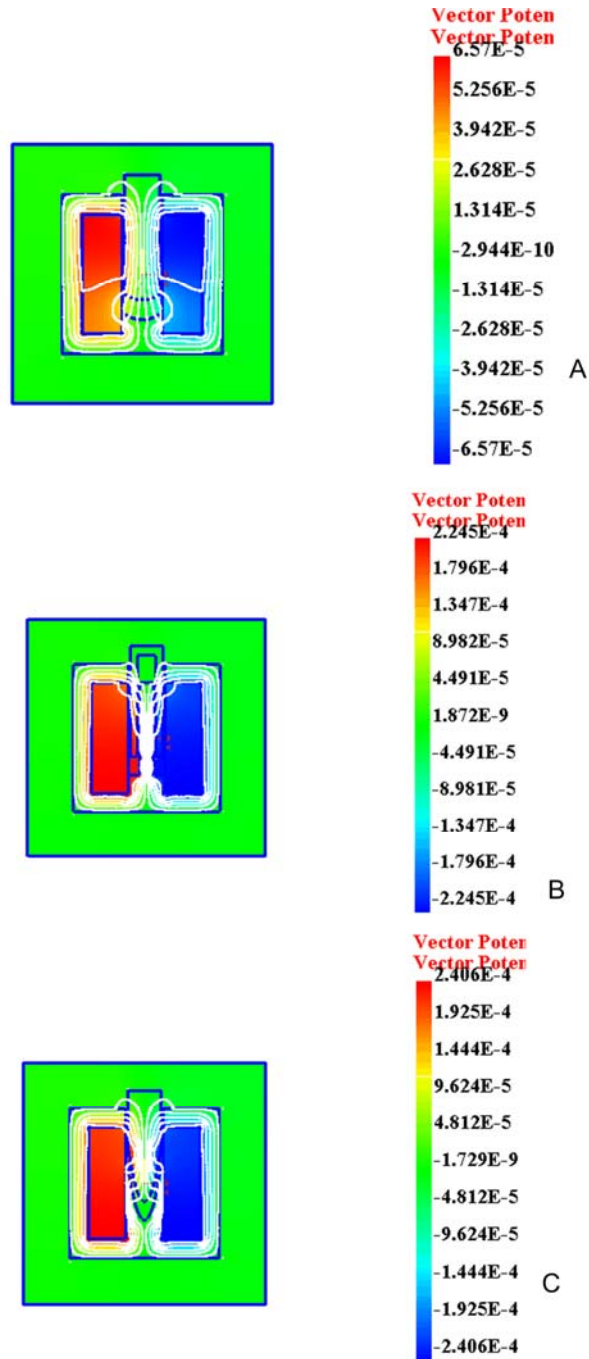


Fig. 71 Contour plots of magnetic vector potential for plunger solenoid actuators. A) Design 1, B) Design 2, and C) Design 3.

Table VI. Comparison for three plunger solenoid actuators ( $N=30$ )

	Design 1	Design 2	Design 3
Force per $m$	1.154 $N/m$	0.262 $N/m$	2.801 $N/mm$
Iron weight per $mm$	0.306 $g/mm$	0.294 $g/mm$	0.310 $g/mm$

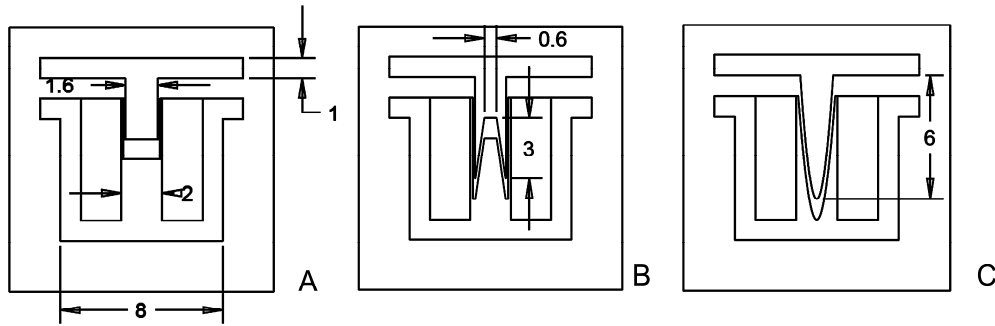


According to Table VI, the third plunger solenoid actuator model can produce the largest force among them. The second actuator model is the lightest one.

#### 4. Solenoid actuators with a combined plunger & clapper armature

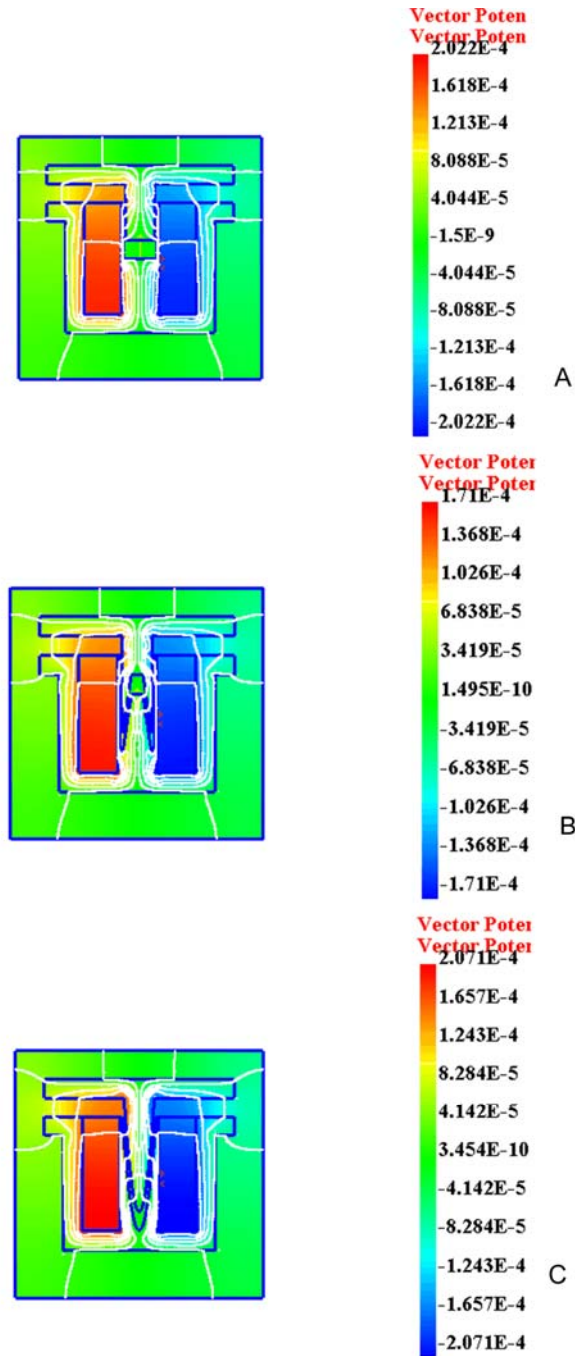
A combined plunger & clapper armature is an armature that includes a clapper & plunger to increase the force. Three designs were studied. The sizes of those actuators are similar to one of the clapper solenoid actuator in the previous section. Magnetic force and iron weight for each actuator are characterized.

Fig. 72 shows three solenoid actuators with a mixture armature. The dimensions shown are all in *mm*. For all designs, the area of the 2D model is as same as one of the clapper solenoid actuator. For the analysis, the same mesh density is applied for all the designs. Nine node B-spline elements were used for the analysis. The total number of nodes was 2674. The asymptotic boundary conditions were applied on the outer boundaries. The magnetomotive force  $NI$  is equal to 30.



**Fig. 72 Three combined plunger & clapper solenoid actuators. A) Design 1, B) Design 2, and C) Design 3**

Contour plots of magnetic vector potentials are shown in Fig. 73. Based on those results, Table VII shows comparison for three designs in terms of the magnetic force and the iron weight.



**Fig. 73** Contour plots of magnetic vector potential for combined plunger & clapper solenoid actuators. A) Design 1, B) Design 2, and C) Design 3.

**Table VII. Comparison for three combined plunger & clapper solenoid actuators ( $NI=30$ )**

	Design 1	Design 2	Design 3
Magnetic force per	0.961 N/m	0.413 N/m	1.30 N/m

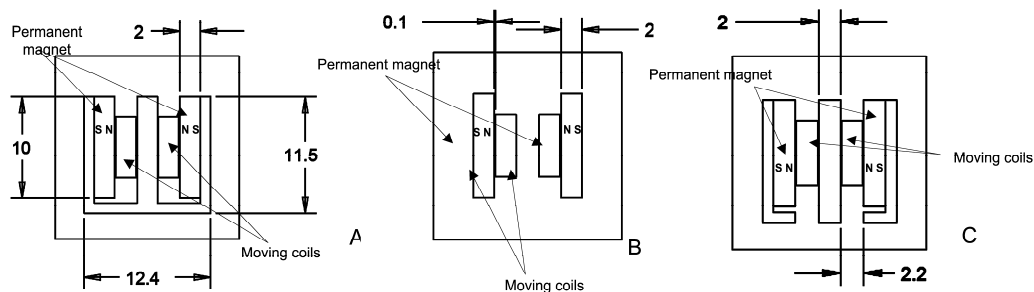
<i>m</i>			
Iron weight per <i>mm</i>	0.342 <i>g / mm</i>	0.339 <i>g / mm</i>	0.340 <i>g / mm</i>

According to Table VII, the third one can produce the largest force among them. The second actuator is the lightest one.

## 5. Coil actuators

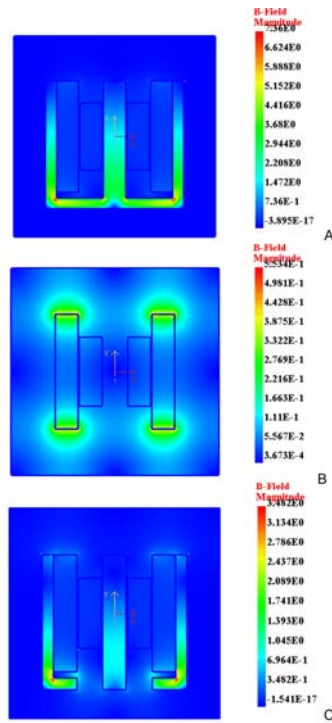
In this section, three coil actuators are studied under the given design criteria. The coil actuators include permanent magnets so that higher magnetic flux can be produced without current flowing through the actuator resulting in heating losses. The coil actuator has magnetic force in the conductive coil instead of one on the armature of the solenoid actuator, a magnetic force that is computed using the Lorentz force equation.

Fig. 74 shows three coil actuators. The dimensions shown are all in *mm*. For all the designs, the rectangular area of the 2D model including the air domain is  $18 \times 18 \text{ mm}^2$ . The coil winding area is the same as in previous solenoid actuators. Two permanent magnets have different direction with the same remanent flux of 0.8 T. The first design is based on a typical voice coil actuator in a loudspeaker. The second is a design to remove the iron laminates from the first design. The third design has a gap at the bottom portion of the iron laminate, which allows the coil to move freely in the downward direction. For the analysis, the same mesh density is applied for all designs. Four node bilinear elements were used. The total number of nodes was 12036. The asymptotic boundary conditions were applied on the outer boundaries. *NI* is equal to 30.



**Fig. 74** Three coil actuators. A) Design 1, B) Design 2, and C) Design 3

The magnitudes of the magnetic flux densities are shown in Fig. 75. As the Lorentz force is proportional to the magnetic flux density, a stronger magnetic flux density near the moving coils can create a larger force. The first design has the strongest magnetic flux near the moving coils. Based on those results, Table VIII shows comparison for three designs in terms of the Lorentz force on the moving coil and the iron weight of the actuator.



**Fig. 75** Magnitude of B fields for three coil actuators. A) Design 1, B) Design 2, and C) Design 3.

**Table VIII. Comparison for coil actuators ( $N=30$ )**

	Design 1	Design 2	Design 3
Force per $m$	21.0 $N/m$	2.64 $N/m$	9.12 $N/m$
Iron weight per $mm$	0.428 $g/mm$	0 $g/mm$	0.394 $g/mm$

According to Table VIII, the first coil actuator can produce the largest force among them. The second design is the best design if the actuator weight is the most critical criterion.

## 6. The best actuator among the designed actuators

Using IBFEM, four types of actuators were examined such as the clapper solenoid actuator, the plunger solenoid actuator, the combined plunger & clapper solenoid actuator, and the coil actuator. Among them, the coil actuator is the best actuator considering the given design criteria. Among several designs for the coil actuators, the first design is used for flapping wings of the micro air vehicle as shown in Fig. 76. Coil actuators have several advantages over the solenoid actuators that were studied. The most important being the force direction can be reversed by changing the direction of current. The magnitude does not vary due to the deformation or movement of the coil as long as the coil is within the uniform field created by the magnets.

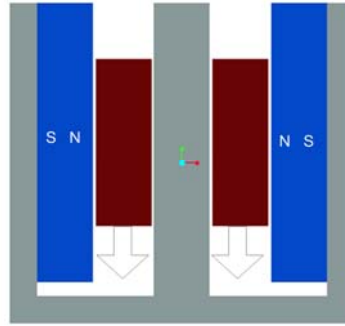


**Fig. 76 The best magnetic actuator among several designed actuators**

This coil actuator ideas was further tested using 3D model as shown in Fig. 77 . Considering the symmetry, one fourth of the actuator was modeled. The geometry was modeled using commercial software, Pro/engineering. Fig. 78 shows the dimension of the 3D coil actuator and the orientation of the permanent magnets. The dimensions shown are all in *mm*.

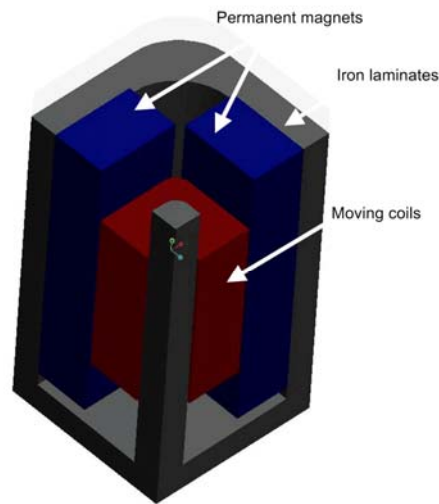


**Fig. 77 Solid model of the 3D coil actuator**

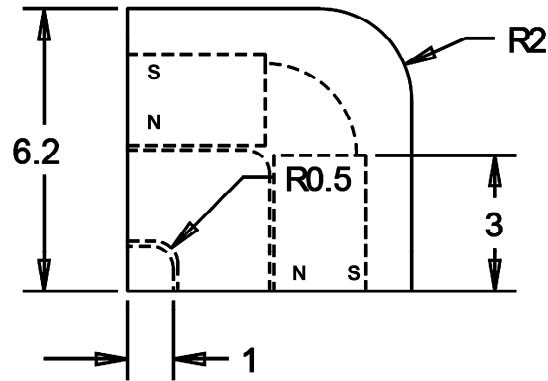


**Fig. 78 The top view of the 3D coil actuator**

The moving coils carry current, coils that has a conductivity values of  $10^6$  S/m. In order to perform the analysis, eight node brick elements were used. The total number of the nodes was 9651. According to the design criterion, the magnetomotive force,  $NI$ , can vary from 0 to 168. When  $NI$  is equal to 30, the magnetic flux density of the coil actuator is shown in Fig. 79 .

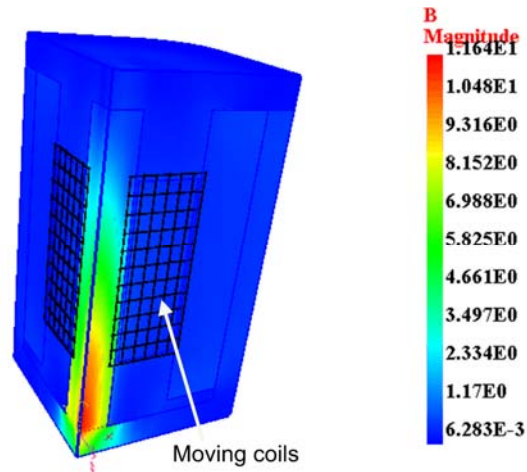


**Fig. 79 The magnitude of the magnetic flux density of the coil actuator**

The magnetic flux density,  $B$ , vary from 1.17 to 2.33 T nearby the moving coils, so the computed force is -0.114 N. When  $NI$  is equal to 10, 30, 60, 90, 120 or 168, the computed Lorentz forces are plotted in Fig. 80 . This figures shows the linear relation between the magnetomotive force and the Lorentz force. The maximum force is 0.683 N.

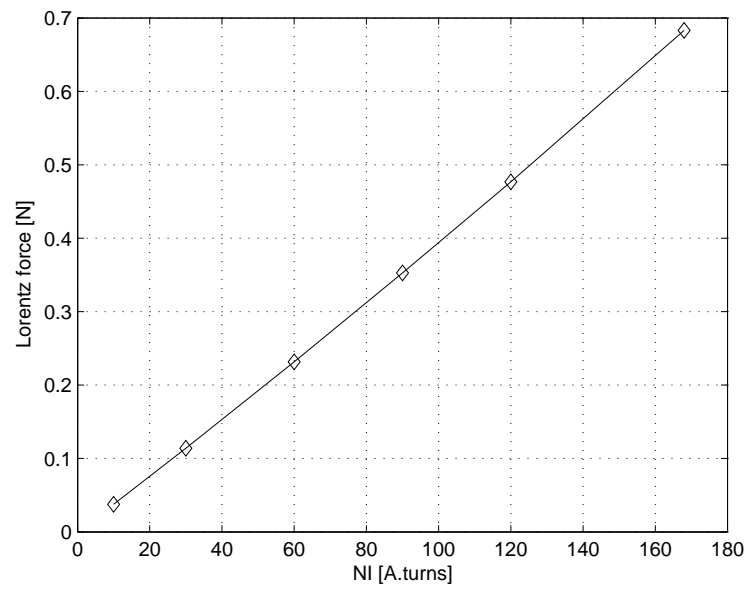


**Fig. 80 Lorentz force of the coil actuator versus NI**

## 7. Coupled magneto-elastostatic analysis of flapping wing actuation

The best coil actuator is embedded in a micro air vehicle with flapping wings as shown in Fig. 81 . The coil actuator can fit inside of the fuselage. The moving coil of the coil actuator is attached to the structure or could even be built-into the structure.

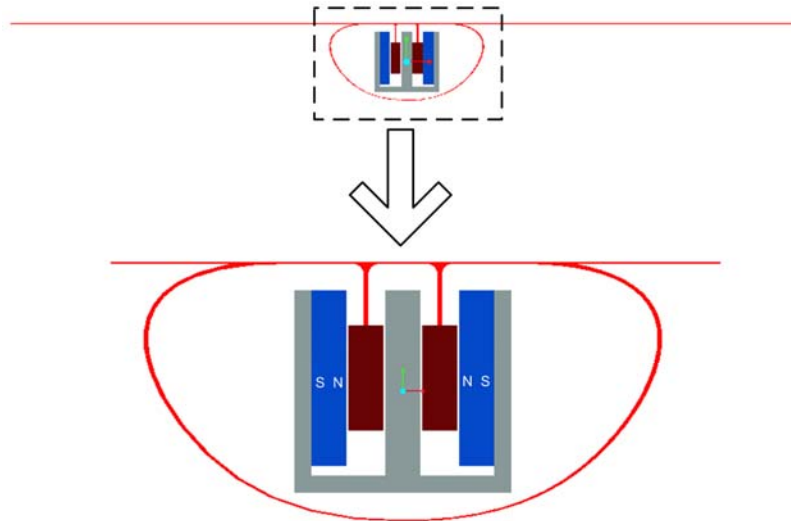


**Fig. 81 The coil actuator with flapping wings**

Four different structure supports for the wing were designed as shown in Fig. 82 . The structures are modeled as shells and surface models as shown in Fig. 83 used represent their geometry. The thickness of the shell-like structure is assumed to be equal to 0.45mm. All the designs have a similar top view; however, they have different front and side views. The dimensions shown are all in mm. As the length in chordwise direction is 26 mm, two coil actuators can be placed along the chordwise direction because the width of the coil actuator is 12.2mm.

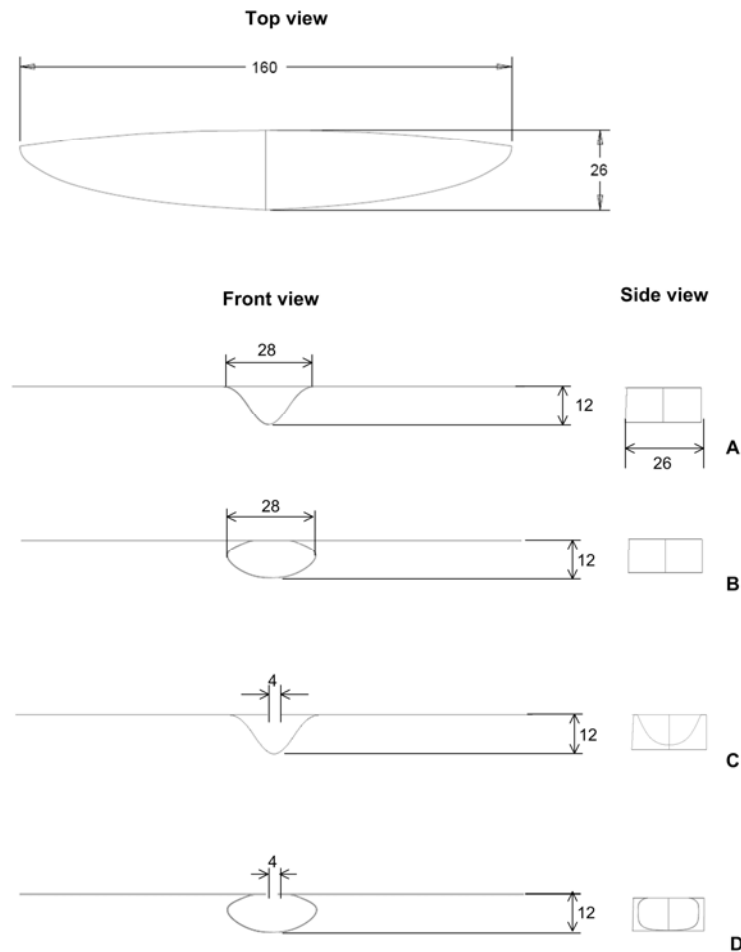


**Fig. 82** Four structures with flapping wings. A) Design 1, B) Design 2, C) Design 3, and D) Design 4.





**Fig. 83 Four surface structures with flapping wings. A) Design 1, B) Design 2, C) Design 3, and D) Design 4.**

In order to perform analysis of thin shell-like structures, IBFEM shell elements described in the previous chapter were used. The total number of nodes in model is 666. Considering the symmetry of the geometry, half of the structure was modeled for the analysis. The structured mesh and the boundary conditions are shown in Fig. 84 . The magnetic force acts downward so that the wing undergoes an upstroke. When one coil actuator is used, the applied force varies from 0 to 0.342 N at the edge. Using two coil actuators, the magnetic force can be double.

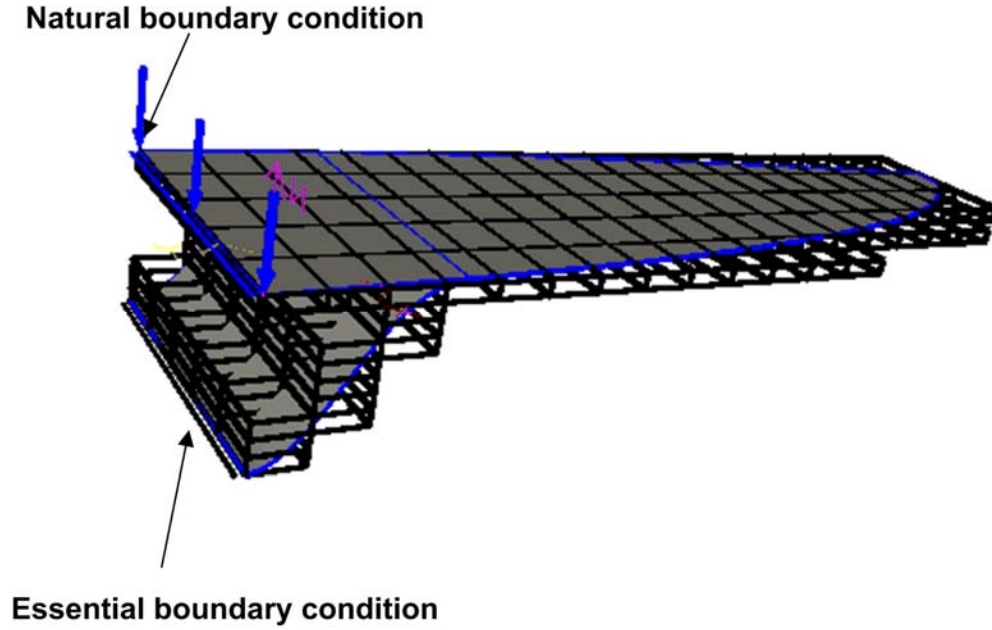


**Fig. 84      Structured mesh and boundary conditions of the first design**

By reversing current direction, force can be reversed so that the wing can undergo a down-stroke. Using the coil actuator, the same amount of Lorentz force can be produced in the opposite direction by changing the direction of the current. When  $NI$  is equal to 30, the wing up-strokes and down-strokes of the four designs are shown in Fig. 85 . For the up-stroke, the maximum displacement on the tip is  $2.633 \times 10^{-3} \text{ mm}$  in the first design,  $4.238 \times 10^{-3} \text{ mm}$  in the second design,  $3.765 \times 10^{-2} \text{ mm}$  in the third design, and  $1.968 \times 10^{-1} \text{ mm}$  in the fourth design. Magnitudes of the tip deflections during the wing up-stroke are the same as ones during the wing down-stroke because the magnetic force is proportional to the displacement. Thus, the tip deflection can be double including both strokes. Among the four designs studied here, the last design produces the largest tip deflection.

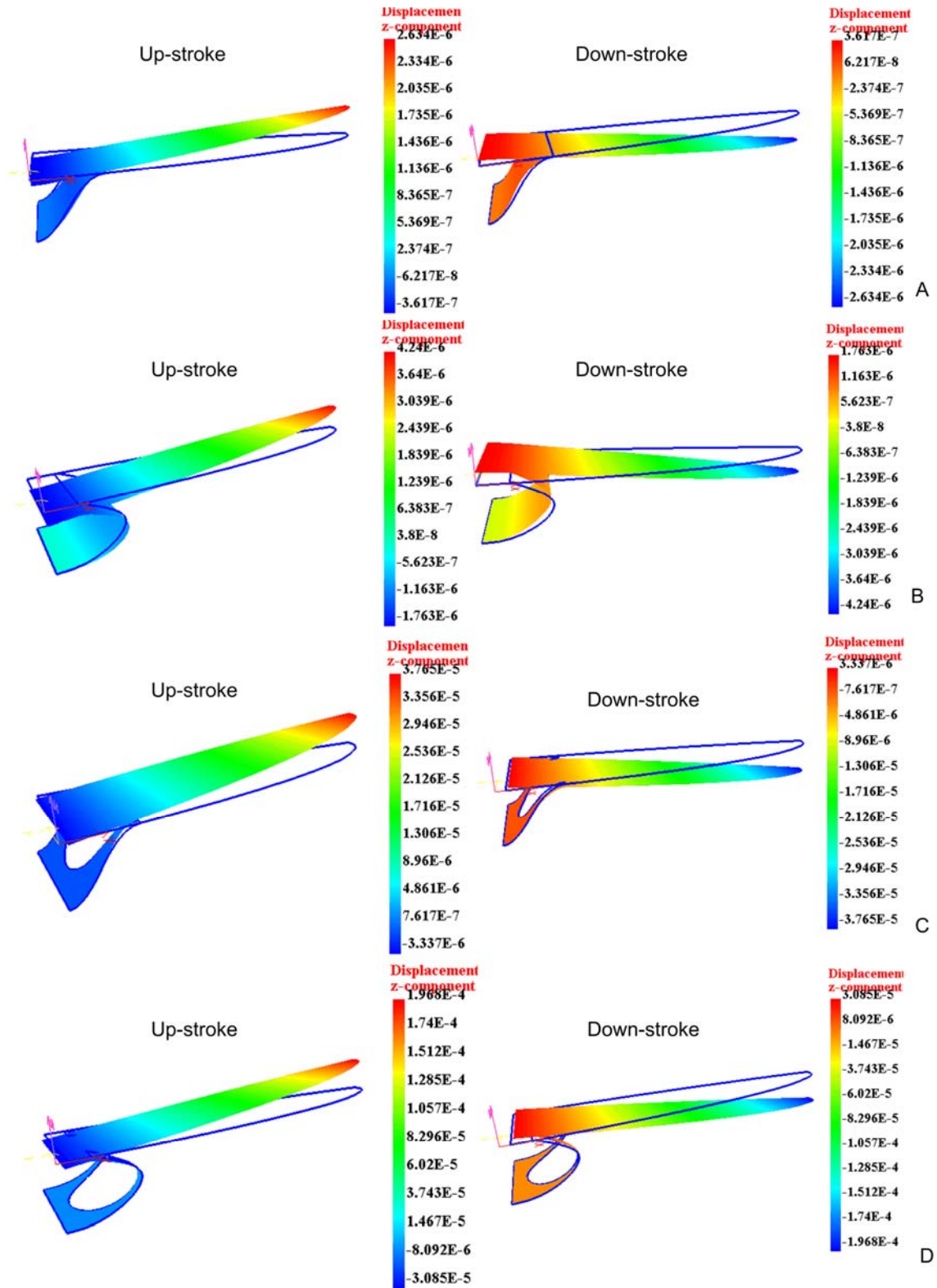
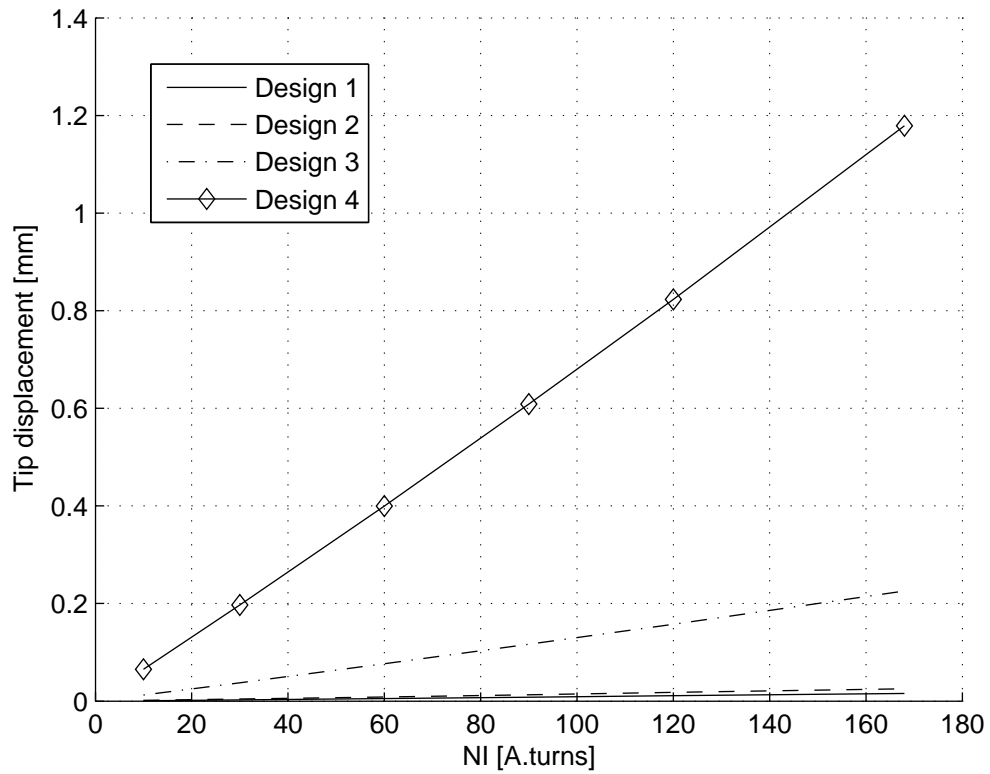


Fig. 85 Displacement in the z-direction during the wing stroke. A) Design 1, B) Design 2, C) Design 3, and D) Design 4.

When  $NI$  varies from 1 to 168, the tip deflection as a function of the magnetomotive force is shown in Fig. 85 . The first three designs are too stiff for our application.



**Fig. 86** Tip displacement versus NI for wing upstroke

## VII. CONCLUSIONS AND FUTURE RESEARCH DIRECTION

### 1. Summary

The goal of this project was to explore means of designing multi-functional composite structures that have sensing and actuation capabilities. Both sensing and actuation means were studied. Computational tools were created that help in designing and analyzing magnetically actuated composite structures. A brief summary of each of these activities is given below.

#### **Composite sensors:**

A method for detecting load application and damage in composite structures by determining change in resistivity/conductivity was studied. An algorithm for solving inverse problem to determine average resistivity values in composite structures was demonstrated. The method can use data from an arbitrarily large number of electrodes to compute average values of resistivity or conductivity for the structure. Finite element models for the structure are used to solve the forward problem, making this method very general and applicable to arbitrary shaped structures. Ideally, the electrodes should be embedded in the structures during the manufacturing process itself so that it can be used for quality control, detection of defects as well as subsequent health monitoring. One of the advantages of measuring resistivity is that damage can be detected even in structures that were not tested during manufacturing. Damage can be detected for structures that are in use by attaching electrodes on the surface, determining the average resistivity and comparing it to values associated with undamaged material. The main source of error in this approach arises from inaccuracy in the geometric models of the structure and the electrodes. Random noise added to the voltage data used in numerical validation indicates that any error in the voltage data can get amplified due to difficulties in numerical convergence. In principle, a similar inverse approach can also be used to determine applied loads on the structure. Experimental studies indicate that this may be difficult because the changes in the electrode voltage due to strains are very small. Even with amplification, the data is hard to use because of significant non-linearity in the observed behavior. However, the approach we developed is promising for detecting damages or defects because they cause significant changes in resistivity and is therefore easier to detect. Further study is needed to explore ways of determining applied loads and strains.

## **Magnetically actuated composite structures**

The idea of using magnetic forces to actuate structural mechanisms was studied. The main application of interest is micro air vehicle wings that are shell like structures. Topology optimization method was studied as a potential method for designing structures that have specified modes of deformation. The structure is then to actuated using magnetic actuation means built into or around the structures. Several actuators were studied including solenoid actuators and coil actuators. After systematic comparison of several designs, it was concluded that a coil actuator built into composite structures is an ideal means for actuation of composite structures. A conceptual design of a flapping wing vehicle was developed that is designed to actuate by built in actuation capability of the body, wing and support structures. No external mechanisms, motors or linkages are needed.

## **Computational tools for designing magnetically actuated structures**

Computational tools were developed to design and analyze structures actuated by magnetic forces. Magnetostatic analysis capability was implemented into a pre-existing software (named IBFEM) developed at the University of Florida that can perform finite element analysis without the need for generating mesh. Solid and surface geometry modeled on commercial CAD software can be imported into this software and analysis can be performed without approximating the geometry using a conforming mesh. The structured mesh approach has been demonstrated to work for magnetostatic analysis and validated using several examples with known solutions. The approach has been demonstrated for both 2D and 3D magnetostatic models. Structured mesh is easy to generate and the elements are regular and not distorted as in traditional finite element mesh. Magnetic forces were computed by integrating the magnetic force density. These forces and then used in a subsequent structural analysis to determine the deflection of the structure. Shell elements based on uniform B-spline shape function were implemented into IBFEM. One of the key advantages of using these elements is that a structured mesh, which is easy generate automatically, can be used for the analysis. Both quadratic and cubic B-spline shape functions were tested and it was found that cubic elements provided very good results with fewer elements than quadratic elements. Computational cost is higher for these elements compared to traditional shell elements but often fewer elements are needed to get accurate results with cubic elements. The time taken to create the model is significantly lower because structured mesh generation is easily automated.

## **2. Future work**

Design methodology developed here based on topology optimization can be extended to design structures that morph or oscillate in specified modes. This would

allow us to design wings that are designed to oscillate in a mode shape that produces the most lift and thrust. High speed photography has been used to study motion of insect and bird wings by biologists. It is challenging to design wings that can oscillate in a fashion that mimics the flapping of insect or bird wings. Preliminary results obtained using topology optimization in this research suggests that this is a promising area for further study but it is a challenging problem that may take 2-3 years of work especially if we also want to create physical models for validation. In order to fully understand the interaction of flapping wings with air, fluid structure interaction model are needed. Incorporating CFD into IBFEM software would make simulation and analysis of such systems much easier than currently available tools.

The magnetostatic analysis capability that was developed in this research needs to be extended in the future to nonlinear problems as well as dynamics problems. Since 3D analysis is computationally expensive, it is not always desirable to use a uniform mesh everywhere. Mesh refinement techniques are needed that locally refines the mesh while still using a structured mesh that has regular shaped elements. Development of such local refinement techniques is part of the future work needed to make 3D magnetostatic analysis less expensive. For application to structural mechanisms undergoing large deformation, the shell elements must be extended to allow large elastic deformation and elasto-plastic deformations. The performance of the IBFEM shell elements can also be further improved by incorporating adaptive mesh refinement. The shell elements using IBFEM can also be extended to mixed solid-shell type analysis where thin shells are attached to solid structures.

This research focused on the steady static analysis so that the coupled problem is modeled as a weakly coupled magneto-elastostatic analysis. This assumption allows us to perform the magnetostatic and elastostatic analysis sequentially. If the magnetic field changes due to the elastic deformation, the problem becomes nonlinear and a strongly coupled nonlinear analysis is needed. The magnetic field may change because the structural deformation may cause permanent magnets or circuits attached to the structure to also move relative to each other. If the structure undergoes large deformation then geometric nonlinearities must be included. In addition, if the coupled problem is a dynamic problem, then the electrical circuits, the magnetic circuits and the structural analysis must be solved as a coupled problem. Another source of nonlinearity is due to contact between the armature and the stator.

This page intentionally left blank



## VIII. LIST OF REFERENCES

- [1] Donald R. Snyder, Robert L. Sierakowski, Eugene R. Chenette and Jon W. Aus., "Preliminary Assessment of Electro-Thermo-Magnetically Loaded Composite Panel Impact Resistance/Crack Propagation with High Speed Digital Laser Photography", 24th International Congress on High-Speed Photography and Photonics, Eds. Kazuyoshi Takayama, Tsutomu Saito, Harald Kleine, Eugene Timofeev, Proceedings of SPIE Vol. 4183 (2001), pp. 488-513.
- [2] Olesya Zhupanska and Robert Sierakowski, 2005, "Mechanical response of composite in the presence of electromagnetic field", Proceeding of the 46th AIAA/ ASME/ ASCE/ AHS/ ASC Structures, Structural Dynamics, and Materials Conference.
- [3] Xiaojun, W., and Chung, D. D. L., 1996, "Continuous carbon fibre epoxy-matrix composite as a sensor of its own strain", Smart Materials and Structures, 5(6), pp. 796-800.
- [4] Wang, S., and Chung, D. D. L., 2007, "Negative piezoresistivity in continuous carbon fiber epoxy-matrix composite", Journal of Materials Science, 42(13), pp. 4987-4995.
- [5] Angelidis, N., Wei, C. Y., and Irving, P. E., 2004, "The electrical resistance response of continuous carbon fibre composite laminates to mechanical strain", Composites Part a-Applied Science and Manufacturing, 35(10), pp. 1135-1147.
- [6] Irving, P. E., and Thiagarajan, C., 1998, "Fatigue damage characterization in carbon fibre composite materials using an electrical potential technique", Smart Materials and Structures, 7(4), pp. 456-466.
- [7] Todoroki, A., and Yoshida, J., 2004, "Electrical resistance change of unidirectional CFRP due to applied load," JSME International Journal Series a-Solid Mechanics and Material Engineering, 47(3), pp. 357-364.
- [8] Wen, S. H., Wang, S. K., and Chung, D. D. L., 2000, "Piezoresistivity in continuous carbon fiber polymer-matrix and cement-matrix composites," Journal of Materials Science, 35(14), pp. 3669-3675.
- [9] Wang, S. K., and Chung, D. D. L., 2006, "Self-sensing of flexural strain and damage in carbon fiber polymer-matrix composite by electrical resistance measurement," Carbon,

- 44(13), pp. 2739-2751.
- [10] Angelidis, N., and Irving, P. E., 2007, "Detection of impact damage in CFRP laminates by means of electrical potential techniques," *Composites Science and Technology*, 67(3-4), pp. 594-604.
  - [11] Wang, S. K., Wang, D. J., Chung, D. D. L., and Chung, J. C. H., 2006, "Method of sensing impact damage in carbon fiber polymer-matrix composite by electrical resistance measurement," *Journal of Materials Science*, 41(8), pp. 2281-2289.
  - [12] Chung, D. D. L., 2007, "Damage detection using self-sensing concepts," *Proceedings of the Institution of Mechanical Engineers Part G-Journal of Aerospace Engineering*, 221(G4), pp. 509-520.
  - [13] Wang, X. J., Wang, S. K., and Chung, D. D. L., 1999, "Sensing damage in carbon fiber and its polymer-matrix and carbon-matrix composites by electrical resistance measurement," *Journal of Materials Science*, 34(11), pp. 2703-2713.
  - [14] Wang, D., and Chung, D. D. L., 2006, "Comparative evaluation of the electrical configurations for the two-dimensional electric potential method of damage monitoring in carbon fiber polymer-matrix composite," *Smart Materials & Structures*, 15(5), pp. 1332-1344.
  - [15] Wang, D. J., Wang, S. K., Chung, D. D. L., and Chung, J. H., 2006, "Sensitivity of the two-dimensional electric potential/resistance method for damage monitoring in carbon fiber polymer-matrix composite," *Journal of Materials Science*, 41(15), pp. 4839-4846.
  - [16] Wang, S. K., Chung, D. D. L., and Chung, J. H., 2005, "Impact damage of carbon fiber polymer-matrix composites, studied by electrical resistance measurement," *Composites Part a-Applied Science and Manufacturing*, 36(12), pp. 1707-1715.
  - [17] Louis, M., Joshi, S. P., and Brockmann, W., 2001, "An experimental investigation of through-thickness electrical resistivity of CFRP laminates," *Composites Science and Technology*, 61(6), pp. 911-919.
  - [18] Abry, J. C., Choi, Y. K., Chateauminois, A., Dalloz, B., Giraud, G., and Salvia, M., 2001, "In-situ monitoring of damage in CFRP laminates by means of AC and DC measurements," *Composites Science and Technology*, 61(6), pp. 855-864.
  - [19] Kupke, M., Schulte, K., and Schuler, R., 2001, "Non-destructive testing of FRP by d.c. and a.c. electrical methods," *Composites Science and Technology*, 61(6), pp. 837-847.

- [20] Todoroki, A., Tanaka, M., and Shimamura, Y., 2002, "Measurement of orthotropic electric conductance of CFRP laminates and analysis of the effect on delamination monitoring with an electric resistance change method," *Composites Science and Technology*, 62(5), pp. 619-628.
- [21] Todoroki, A., and Tanaka, Y., 2002, "Delamination identification of cross-ply graphite/epoxy composite beams using electric resistance change method," *Composites Science and Technology*, 62(5), pp. 629-639.
- [22] Todoroki, A., Tanaka, M., and Shimamura, Y., 2005, "Electrical resistance change method for monitoring delaminations of CFRP laminates: effect of spacing between electrodes," *Composites Science and Technology*, 65(1), pp. 37-46.
- [23] Hirano, Y., and Todoroki, A., 2007, "Damage identification of woven graphite/epoxy composite beams using the electrical resistance change method," *Journal of Intelligent Material Systems and Structures*, 18(3), pp. 253-263.
- [24] Kubo, S., Kuchinishi, M., Sakagami, T., and Ioka, S., 2001, "Identification of delamination in layered composite materials by the electric potential CT method," *International Journal of Applied Electromagnetics and Mechanics*, 15(1-4), pp. 261-267.
- [25] Nakatani, K., Kubo, S., Sakagami, T., Shiozawa, D., and Takagi, M., 2007, "An experimental study on the identification of delamination in a composite material by the passive electric potential CT method," *Measurement Science & Technology*, 18(1), pp. 49-56.
- [26] Shiozawa, D., Kubo, S., and Sakagami, T., 2004, "An experimental study on applicability of passive electric potential CT method to crack identification," *Jsme International Journal Series a-Solid Mechanics and Material Engineering*, 47(3), pp. 419-425.
- [27] Shiozawa, D., Kubo, S., and Sakagami, T., 2006, "Experimental study on applicability of passive electric potential CT method for identification of three-dimensional surface crack," *JSME International Journal Series a-Solid Mechanics and Material Engineering*, 49(3), pp. 426-435.
- [28] Bertsekas, D. P., 1999, *Nonlinear Programming*, Athena Scientific, Belmont, MA.
- [29] Kumar A.V., A sequential optimization algorithm using logarithmic barriers: Applications to structural optimization, *Journal of mechanical design* 122 (2000) 271-277
- [30] Belytschko T, Krongauz Y, Organ D, Fleming M, Krysl P. Meshless methods: An overview

- and recent developments. *Computer Methods in Applied Mechanics and Engineering* 1996; 139:3-47
- [31] Lee KM, Li Q, Sun H. Effects of Numerical Formulation on Magnetic Field Computation Using Meshless Methods. *IEEE Transactions on Magnetics* 2006;42(9): 2164-2171.
  - [32] Li Q, Lee KM. An Adaptive Meshless Method for Magnetic Field Computation. *IEEE Transactions on Magnetics* 2006;42(8):1996-2003.
  - [33] Bruyère A, Illoul L, Chinesta F, Clénet S. Comparison Between NEM and FEM in 2-D Magnetostatics Using an Error Estimator. *IEEE Transactions on Magnetics* 2008; 44(6):1342-1345.
  - [34] Liu X, Deng Y, Zeng Z, Udpa L, Udpa SS. Model-Based Inversion Technique Using Element-Free Galerkin Method and State Space Search. *IEEE Transactions on Magnetics* 2009; 45(3): 2164-2171.
  - [35] Bottauscio O, Chiampi M, Manzin A. Computation of Higher Order Spatial Derivatives in the Multiscale Expansion of Electromagnetic - Field Problems. *IEEE Transactions on Magnetics* 2008;44(6):1194-1197.
  - [36] Muramatsu K, Yokoyama Y, Takahashi N. 3-D magnetic field analysis using nonconforming mesh with edge elements, *IEEE Transactions on Magnetics* 2002; 38(2): 433-436.
  - [37] Belytschko T, Parimi C, Moes N, Sukumar N, Usui S. Structured extended finite element methods for solids defined by implicit surfaces. *Int J Numer Meth Eng* 2003; 56: 609 – 635.
  - [38] Moes N, Béchet E and Tourbier M. Imposing Dirichlet boundary conditions in the extended finite element method. *Int J Numer Meth Eng* 2006; 67: 1641-1669.
  - [39] Abdelaziz Y, Hamouine A. A survey of the extended finite element. *Computers & Structures* 2008;86:1141-1151
  - [40] Belytschko T, Black T. Elastic crack growth in finite elements with minimal remeshing. *Int J Numer Meth Eng* 1999; 45: 601–620.
  - [41] Areias PMA, Belytschko T. Analysis of three-dimensional crack initiation and propagation using the extended finite element method. *Int J Numer Meth Eng* 2005;63:760–788,.
  - [42] Kumar AV, Burla R, Padmanabhan S, Gu LX, Finite element analysis using nonconforming mesh. *Journal of Computing and Information Science in Engineering* 2008;8(3): 031005.
  - [43] Kumar AV, Padmanabhan S, Burla R. Implicit boundary method for finite element analysis

- non-conforming mesh or grid. *Int J Numer Meth Eng* 2008;74(9):1421-1447.
- [44] Burla RK, Kumar AV. Implicit boundary method for analysis using uniform B-spline basis and structured grid. *Int J for Numer Meth Eng* 2008; 76(13):1993-2028.
- [45] Burla RK, Kumar AV, Sankar BV. Implicit boundary method for determination of effective properties of composite microstructures. *International Journal of Solids and Structures* 2009; 46(11-12):2514-2526.
- [46] K Höllig, *Finite element methods with B-Splines.*, SIAM: Philadelphia 2003.
- [47] V. L. Rvachev, T. I. Shieko, "R-functions in boundary value problems in mechanics", *Applied Mechanics Reviews* 1995; 48: 151-188.
- [48] V. Shapiro, I. Tsukanov, Meshfree simulation of deforming domains. *Computer-Aided Design* 1999; 31: 459-471.
- [49] Simkin J, Trowbridge CW. Use of the Total Scalar Potential in the Numerical-Solution of Field Problems in Electromagnetics. *Int J Numer Meth Eng* 1979; 14(3):423-440.
- [50] Coulomb JL. Finite Element 3-Dimensional Magnetic-Field Computation. *IEEE Transactions on Magnetics* 1981;17(6):3241-3246
- [51] Biro O, Preis K. On the Use of the Magnetic Vector Potential in the Finite Element Analysis of 3-Dimensional Eddy Currents. *IEEE Transactions on Magnetics* 1989;25(4):3145-3159
- [52] Preis K, Bardi I, Biro O, Magele C, Renhart W, Richter KR, Vrisk G. Numerical Analysis of 3D Magnetostatic Fields. *IEEE Transactions on Magnetics* 1991; 27(5):3798-3803
- [53] Albanese R, Rubianacci G. Magnetostatic Field Computations in Terms of 2-Component Vector Potentials. *Int J Numer Meth Eng* 1990;29(3):515-532
- [54] Mesquita RC, Bastos JPA. An Incomplete Gauge Formulation for 3D Nodal Finite Element Magnetostatics. *IEEE Transactions on Magnetics* 1992; 28(2): 1044 -1047.
- [55] Demerdash NA, Wang R. Theoretical and Numerical Difficulties in 3-D Vector Potential Methods in Finite-Element Magnetostatic Computations. *IEEE Transactions on Magnetics* 1990;26(5):1656-1658
- [56] Semenov AS, Kessler H, Liskowsky A, Balke H. On a vector potential formulation for 3D electromechanical finite element analysis. *Communications in Numerical Methods in Engineering* 2006;22(5):357-375.
- [57] Jin J. *The Finite Element Method in Electromagnetics*. Wiley-IEEE Press, 2002.

- [58] Chen Q, Konrad A. A review of finite element open boundary techniques for static and quasi-static electromagnetic field problems. *IEEE Transactions on Magnetics*, 1997; 33(1): 663-676.
- [59] Bathe KJ. *Finite element procedures*. Englewood Cliffs, NJ: Prentice-Hall, 1996.
- [60] Ventura G. On the elimination of quadrature subcells for discontinuous functions in the eXtended Finite-Element Method, *Int J Numer Methods Eng* 2006; 66: 761-795.
- [61] Natarajan S, Bordas S, Mahapatra DR. Numerical integration over arbitrary polygonal domains based on Schwarz–Christoffel conformal mapping. *Int J Numer Methods Eng* 2009; 80: 103-134.
- [62] J. Bastos and N. Sadowski, *Electromagnetic modeling by finite element methods*. CRC Press, 2003.
- [63] Coulomb JL, Meunier G. Finite-element implementation of virtual work principle for magnetic or electric force and torque computation. *IEEE Transaction on Magnetics* 1984; 20: 1894-1896.
- [64] Ren Z, Razek A. Local force computation in deformable-bodies using edge elements. *IEEE Transaction on Magnetics* 1992; 28: 1212-1215.
- [65] Huang L, Mandeville RE, Rolph WD. Magnetostatics and coupled structural finite element analysis. *Computers & Structures* 1999; 72: 199-207.
- [66] Grandia RS, Galindo VA, Galve AU, Fos RV. General formulation for magnetic forces in linear materials and permanent magnets. *IEEE Transaction on Magnetics* 2008; 44: 2134-2140.
- [67] W. B. Cheston, *Elementary theory of electric and magnetic fields*, John Wiley & Sons, NY, 1964.
- [68] R. Arumugam, D. A. Lowther, R. Krishnan, and J. F. Lindsay, “Magnetic-Field Analysis of a Switched Reluctance Motor Using a Two Dimensional Finite-Element Model.” *IEEE Transactions on Magnetics*, vol, pp. 1883-1885, 1985.
- [69] Brauer JR. *Magnetic Actuators and Sensors*. John Wiley & Sons, NY, 2006.
- [70] Mindlin RD. Influence of rotatory inertia and shear on flexural motions of isotropic elastic plates. *ASME Journal of Applied Mechanics* 1951 Vol 18.
- [71] Zienkiewicz OC, Taylor RL. *The Finite Element Method for Solid and Structural Mechanics*, Butterworth-Heinemann 2000.

- [72] Belytschko T. A Review of Recent Developments in Plate and Shell Elements. Computational Mechanics-Advances and Trends, AMD vol. 75, ASME, New York 1986.
- [73] Hughes TJR. Finite elements based upon Mindlin plate theory with particular reference to the four-node bilinear iso parametric element. Journal of Applied Mechanics 1981 48: 587–596
- [74] Hughes, T J R, Taylor R L, Kanoknukulchai W. A Simple and Efficient Finite Element for Plate Bending. International Journal for Numerical Methods in Engineering 1977 11(10) 1529–1543.
- [75] Bathe KJ, Dvorkin EN. A four-node plate bending element based on Mindlin-Reissner theory and a mixed interpolation. Int. J. Num. Methods in Eng. 1985 21: 367–383
- [76] Hughes T.J.R., 2000. The Finite Element Method: Linear Static and Dynamic Finite Element Analysis. Dover Publications, New York.
- [77] Bathe K. J, Finite element Procedures, Prentice Hall, NY.

**DISTRIBUTION LIST**  
**AFRL-RW-EG-TR-2010-047**

Defense Technical Information Center      1 Electronic Copy (1 File & 1 Format)  
Attn: Acquisition (OCA)  
8725 John J. Kingman Road, Ste 0944  
Ft Belvoir, VA 22060-6218

---

EGLIN AFB OFFICES:

AFRL/RWOC (STINFO Office)	- 1 Hard (Color) Copy
AFRL/RW CA-N	- STINFO Officer Provides Notice of Publication
AFRL/RWGN	- 1 Copy